June 2020

Theory, Fabrication, and Characterization of Perovskite Phototransistor

Fatemeh Khorramshahi
University of South Florida

Theory, Fabrication, and Characterization of Perovskite Phototransistor

by

Fatemeh Khorramshahi

A dissertation submitted in partial fulfillment
of the requirements for the degree of
Doctor of Philosophy in Electrical Engineering
Department of Electrical Engineering
College of Engineering
University of South Florida

Major Professor: Arash Takshi, Ph.D.
Ioanniss Kymissis, PhD.
Chris Ferekides, Ph.D.
Jing Wang, Ph.D.
Rasim Guldiken, Ph.D.
Xiaomei Jiang, Ph.D.

Date of Approval:
May 12, 2020

Keywords: Methylammonium Lead Iodide, Capillary Motion, Photodetector, Microfluidic, Piezoelectricity

Dedication

To my parents for their absolute love, support, and motivation.

Acknowledgments

First and foremost, this work would be impossible to finish without the endless support, guidance, and advice from my major professor Dr. Arash Takshi. He has thought me the methodology to carry out the research and to present the research work. I would like to thank him for his friendship, empathy, and his patience during continuous hours of discussion. I am extending my heartfelt thanks to his wife, and family for helping me during my stressful time.

I wish to express my deepest gratitude to my committee member, professor John Kymissis who trusted me after I talked to him for few minutes in the SPIE Optics + Photonics conference, on the most difficult moment of my studies without him knowing, he gave me extraordinary support, encouraged me and gave me the opportunity of working with his esteemed research group in his lab at the Columbia University for two months. He motivated me beyond what I thought was possible.

I would also like to thank my committee members Dr. Rasim Guldiken, Dr. Xiaomei Jiang, Dr. Jing Wang and Dr. Chris Ferekides who provided guidance and insightful feedback for my research. A warm thank you to Dr Shengqian Ma and Dr. Lukasz Wojtas for helping me in X-ray diffraction measurements, NREC's staffs, Richard Everly, Robert Tufts, Sclafani Louis-Jeune and Dr. Yusuf Emirov for their generous help and making the cleanroom such a good place to work.

I owe a great debt of gratitude to Seyedmorteza Hosseyni for being such a wonderful mentor and role model to me, students in Bio-Organic Electronics lab, CLUE lab students, Dr. Zachary Lamport, and Chrissy McGinn.

Above ground, I am indebted and forever grateful to my parents whose value to me only grows with age. Without their motivation, kind understanding and their full support I could have never accomplished all I have. I am also thankful for my brothers Ehsan, Mohammad, and Ali, and all my friends who bring happiness to my life.

Table of Contents

List of Tables

List of Figures

Abstract

In recent years, there has been a significant interest in making electronic devices with low-cost techniques and materials for both industrial and medical applications. Methylammonium lead iodide perovskite ($MAPbI_3$) is one of the novel materials which has drawn much attention owing to its outstanding optical and electrical properties along with inexpensive, simple, and easy fabrication methods. In this work, the feasibility of using microfluidic device fabrication techniques on making a perovskite phototransistor has been studied. The fabrication method well addresses challenges such as lead toxicity and instability.

In the first step, mechanical micromachining and laser engraving were employed to make two-terminal flexible perovskite photodetectors with an indium tin oxide (ITO)–$MAPbI_3$–ITO horizontal structure. Photodetectors were made by filling engraved microchannels using the capillary motion of the solution containing the perovskite precursors. In addition to studying the photoelectric response of the devices with a solar simulator, potentiostat, and a Keithley source measure unit (SMU), the fabricated samples were characterized using scanning electron microscopy (SEM), X-ray diffraction (XRD), and atomic force microscopy (AFM) methods.

Long term stability was observed when encapsulating the devices with either FluoroPel or CYTOP. Also, the effect of external normal and transverse forces on the photoelectric response of the devices were investigated, proving the piezotronic property of $MAPbI_3$. In the highest state, when the normal force of 340 kPa was applied the photocurrent of the two-terminal photodetector increased by 97%. At this condition, the device exhibited a sensitivity (I_{photo}/I_{dark}) of 3250 with a

photocurrent of ≈6.9 μA at 2.0 V bias and responsivity of 14.56 $mA.W^{-1}$ under white light illumination of 80 $mW.cm^{-2}$.

Finally, a perovskite phototransistor was fabricated following the optimized parameter of the laser ablation method to form the microchannel on an ITO coated polyethylene terephthalate (PET) substrate. The transistor characteristic proved the formation of a depletion-mode field-effect transistor (FET) with a conductive channel at 0 V gate-source voltage (V_{gs}) entering the saturation mode when the drain-source voltage (V_{ds}) was above 10.0 V.

The proposed fabrication method is fairly simple and can contribute to the integration of perovskite photovoltaic devices with optofluidic circuit elements which may help in the further development of low-cost and disposable medical devices.

Chapter 1: Introduction

1.1 Aims and Objectives

Nowadays, photodetectors have spanned a vast range of applications from the integrated optical microfluidic biosensor [1] to inter-satellite communications [2]. The large market size of photodetectors in consumer electronics, industrial equipment, automobile applications, aerospace, and defense has led to intense research interest and studies on finding the best material and structure to make a high-performance photodetector. Semiconductor-based photodetectors have been made in three main configurations: photodiode, photoresistor, and phototransistors [3-5].

While every configuration has its unique assets, phototransistors are three-terminal devices that produce higher current and therefore larger photoresponsivity. Moreover, phototransistors photocurrent can remain constant in a wide range of voltage which can be beneficial in specific applications. Although the fabrication of transistors requires more steps than diodes and resistors, the signal-to-noise ratio is higher in phototransistors due to their internal amplification mechanism.

On the other hand, the recently developed optofluidic technologies allow the integration of optical components and microfluidic devices to manipulate or measure liquid, light, and matter [6]. Optofluidic devices combine the advantages of microfluidic and optics. The optical measurements provide the advantage of contactless measurement which is mainly beneficial in biosensing and analysis applications [7].

As is shown in Figure 1.1, optofluidic circuits composed of two parts, a microfluidic circuit and an optical part which includes optical components, a light source, and a photodetector to monitor the photoabsorption of the liquid in the microchannels [8]. The optical part can be fully

integrated with the microfluidic circuit using optofluidic laser sources and optofluidic waveguides [9, 10].

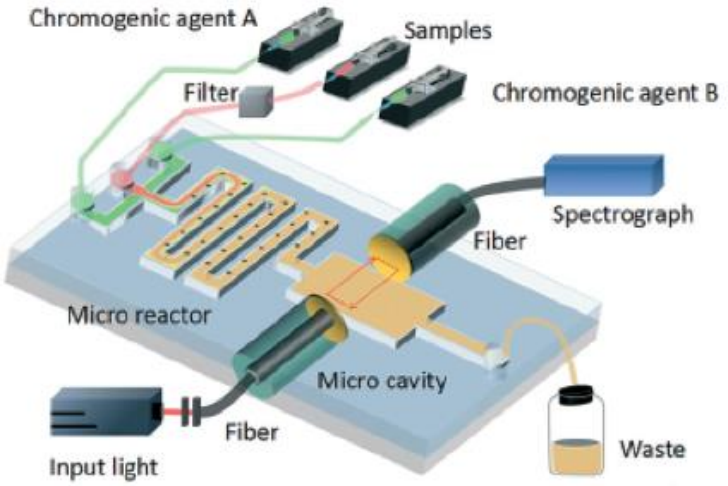

Figure 1.1 A schematic of the optofluidic microchip consisting of the microfluidics circuit and the optical part (used with permission [8]).

In biosensing applications, factors such as size, power, cost, and ease of implementation are of importance in the design of a photodetector. To reduce the cost and enable the production of a portable device, ambient light could be used as a natural light source. However, a highly sensitive photodetector would be needed to be integrated with the microfluidic circuit part of the optofluidic device. Various medical testing products including some pulse oximetry [11] and immunosensing [12] devices are examples using ambient light and highly sensitive photodetectors to reduce the size and cost.

On the other hand, metal halide perovskites are highly photosensitive and inexpensive semiconductors. Also, their various solution-based deposition methods have been employed for solar cells and visible light photodetectors [13]. Therefore, metal halide perovskites can be used as the photodetector component in optofluidic circuits for industrial or medical applications.

Particularly, perovskite photodetectors can be used in lab-on-a-chip (LOC) optofluidic devices for photo-spectroscopic measurement of analytes. A simple and low-cost fabrication

method will allow fast production of inexpensive, disposable devices to be used for detecting contaminants in drinking water, testing blood or saliva [14-16].

Both organic and inorganic semiconductors have been used as photoactive materials for making photodetectors. Defect-free single crystals of inorganic materials such as silicon can be used to make photosensors. Although organic semiconductor-based photodetectors have shown lower performance, their fabrication process is low-cost and solution-based. Organic-inorganic perovskites offer both low-cost fabrication process and better performance than organic semiconductors [17]. Some of the challenges that hinder large-scale fabrication of high-performance perovskite devices are instability, the toxicity of lead and the existence of trap states and defects in the crystalline structure of the materials. Table 1.1 summarized the features and challenges scientists face when using different materials to make photodetectors.

Table 1.1 Comparison between different materials of fabricating visible light phototransistors.

Material	**Fabrication and Features**	**Challenges**
Crystalline Inorganic Semiconductors	• The most mature conventional fabrication process • Proper control • Defect-free • Integration • Resolution	• Mainly high temperature, complicated fabrication process • Rigid substrate • Expensive
Organic Semiconductors	• Low cost • Simple, low-temperature fabrication	• Low performance • Defects • High recombination rate
Metal Halide Perovskites	• Low cost • Simple, low-temperature fabrication • Bandgap tuning • High performance	• Instability • Defects • Toxicity

The majority of reported perovskite-based sensors are using thin-film fabrication methods such as spin coating that spread the toxic materials. Another challenge in the fabrication is in

patterning the semiconductor for building devices, due to the high sensitivity of perovskites to the solvents used for photolithography. The objective of this work was to study the feasibility of fabricating perovskite-based photosensors using a novel method that employs the capillary force to fill patterned microfluidic channels with perovskite precursor solutions

Although the research focus in this dissertation is on $MAPbI_3$, the studied fabrication method is applicable for fabricating various forms of flexible electronic devices and circuits. The total market of flexible electronics will be $41.2 billion in 2020 and it has been projected that it will grow to $74 billion in 2030 [18]. As is shown in Figure 1.2, printed and flexible sensors are one of the majority segments.

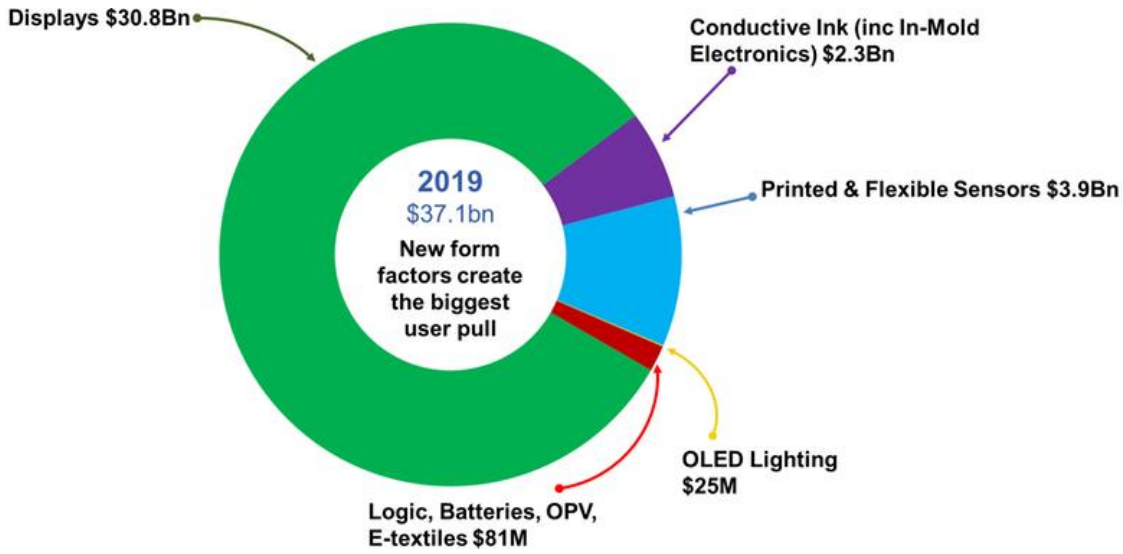

Figure 1.2 Market of the printed, organic, and flexible electronics industry in 2019 (open access article [18]).

1.2 Literature Survey

$MAPbI_3$-based phototransistor's structures are categorized into three general structures, photo-field effect transistor (photo-FET), hybrid photo-FET, and barristor-type [19]. Photo-FET structure can be top or bottom-gate while having top or bottom-contacts [20]. $MAPbI_3$ hybrid photo-FETs combine high absorption and slow recombination rate of $MAPbI_3$ with high mobility

properties of another semiconductor to enhance the functionality of pure $MAPbI_3$ phototransistor. Gate-modulated Schottky barrier or barrister-type employs 2D materials such as graphene to interchange the nature of the gate-dielectric and gate electrode junction between Schottky barrier and ohmic contact [19].

The first pure $MAPbI_3$-based phototransistor which was able to modulate drain-current by varying applied gate-voltages was introduced by Li et al [21]. They reported an ambipolar carrier transport with the mobility of 0.18 (0.17) $cm^2V^{-1}s^{-1}$ for holes (electrons) at room temperature.

While most of the research groups have used SiO_2 as the gate oxide layer [21-27], poly(perfluorobutenylvinylether) (CYTOP) [28], HfO_2 [29, 30], Ta_2O_5 [31], and AlO_x [32]have also been used as the insulator layer between the gate contact and the semiconducting channel. In the work by Mohite et al., higher gate modulation and lower hysteresis were obtained using high dielectric constant HfO_2 (HfO_2 relative dielectric constant ε_r is 23.5) [30]. However, due to the presence of traps at the interface of HfO_2/perovskite, a very low mobility of 10^{-3} $cm^2V^{-1}s^{-1}$ was reported. On the other hand, fluoropolymer CYTOP ($\varepsilon_r \sim 2$) yields a low density of electronic trap states at its interface with the semiconductors and consequently produce high-mobility organic field-effect transistors (OFETs) exhibiting minimal bias-stress effects [20]. The summary of fabricated $MAPbI_3$ based phototransistors is shown in Table 1.2.

Table 1.2 Summary of fabricated $MAPbI_3$ based phototransistors.

Year	**Material**	**Substrate**	**Method**	**Carrier transport**	**Ref.**
2015	$MAPbI_3$ thin-film	Si	Two-step vapor-assisted	Ambipolar	[21]
2015	$MAPbI_{3-x}Cl_x$		One-step spin coating	Ambipolar No current modulation	[28]

Table 1.2 (Continued)

2015	Hybrid graphene $MAPbBr_2I$	Si	One-step spin coating	Ambipolar No current modulation	[33]
2015	Tetragonal $MAPbI_3$ thin-film	Si	One-step spin coating	LT** current modulation	[22]
2016	2D $MAPbI_3$	Si	Combined solution process and vapor-phase conversion	No current modulation	[23]
2015	$MAPbI_3$ microplate crystals	Si	Seeded growth process		[34]
2016	Hybrid C8BTBT* onto $MAPbI_3$	Si	Co-evaporating	Unipolar	[35]
2016	$MAPbI_3$	Si	Modified vapor-assisted solution process	Unipolar No current modulation	[24]
2016	Orientationally pure crystalline $MAPbI_3$	Si	Thermal-gradient-assisted directional crystallization	Ambipolar	[26]
2017	$MAPbI_3$ thin-film	Glass	Doctor blade	No current modulation	[36]
2017	$MAPbI_3$ microplates	Si	Vapor phase intercalation Process	P-type to ambipolar to N-type by thermal annealing LT current modulation	[27]
2017	Hybrid $MAPbI_{3-x}Cl_x$/CNT	Si	One-step spin coating	Ambipolar	[37]
2017	$MAPbI_3$ thin-film	Glass	Two-step spin coating	No transfer characteristic	[38]
2017	$MAPbI_3$ thin-film	Si and Glass	One-step spin coating	Ambipolar at LT Unipolar at HT***	[39]
2018	$MAPbI_3$ single crystal			Ambipolar No Saturation Regime	[40]
2018	$MAPbI_xCl_{3-x}$	Si	Multi-step annealing process	Ambipolar No Saturation Regime	[41]
2018	$MAPbI_3$ thin-film	Glass	One-step spin coating	Vertical structure with ITO contact	[29]

Table 1.2 (Continued)

2019	$MAPbI_3$ thin-film	Glass	One-step spin coating	Ambipolar	[32]
2019	$MAPbI_3$ micro/nanowire	Si		Unipolar/P-type	[42]
2019	$MAPbI_3$	Glass	One-step spin coating	Ambipolar	[43]
2019	$MAPbI_3$ thin-film	Si	Hot-casting method	Unipolar/P-type	[30]
2019	$MAPbI_xCl_{3-x}$	Si	One-step spin coating	Ambipolar	[44]
2020	$MAPbI_3$/PDVT-10 and $MAPbI_3$/N2200 nanowire heterojunctions	Si/Glass	Cast and mold cleanroom microfluidic fabrication	Ambipolar	[45]

* Dioctylbenzothieno[2,3-*b*]benzothiophene, ** Low temperature, ***High temperature

In this dissertation, the motivation and literature review are discussed in Chapter 1. Chapter 2 covers the background of the material structure and perovskite electro-optical properties along with the methods that were used for designing, fabricating, and characterizing sensors. In Chapter 3, the feasibility of fabricating a two-terminal perovskite photodetector by microfluidic techniques is demonstrated. The stability and electro-mechanical properties of the fabricated photodetectors are studied in Chapter 4 and Chapter 5 respectively. The designed perovskite phototransistor is introduced in Chapter 6. Chapter 7 includes the conclusion and suggested works for the future.

Chapter 2: Perovskite Background and Properties

In general, perovskite is a class of material with a chemical formula of ABX_3. Where A is an organic or inorganic large cation, B is usually a medium-size cation that can be a metal ion, and X is an anion such as a halide or any mixture of different halides [46]. The name perovskite had been given by G. Rose in 1839 [47]. Materials with perovskite structure are classical systems for phase transition which depends on the tilting and rotation of the BX_6 polyhedra in the lattice [48, 49]. Reversible phase transition may be induced by different stimuli such as electric field [50, 51], pressure [52, 53], and temperature [54, 55].

Over the past decade, metal halide perovskites (MHPs) and particularly methylammonium lead iodide ($CH_3NH_3PbI_3$ or $MAPbI_3$) have attracted a lot of attention in solar cell research. This arises from two key characteristics: their excellent electro-optical properties and feasibility of using them to fabricate devices with low-cost and simple methods. In this chapter, perovskite material and its properties are discussed in detail.

2.1 Metal Halide Perovskites Basics

Metal halide perovskites are semiconductors. In their ABX_3 structure, A site is Methylammonium (MA) $CH_3NH_3^+$, Formamidinium (FA) $CH(NH_2)_2^+$, Guanidinium (GA) $C(NH_2)_3^+$ or Cs^+, B site is Pb^{2+} or Sn^{2+} and X is I^-, Br^- or Cl^- [56-61]. The optical bandgap and electronic properties can be tuned by changing the materials. It has been shown that, in the A-site of ABX_3 structure of MHP, by changing MA to mixed MA-FA or substituting a different mixture of any halide to X, the bandgap of perovskite can be tuned and crystal structure changes due to the different cation size [62].

Single crystal MHPs have a remarkably low density of trap-states [63]. MHPs have variety of applications such as solar cells (SCs) [64], light-emitting diodes (LEDs) [65], thin-film transistors (TFTs) [66], photodetectors [67], and Laser diodes [68]. Figure 2.1 shows the schematic of the perovskite crystal structure and the energy levels in some perovskite materials.

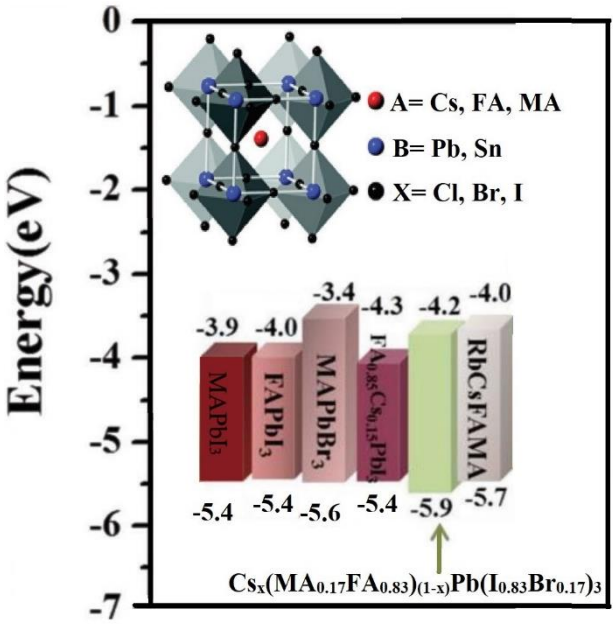

Figure 2.1 A general schematic of the perovskite structure and the energy levels in perovskite materials (open acess article [69]). The numbers at the top and bottom of each column show the edge of conduction and valence bands in the materials, respectively.

2.2 Methylammonium Lead Iodide Structure, and Properties

$MAPbI_3$ is the most common perovskite considered for photovoltaic applications. It has been extensively studied and employed in solar cells, due to the rapid growth of power conversion efficiency (PCE) reported for $MAPbI_3$-based devices already exceeding 20% [70, 71].

Three phases have been identified in $MAPbI_3$ single crystals: orthorhombic, tetragonal, and cubic Polymorphs. Indeed it has been suggested that $MAPbI_3$ crystalizes in the tetragonal phase at room temperature, a tetragonal to orthorhombic transition occurs below ~160 K with a cubic phase being stable from around 330 K and above [49]. It should be mentioned that the chemical and physical properties of lead halide perovskites strongly depend on its preparation method [72].

2.2.1 Optical Properties

While the unique optical properties of perovskite semiconductors had been studied many years back [73], since the first $MAPbI_3$ based solar cell was reported by Miyasaka and his group in 2009 [74], a tremendous effort has been made by researchers to investigate these properties in a variety of forms of lead halide perovskite with deposition techniques. The direct bandgap of about 1.55-1.65 eV which is suitable for visible light absorption, has been reported by several research groups [75-77].

A broad absorption spectrum covering both visible and near-infrared regions has been observed in $MAPbI_3$ [78]. The reported absorption coefficient at visible wavelengths ranged between 10^4 and $10^5\,cm^{-1}$ [79]. Single crystal $MAPbI_3$ has a low number of defects and lower density of trap states, thus unlike polycrystalline form, it has long exciton diffusion length (>175 μm under 1 sun) and high carrier recombination lifetime (τ=92 μs under 1 sun) [80].

2.2.2 Electrical Properties

To predict some electrical characteristics such as conductivity, maximum photovoltaic potential, energy bending at the interfaces, and formation of Schottky or Ohmic contacts, it is needed to understand the doping mechanism of the semiconductor [81]. While in non-ionic crystalline semiconductors such as silicon or germanium, substitutional impurities can replace the host atoms and change the Fermi level and conductivity of the semiconductor, due to high ionicity of $MAPbI_3$, ambipolar characteristics or preferential p-type or n-type transport characteristics might be observed from $MAPbI_3$-based devices without any external dopant [32]. Substitutional impurities have been used in $MAPbI_3$ based devices as well. In a study by Yang et al., $MAPbI_3$ was doped by a group of polarized ferroelectric polymers [82].

Different processes such as thermal annealing and growth condition or precursor ratio (MAI/PbI_2) may impact self-doping and change in the material type of $MAPbI_3$. Field-induced and photoinduced self-doping effects have been also introduced to be responsible for the change in $MAPbI_3$ Fermi level [83]. In the work by Huang et al. it was shown that MAI-rich and PbI_2-rich perovskite films are p and n self-doped, respectively. Ultraviolet photoelectron spectroscopy (UPS) of $MAPbI_3$ samples formed by one-step spin coating method is shown in Figure 2.2 [81].

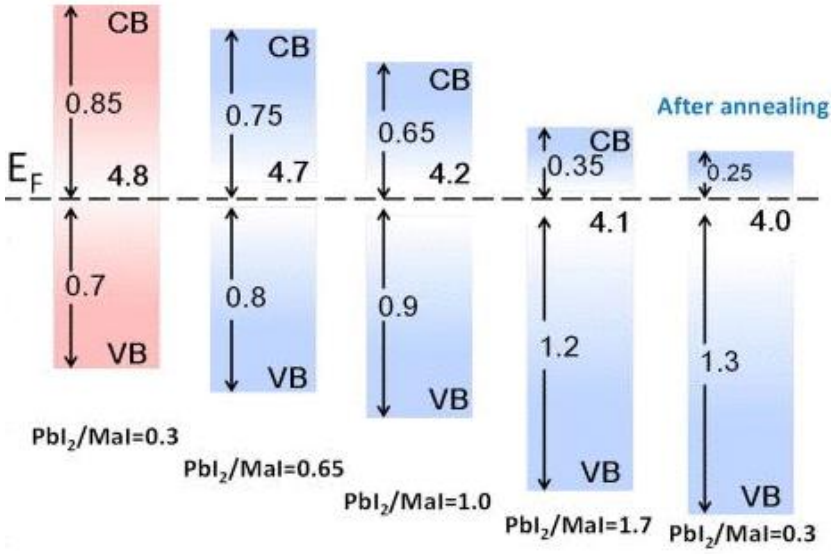

Figure 2.2 UPS measured energetic levels of perovskite films formed by one-step method with different precursor ratios (used with permission [81]).

To determine the material type, some research groups considered $MAPbI_3$ as a conventional semiconductor and then methods such as Kelvin probe [84] and Hall effect [85] were employed. Yet, the ambipolar characteristic has been reported by several researchers testing the materials in a transistor structure [21, 28]. Very large charge mobility higher than 100 $cm^2V^{-1}s^{-1}$ has been observed in $MAPbI_3$ single crystals [80].

2.2.3 Piezoelectricity

As it was mentioned before, $MAPbI_3$ has three crystalline phases: cubic, tetragonal, and orthorhombic. The most stable phase at room temperature is the tetragonal phase [86], which has

been ascribed to a polar space group I4cm [87] and is shown to be ferroelectric [87] and piezoelectric [88-92]. Polarized domains have been observed in both single crystal and thin-film polycrystalline forms of $MAPbI_3$ [89, 92].

2.3 Fabrication Techniques

The feasibility of fabricating devices with low-cost methods using inexpensive precursor materials is one of the main advantages of lead halide perovskite-based devices. While spin coating as a low-cost method is the most common technique for thin-film deposition of $MAPbI_3$ [93, 94], a wide range of techniques have been introduced to make high-quality perovskite films. That includes co-evaporation [95], vapor-assisted solution process (VASP) [96], sputtering [97], doctor-blading [98], spray coating [99] and inkjet printing [100].

Spin coating of perovskite can be done in two-steps or one-step. In both methods, MAI and PbI_2 are being used as precursors. In the one-step method, a precursor solution can be prepared by dissolving PbI_2 and MAI in a polar solvent such as N,N-dimethylformamide (DMF), dimethyl sulfoxide (DMSO) and/or γ-butyrolactone (GBL). A thin film of perovskite can be made by spin coating the solution on a substrate and curing the sample. In the two-step method, first, a solution containing PbI_2 is spun coated on a substrate, and then the MAI solution will be dip coated or spun coated on a sample.

Despite the ease of fabrication and cost-effectivity of spin coating, this method is generally limited to a scale of <10 cm, and a large portion (>90%) of the precursor solution is wasted in the process [101]. On the other hand, spin coating is suitable for forming a thin coating layer of perovskite on the entire surface area and impossible to form different patterns of perovskite by spin coating. Also, hydrophobicity of some substrates makes the use of spin coating difficult for perovskite deposition [102].

In addition to above-mentioned drawbacks of spin coating method, in the case of $MAPbI_3$, there is a growing concern regarding the lead toxicity driven by the result of the restriction of hazardous substances directive (RoHS) regulations. Lead toxicity related concerns lead to employing a method which does not waste the precursor and requires as low as possible amount of $MAPbI_3$ precursor.

Different groups have tried to form perovskite patterns. Gu et al. introduced a vapor–solid–solid reaction (VSSR) process to grow ordered three-dimensional (3D) $MAPbI_3$ nano-wire arrays using a nanoengineered template [103]. Despite the feasibility of forming arrays of perovskite, the vapor deposition methods are complicated and require a high vacuum and high-temperature equipment [104]. The solution processability of halide perovskites has motivated to use novel fabrication methods. In this project, microfluidic methods have been suggested for patterning the perovskite precursor solution to fabricate photosensors.

2.3.1 Microfluidic Methods

Microfluidic devices employ surface tension effect encoded by the geometry and surface chemistry of a microchannel to deliver liquid. The liquid flows through capillary action and it happens when the adhesion to the surface material is more powerful than the cohesive forces between molecules of a liquid [105]. Since the first microfluidic device was made in 1979 [106], many different approaches were employed to make capillary channels and chips including micromachining, cleanroom fabrication techniques, and rapid prototyping. Notable developments in capillary circuits are represented in Figure 2.3.

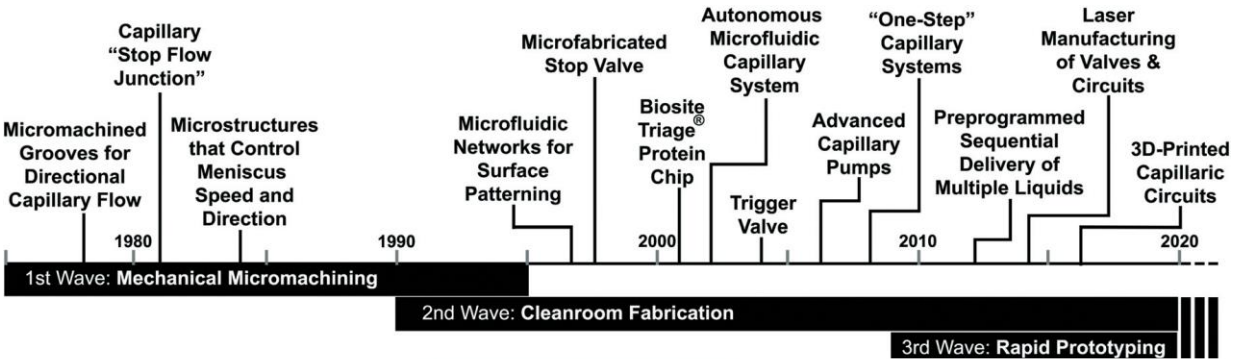

Figure 2.3 The three waves of capillary circuits with notable developments highlighted in the timeline (open acess article [105]).

Cleanroom fabrication of capillary circuits is expensive and needs complicated equipment to make cast and mold. Cast and mold degrade over time and the material wastes. On the other hand, mechanical micromachining is cast/mold- and cleanroom-free. It is easy to use on various types of substrates. This method is suitable for rapid fabrication, both mass production and prototyping of microfluidic devices.

In addition, over the last few years, with the high development of laser technology, laser ablation has been considered as an alternative technique to traditional lithography in the fabrication of microfluidic devices. Since $MAPbI_3$ has the solution-based deposition method, the capillary motion of the one-step method perovskite precursor can be used for filling a laser-engraved patterned conducting layer.

In general, laser engraving or laser ablation can be performed by melting or vaporizing the target material using a focused laser beam on a material surface or inside the bulk part and removing the intended parts of the target through heating. Sor far, to fabricate microfluidic devices, CO_2 [107], Nd:YAG [108] and Q-switched solid state [109] lasers have been employed. Among different types of laser sources, CO_2 source provides low-cost advantage [110]. The desirable microchannel dimensions can be fabricated by manipulating several factors, including

focus length, the pulse repetition rate, machining speed, and the absorption coefficient of the materials [111].

Different polymers such as polymethyl methacrylate (PMMA) [112], PET [113] and polydimethylsiloxane (PDMS) [114] have been ablated by CO_2 laser to make a microchannel. Surface tension effect helps the fluid to flow in a microchannel which is called capillary motion. According to fluid mechanics, the flow resistance within a microchannel and the flow rate can be calculated using Equation (1) and (2) respectively [105]:

$$\boldsymbol{R} = \frac{\boldsymbol{\Delta P}}{\boldsymbol{Q}} \qquad (2\text{-}1)$$

$$\boldsymbol{Q} = \boldsymbol{A} \times (\bar{\boldsymbol{v}}) \qquad (2\text{-}2)$$

where A is the cross-section area, ΔP is the difference in capillary pressure across the microchannel, and $\bar{v}$ is the average velocity of the fluid. The contact angles and microchannel size determine the capillary pressure [105]. Once microchannels are made, the one-step method precursor of lead halide perovskites can fill the engraved channels and after solidifying make the perovskite crystal inside the channel [102].

2.4 Stability

Although perovskite solar cell is the fastest developing photovoltaic technology [115, 116] since 2010, the instability of organic-inorganic halide perovskites has hindered its implementation for large scale industrial applications. Humidity, heat, light, oxygen, and electric field can induce decomposition of methylammonium lead iodide perovskite. The responsible process for the potential initial step of the moisture-induced decomposition of $CH_3NH_3PbI_3$ is the following chemical reactions [69, 117]:

$$CH_3NH_3PbI_3(s) \leftrightarrows PbI_2(s) + CH_3NH_3I(aq.) \qquad (2\text{-}3)$$

$$CH_3NH_3I(aq.) \leftrightarrows CH_3NH_2{+} + HI(aq.) \qquad (2\text{-}4)$$

$$4HI(aq.) + O2 \leftrightarrows I_2(s) + 2H_2O \quad (2\text{-}5)$$

$$2HI(aq.) \leftrightarrows H_2 + I_2(s) \quad (2\text{-}6)$$

Some strategies such as minimizing the exposure to environment by encapsulation techniques [118, 119], improving film qualities [120], and engineering thermally stable, water-repelling interlayers [121] have been proposed to suppress the decomposition of perovskite and improve the stability of device.

Hydrophobic fluoropolymers such as CYTOP provide a water repellant layer that does not let water molecules penetrate the perovskite layer. These polymers can be used for encapsulation in perovskite devices [122, 123]. FluoroPel is another type of fluoropolymer thin film coating fluid which is manufactured by Cytronix corporation [124]. FluoroPel dielectric strength and contact angle are higher than CYTOP [125]. FluoroPel is a true solution fluid and does not carry micron-sized solids therefore results in much thinner, smoother coats than fluid based on carrying suspended solids [124]. Also, it has sufficient adhesion to the surface even without thermal curing.

2.5 Ion Migration

Among all factors that cause the instability of $MAPbI_3$, ion migration has been recently introduced as intrinsic to the perovskite polycrystalline films and cannot be removed by encapsulation methods [126].

The I-V hysteresis loop of the perovskite devices which can be capacitive and partly non-capacitive [127-131] is believed that arises from three major mechanisms: charge trapping/detrapping process on the surface and grain boundaries of the perovskite, ion migration [132], and polarization [130].

Extraction of photogenerated charge, recombination, and polling can cause a non-capacitive effect in perovskite-based devices [129, 130]. The contact material determines the

activation energy required for ion migration at the interface and the rate of the ion migration at the interface of the perovskite layer depends on the contact material as well [133].

Chapter 3: Two-Terminal Photodetectors

Methylammonium lead halide perovskites have shown outstanding electrical and optical properties which make them excellent candidates to be used as the photoactive layer in photodetectors[134]. Different structures have been introduced for fabricating $MAPbI_3$-based photodetectors such as Schottky junction [135] and heterojunction [136] in vertical [137] or lateral [138] structures. Non-ohmic contacts provide low dark-current which leads to high sensitivity (the ratio of photocurrent to dark-current) and low shot noise in photodetectors [139]. By employing a mechanism that maintains the junction barrier in the dark but reduces it in the light, the sensitivity can be further improved.

In this chapter, two different photodetectors with lateral structures are introduced by using two non-lithographic and low-cost methods to make high aspect ratio $MAPbI_3$ microchannels on a flexible substrate. In the first method, manual mechanical machining was used to make a capillary microchannel. The second method uses a laser engraving tool which showed remarkable enhancement in the reproducibility of fabricated capillary channels.[*]

3.1 Perovskite Photodetector by Mechanical Machining

As it was discussed in the second chapter, mechanical micromachining is one of the fastest methods to make microchannels. These channels can be used to be filled with the perovskite precursor and form a lateral structure. The experimental details are presented in the next sections.

[*] Sections 3.1.1-3.3 are as presented in the published work at Organic and Hybrid Sensors and Bioelectronics XI. Vol. 10738. International Society for Optics and Photonics, 2018.

3.1.1 Experimental

3.1.1.1 Sample Fabrication

Flexible photodetector devices were fabricated by cutting ITO coated polyethylene terephthalate, PET, (60 Ωsqr, Sigma-Aldrich) to 1 cm×2 cm pieces. The perovskite precursor solution was prepared by dissolving a mixture of equimolar 0.5 M lead iodide (98.5%, Alfa Aesar) and methylammonium iodide (Lumtec) in gamma-butyrolactone (99%, Aldrich). The solution was stirred overnight at 1200 rpm and kept at 50 °C.

As shown in Figure 3.1, two different methods were used to make a channel on the ITO coated PET. In one method (similar to the conventional lithography), the entire surface of the ITO sheet was covered by the permanent marker as a mask. The tip of a tweezer was used to remove a part of the permanent marker by simply slipping the tip over the sample to make a straight line pattern with a width of ~200 µm and a length of 2 cm. Afterward, the sample was dipped into hydrochloric acid (1:2 HCl to DI water) to etch the exposed part of ITO. After removing the marker by acetone, two conductive ITO pads with a gap between was obtained. The sample was used to make a device by spin coating (500 rpm for 45 s) the perovskite precursor and heating on a hotplate for 10 minutes at 90°C.

In the other method, a custom-designed blade set up was used to make a groove on the ITO coated PET sample with a controlled depth (Figure 3.2.a). The groove formed a channel between the two sides (i.e. ITO pads) with a width of ~100 µm. Instead of spin coating the perovskite solution, 2 µl of the perovskite precursor was placed on one end of the channel. The droplet immediately spread into the channel under the action of the capillary force. Then the sample was placed on the hotplate and heated to 90°C. The schematic in Figure 3.2.b shows the structure of the device with the capillary method of fabrication.

As the final step, spin coating at 2000 rmp for 45 s was employed to deposit a 50 nm transparent layer of CYTOP on both samples for stability enhancement of the devices during the characterization step [122]. Then the samples were heated to 90°C for 40 minutes and kept in the desiccator for 24 hours to remove any residual solvent.

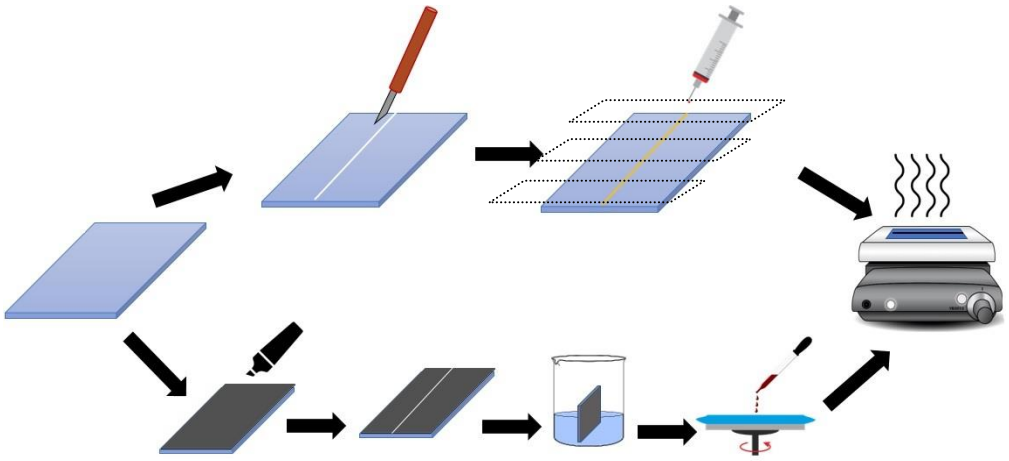

Figure 3.1 Fabrication steps of two different photodetectors using capillary motion and spin coating. Certain areas of the sample made by using capillary motion are labeled as A, B, and C referring to the beginning, middle, and end of the channel, respectively.

a) b)

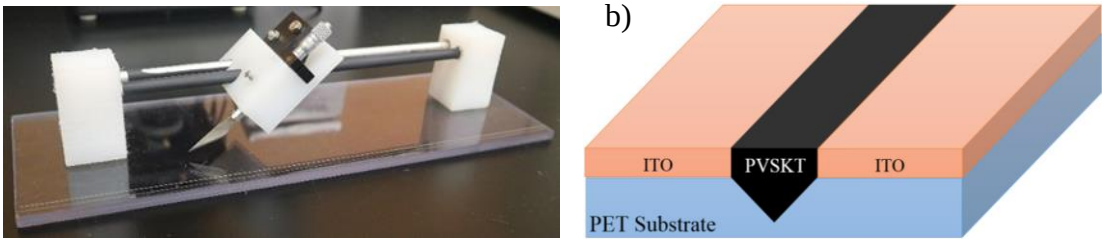

Figure 3.2 a) The custom-designed setup which was used to make the micro-channel. b) Schematic of the structure of the fabricated photodetector.

3.1.1.2 Characterization

Scanning electron microscopy (SEM) images were taken by an Hitachi S800 Scanning Electron Microscope. Thickness profile of the sample was measured by Dektak D150 profiler. The I-V characteristics (photocurrent, and dark current) were carried out using a VersaSTAT 4 potentiostat. All measurements were performed in a dark box connected to a solar simulator (RST,

Radiant Source Technology) via an optical fiber. The light intensity at the sample location was measured to be ~80 mW/cm^2.

3.1.2 Results and Discussion

The quality of the perovskite in the micro-channel was studied via optical microscopy and SEM methods. The optical images showed a fairly uniform coverage of perovskite along the micro-channel. SEM images of the fabricated sample using capillary motion are shown in Figure 3.3. The width of the channel was measured to be 100 µm. The zoomed picture in Figure 3.3.b shows perovskite grain size of ~2-5 µm.

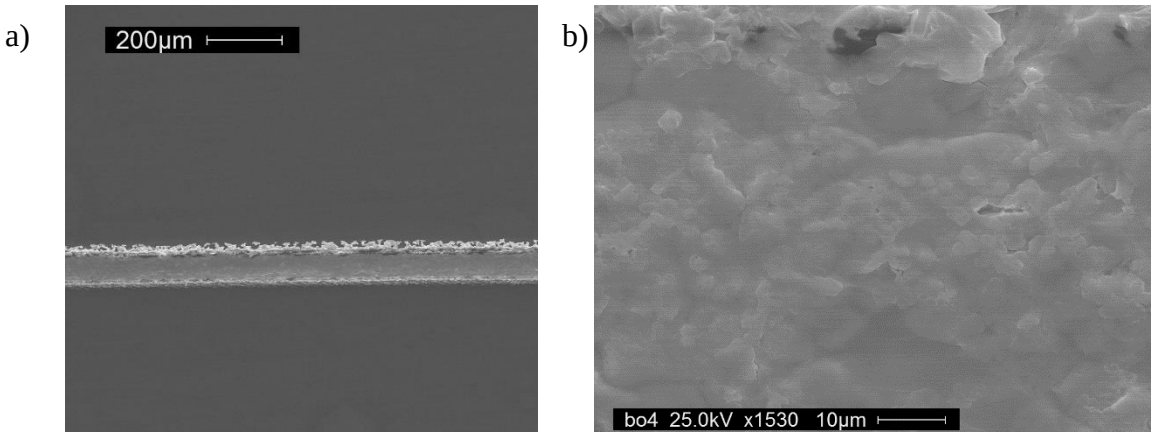

Figure 3.3 Top view SEM images of the fabricated sample using capillary motion.

Using a Dektak profilometer, the profile of the channel was studied at different points along the groove. Specifically, the profiles were measured at the beginning, middle, and end of the channel (regions A, B, and C in Figure 3.1). The measurement results are shown in Figure 3.4. a, b and c. Thickness profile of the sample was also measured after filling the channel with perovskite and spin coating 50 nm of CYTOP, which are shown in Figure 3.4. d, e, and f. As it can be observed the cut has made a channel with walls as high as ~30 µm and depth of ~20 µm. At the beginning of the channel (area which is marked by "A" in Figure 3.1) perovskite covered the entire depth of the channel. Moving along the channel, the thickness of the perovskite was lowered.

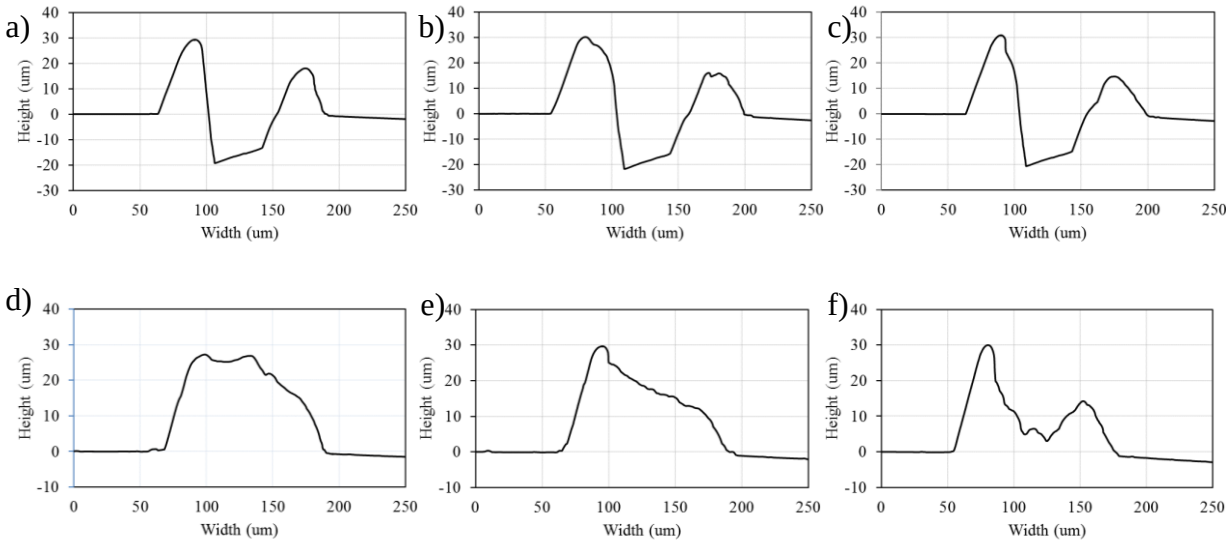

Figure 3.4 (a, b, and c) Dektak profile of the grooved ITO sample across the channel at the beginning, middle, and end of the channel (marked as A, B, and C in Figure 3.1), respectively. (d, e, and f) The profile of the sample at area A, B, and C after crystallization of perovskite which was formed due to the capillary motion of the liquid along the channel.

To explore the photoelectric properties of the samples, first, the transient photoresponse of the samples was measured and compared with the one made with the spin coating method. As shown in Figure 3.5, the device made by using capillary motion showed almost three times higher photocurrent while the device was biased at 2.0 V. The detail characteristic study was conducted by measuring the I-V characteristics under 80 mW/cm^2 visible light illumination and compared with the dark condition. As it can be observed in Figure 3.6.a, the photodetectors fabricated using capillary motion and spin coating showed the dark current as low as 2 nA and 0.5 nA at 2.0 V, respectively. The photocurrent at 2.0 V reached to 211 nA in the sample made by the capillary motion while it was only 76 nA in the spin coated sample. Light absorption at the surface of the perovskite layer causes electron and holes to be generated. Under the existence of electric field, generated charges were transported toward the electrodes. The non-symmetry I-V curves can be due to formation of Schottky barrier between $CH_3NH_3PbI_3$ and ITO.

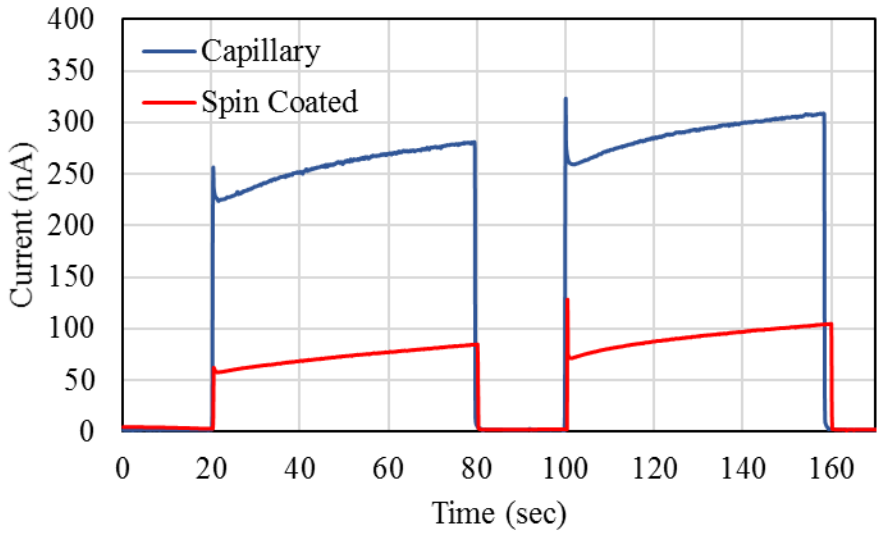

Figure 3.5 Transient photoresponses of the samples biased at 2.0 V.

In order to compare the two photodetectors, three figures of merit (i.e. sensitivity, responsivity, and normalized detectivity) were calculated as it is suggested in the literatures [140]. At 2 V the spin coated device reached the responsivity of 0.036 A/W, sensitivity of 40 and detectivity of 7.5×10^{7} Jones. While the device made by capillary motion showed a superior performance. At 2.0 V, the sensitivity of 172, responsivity of 0.1 A/W and normalized detectivity 2.6×10^{8} Jones were calculated for the other sample made by capillary motion. Which are respectively 4.3, 2.8 and 3.5 times higher than those in the spin coated sample (Table 3.1). The calculated responsivity in visible light for sample made using capillary motion is higher than the amount reported previously for the flexible photodetectors having lateral topology using ITO/$CH_3NH_3PbI_3$/ITO structure [141].

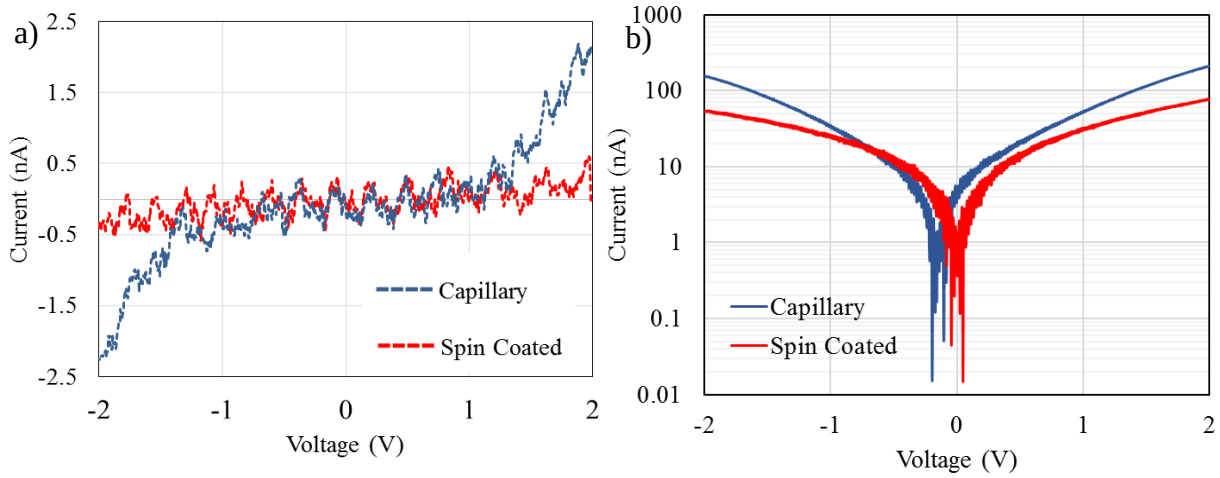

Figure 3.6 I-V characteristics of the fabricated samples a) in dark, b) under illumination.

Table 3.1 Comparison between figures of merit in fabricated samples.

	Responsivity (A/W)	**Sensitivity**	**Normalized detectivity (Jones)**
Capillary	0.1	172	2.5×10^{8}
Spin Coated	0.036	40	7.5×10^{7}

To further understand the difference in the nature of the junction made between perovskite and ITO when two different methods of fabrication was used to make a channel on ITO, the impedance of the samples were measured in the dark. As shown in Figure 3.7, the absolute value of impedance (at low frequencies) for the capillary used sample is one order of magnitude lower than the spin coated sample. This can be an indication of lower contact resistance between perovskite and ITO in the capillary sample. This lower impedance may explain the higher dark current in the capillary device. Nevertheless, the superior response from the device made with the capillary method is promising particularly for reducing the consumption of the toxic materials.

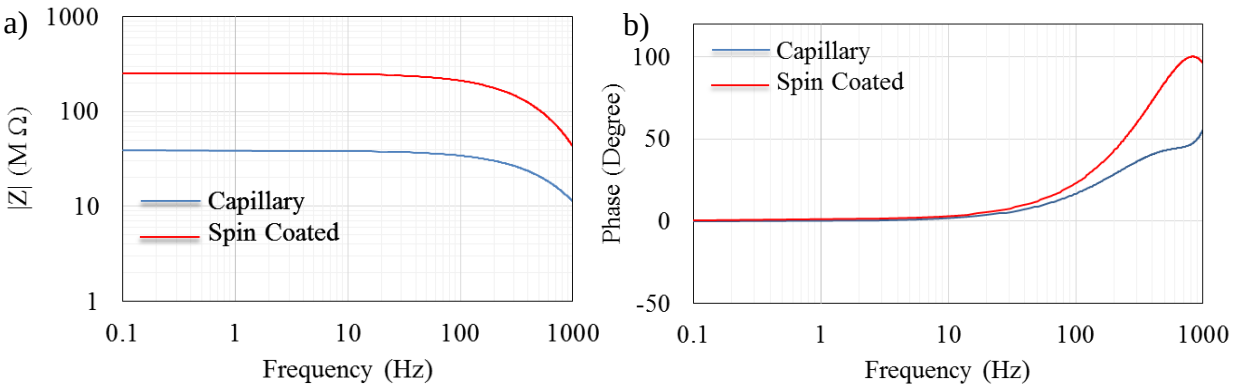

Figure 3.7 Impedance spectroscopy measurement ot the fabricated samples, a) amplitude and b) phase.

3.1.3 Conclusion

A novel method was introduced to pattern perovskite crystal along a micro-channel using the capillary force motion. This method was employed for fabrication of a photodetector. Another photodetector was made employing spin coating of perovskite precursor on a gap between two electrodes. The optical and electrical properties of the two devices were measured and compared. The sample made by capillary motion showed the better photoelectric properties. This enhancement was attributed to existence of the better contact between perovskite and the electrodes as the result of capillary motion of the perovskite precursor through the channel's walls. In future works, this novel method can be used for simple fabrication of low-cost devices based on perovskite micro-channels.

3.2 Perovskite Photodetector by Laser Ablation

Here a laser engraving technique for fast production of lead halide perovskite photodetectors is introduced. Several microchannels were fabricated using laser engraving of a

conductive flexible layer (ITO coated PET). The optimum laser parameters were found, and the photodetectors were fabricated by simply filling the microchannels by perovskite. †

3.2.1 Experimental

Several photodetectors were made by laser ablation of ITO coated polyethylene terephthalate, PET, (60 Ωsqr, Sigma-Aldrich) using a commercially available CO_2 laser (Epilog Fusion M2, 60 watt) which provides a laser beam of 10.6 μm wavelength printing in the vector mode with lowest beam diameter of 76.2 μm. The maximum number of laser pulses that the laser (used in this experiment) fires per inch of travel was 5000 pulses per inch (PPI) and its maximum machining speed was 254 $mm.s^{-1}$. The laser power, PPI and the machining speed were manipulated in order to fabricate the different microchannels.

The perovskite precursor solution was prepared by a mixture of equimolar 0.5 M lead iodide (98.5%, Alfa Aesar) and methylammonium iodine (Lumtec) in gamma-butyrolactone (99%, Aldrich). The solution was stirred over night at 300 rpm and at 50 °C. 2 μl of the perovskite precursor was placed at one end of the laser engraved microchannel. The solution droplet was immediately pulled into the channel due to the capillary motion effect. Then the sample was placed on the hotplate and heated to 100 °C for 6 minutes. Afterward, a transparent layer of hydrophobic FluoroPel (CYNTONIX) was deposited by deep coating to protect the perovskite from degradation due to moisture. Finally, the sample was heated to 100 °C for 10 minutes and kept in vacuum in a desiccator for 24 hours to remove any residual solvent.

The fabricated samples were characterized by an Hitachi S800 Scanning Electron Microscope. The cyclic voltammetry, photocurrent and impedance measurements were carried out using a VersaSTAT 4 potentiostat. The light intensity at the sample location was measured to be

† Sections 3.2.1-3 are as presented in the published work at Organic and Hybrid Sensors and Bioelectronics XII. Vol. 11096. International Society for Optics and Photonics, 2019.

80 mW/cm^2. The light pulses were applied by switching on and off the light source. All experiments were performed at room temperature and under ambient condition.

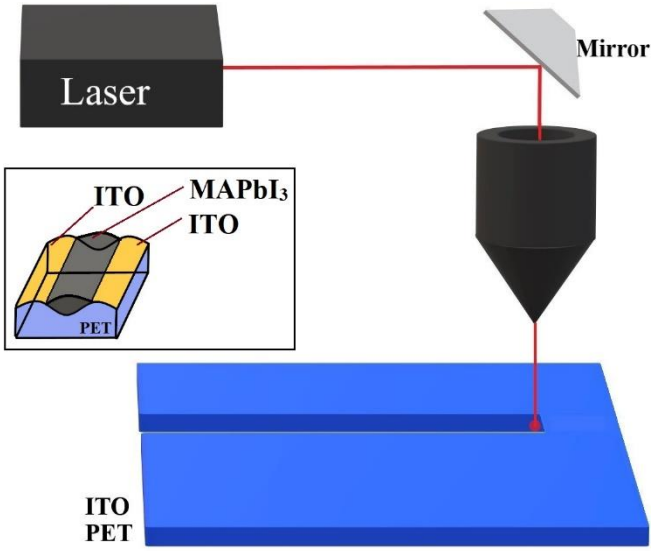

Figure 3.8 Schematic showing laser engraving of ITO coated PET and the schematic of the fabricated photodetector.

3.2.2 Result and Discussion

SEM images of the four different microchannels made by laser engraving are shown in Figure 3.9. Laser machining speed and power were varied in order to find the optimum values for each parameter. As the power increased (from 0.6 watt to 1.2 watt) the microchannel width increased, and deeper cracks were observed. The speed had a different effect, by increasing the laser speed (from 25.4 mm.S^{-1} to 50.8 mm.S^{-1}), a more uniform and shallower microchannel was made. The channel width of the microchannels shown in Figure 3.9 (a to d) are 117 μm, 100 μm, 197 μm, and 227 μm, respectively.

The four microchannels were filled with perovskite in order to make a photodetector. In addition, another photodetector was fabricated by forming a microchannel which was made by using the highest machining speed and PPI of the CO_2 laser. Using the highest speed and PPI

provided a higher degree of freedom in the choice of laser power which was increased to 2.4 watts.

The fabricated samples were named as A, B, C, D, and E which are shown in Table 1.

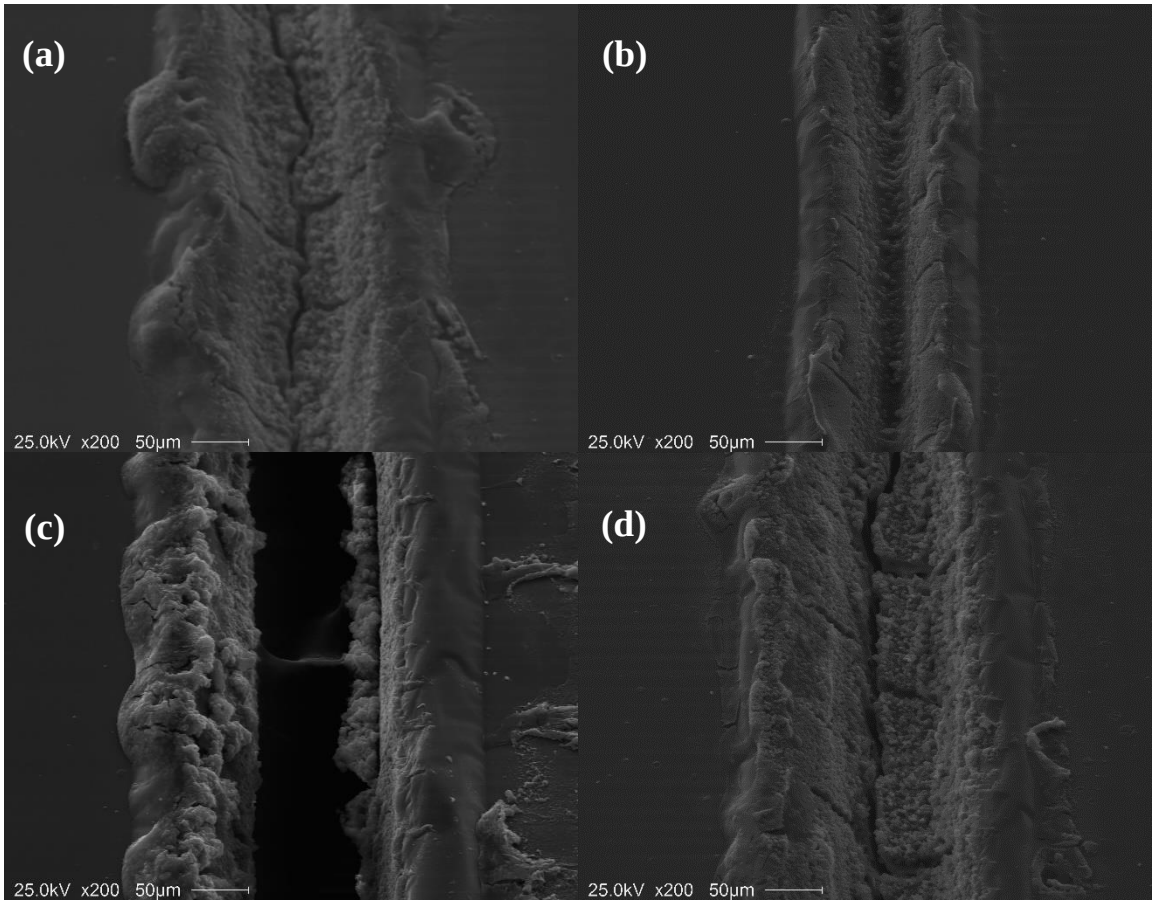

Figure 3.9 The SEM image of the microchannels engraved at different laser powers and speeds (images are taken at 44 degrees tilt angle): (a) 0.6 watt, 25.4 mm.S^{-1}, (b) 0.6 watt, 38.1 mm.S^{-1}, (c) 1.2 watt, 38.1 mm.S^{-1} and (d) 1.2 watt, 50.8 mm.S^{-1}.

Table 3.2 Laser engraving parameters of the fabricated samples.

Sample	**Speed (mm.S^{-1})**	**Power (watt)**	**PPI**
A	25.4	0.6	2500
B	38.1	0.6	2500
C	254	2.4	5000
D	38.1	1.2	2500
E	50.8	1.2	2500

Sample D and E showed a poor performance therefore we omit them from the rest of the study. The cyclic voltammetry of the samples A, B, and C measured in dark and under light

exposure are presented in Figure 3.10. Sample A and B showed a lower dark current. In the light condition, sample B presented the highest photocurrent of ~2.7 μA. The lower photocurrent of sample C while having a higher dark current is most likely because the perovskite precursor has gone over the ITO, cover a part of the electrodes, and made better contact. As a result, no significant change in the current was observed when the sample was under light illumination.

In addition, in dark condition, a hysteresis loop was observed in the I-V characteristics of all three samples. For samples A and B, the observed hysteresis loops were clockwise, but sample C showed a partly clockwise and partly counterclockwise loop (in larger bias voltages). As it can be seen in Figure 3.10.a, the area of the hysteresis loop of sample A was clearly larger than the observed loop in I-V characteristic of sample B, indicating a larger capacitive effect which can be due to the cracks and pores formed on the PET substrate during the laser engraving affecting the perovskite channel.

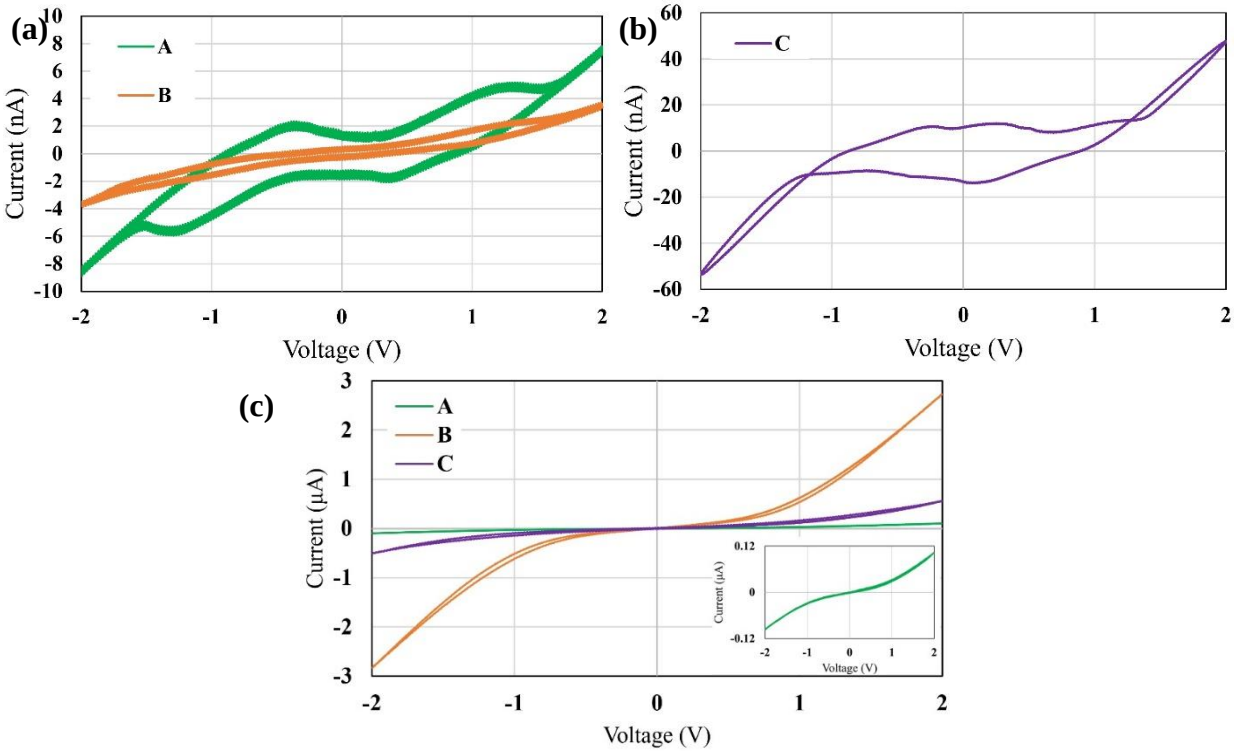

Figure 3.10 The cyclic voltammetry of the fabricated samples, (a and b) in dark and (c) under 80 mwatt.cm^{-2} light exposure.

The current response of the samples was measured at 2.0 V bias voltage when the light pulses of 20 seconds were illuminated to the samples (Figure 3.11). As it was expected, sample B showed the highest photocurrent and sample A showed the lowest photocurrent.

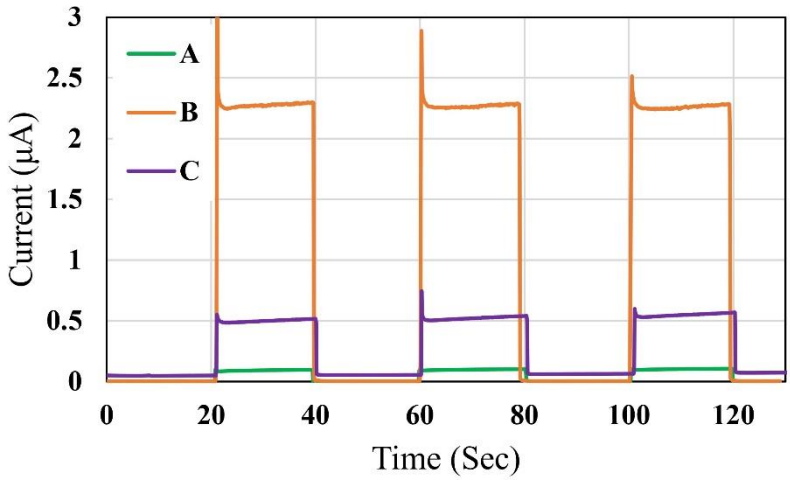

Figure 3.11. Current response of the photodetectors to light pulses at 2.0 V bias.

The amplitude and phase of the samples impedances were measured using the potentiostat. As shown in Figure 3.12, all sample had a pole which can be due to the capacitive effect exists between the perovskite grains. Sample C has shown a lower impedance which also confirms the I-V plot in dark condition.

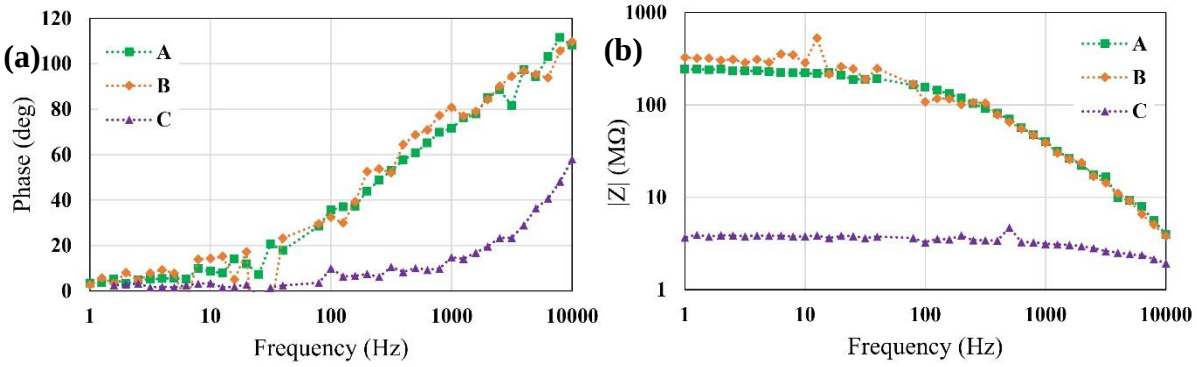

Figure 3.12 The bode (a) phase and (b) amplitude diagram of the fabricated photodetectors in dark condition.

As sample B represented the best performance, an equivalent circuit was proposed to model the impedance behavior of the device and the simulated data was fitted to the bode amplitude plot

of the impedance (Figure 3.13). The simulation was performed by EIS Spectrum Analyser software. For frequency ranges below 5000 Hz, a RC circuit model can be fitted to the bode amplitude plot. As it was seen in Figure 3.12.a the phase increased to values over 90 degrees in the higher frequencies (>2500 Hz). In order to model a circuit to get impedance phases higher than 90 degrees and considering potentiostat calculated all phases as positive numbers, an inductor can be added to the equivalent circuit. More studies are required to investigate the inductive behavior of the fabricated samples in high frequencies.

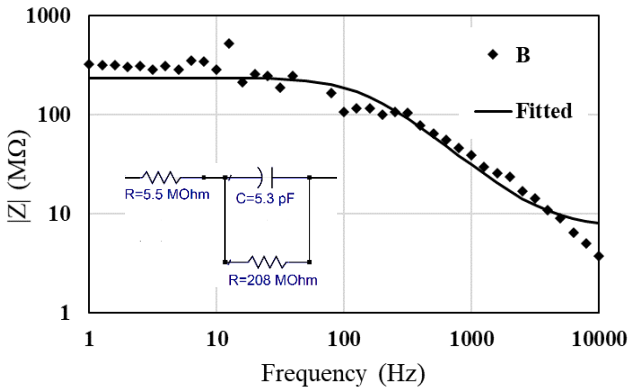

Figure 3.13 The simulated equivalent circuit bode plot fitted on sample B data points.

3.2.3 Conclusion

In conclusion, we fabricated several perovskite photodetectors by laser engraving ITO coated PET substrates to form a microchannel and then filling the channel by perovskite precursor. The most promising result was obtained by using the laser power of 0.6 watts, the laser speed of 38.1 $mm.S^{-1}$, and the laser pulse per inch of 2500 to engrave the microchannel. Along with simplicity, low cost, and cleanroom free advantages, our proposed fabrication method profits a clean and speedy micromachining which is beneficial for mass production.

Chapter 4: Stability in Photodetectors

The objective of this chapter is to study the stability of $CH_3NH_3PbI_3$ under CYTOP and FluoroPel coatings. In order to achieve this goal, a lateral structure photodetector was employed to facilitate fully encapsulation of perovskite. Here, as of our knowledge, for the first time, FluoroPel was used as a water repellent layer to enhance $CH_3NH_3PbI_3$ stability.[‡]

4.1 Experimental

The samples were made on 1 cm × 2 cm pieces of ITO coated polyethylene terephthalate, PET, (60 Ωsqr, Sigma-Aldrich). The substrates were laser engraved using a commercially available CO_2 laser (Epilog Fusion M2, 60 watts) which provides a laser beam of 10.6 μm wavelength printing in the vector mode with the lowest beam diameter of 76.2 μm. The macro channels were laser engraved when the laser fired 5000 pulses per inch (PPI) at the power of 0.6 watts and machining speed of 38.1 $mm.s^{-1}$.

The perovskite precursor solution was prepared by a mixture of equimolar 0.5 M lead iodide (98.5%, Alfa Aesar) and methylammonium iodide (Lumtec) in gamma-butyrolactone (99%, Aldrich). The solution was immersed in a bath of water and stirred overnight at 300 rpm and at 60 °C. 2 μl of the perovskite precursor was placed at one end of the laser engraved microchannel. The capillary motion helped the solution droplet to pull into the channel. Then the sample was placed on the hotplate and heated to 90 °C for 6 minutes.

[‡] Sections 4.1-4.4 are as presented in the published work in the journal of MRS Advances, 2020.

One group of four samples was prepared for the purpose of X-ray diffraction (XRD) characterization and another group of four samples were prepared for electrical and optical characteristics measurement. A 50 nm of CYTOP was spin-coated on two samples from each group and a 50 nm of hydrophobic FluoroPel (CYNTONIX) was spin-coated on the rest of the samples, to protect the perovskite from degradation due to moisture.

Four samples (one coated with CYTOP and one coated with FluoroPel from the first group and one coated with CYTOP and one coated with FluoroPel from the second group of samples) were kept in vacuum inside a desiccator and four other samples were kept under the ambient condition in order to study the effectiveness of hydrophobic coatings.

The fabricated samples were characterized by an Hitachi S800 and Hitachi SU70 Scanning Electron Microscopes. The cyclic voltammetry was carried out using a VersaSTAT 4 potentiostat. The light intensity at the sample location was measured to be 80 mW/cm^2. The light pulses were applied by switching on and off the light source. All experiments were performed at room temperature, under ambient condition and at the same time for all the samples. The schematic of the fabrication steps is shown in Figure 4.1.

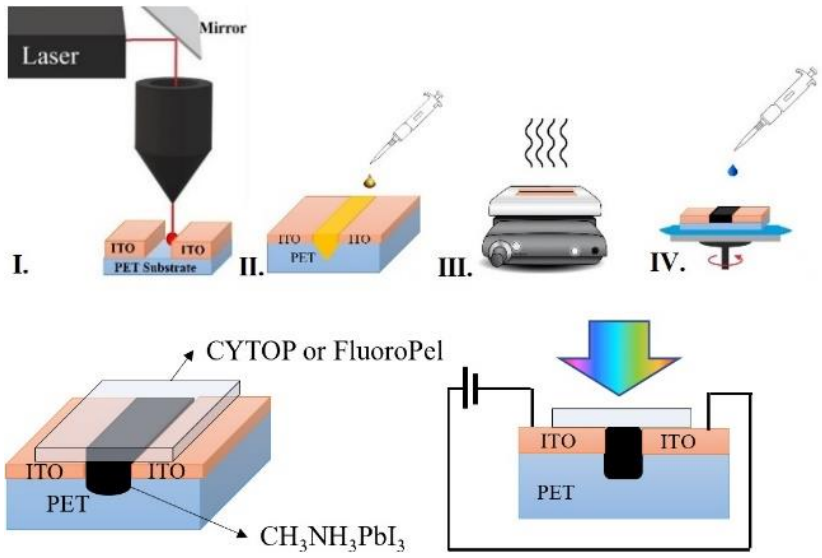

Figure 4.1 Schematic of the fabrication steps of the samples.

4.2 Characterization

The tilted (44 tilt degrees) view SEM image of the channel made by laser ablation is shown in Figure 4.2.a. Also, the top view SEM image of the perovskite layer grown inside the channel is presented in Figure 4.2.b.

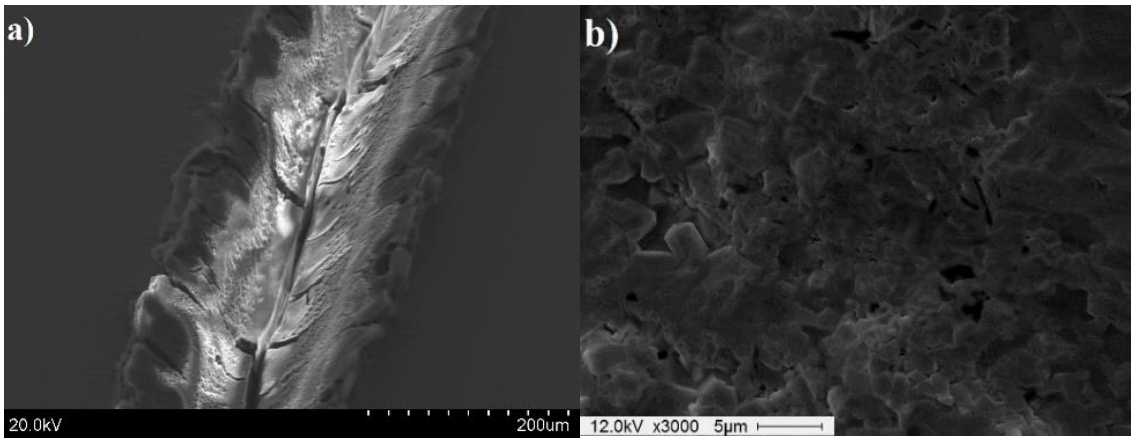

Figure 4.2 SEM image of the (a) the laser-engraved microchannel, (b) the perovskite layer inside the microchannel.

In order to estimate the crystalline quality of the perovskite layer, four samples were made by laser ablation of 19 microchannels (with a distance of 1 mm from each other) on the ITO coated PET substrates. XRD was performed over 22 days period on the mentioned samples as shown in Figure 3.

It has to be noted that the full XRD spectra had been shown in our previous work [[104]]. Therefore, here to simplify the comparison, the first two peaks are presented. The sharp peaks at 2Θ of 13.95 and 14.22 degrees were assigned to (002) and (110) planes of tetragonal $CH_3NH_3PbI_3$, space group I4/mcm [[142]]. In all samples, the perovskite crystal quality enhanced over 6 days. In addition, the PbI_2 diffraction peak at 2Θ of 12.6 degrees [[143]] which is known as a clear sign of the perovskite degradation, was not observed in any of the XRD data.

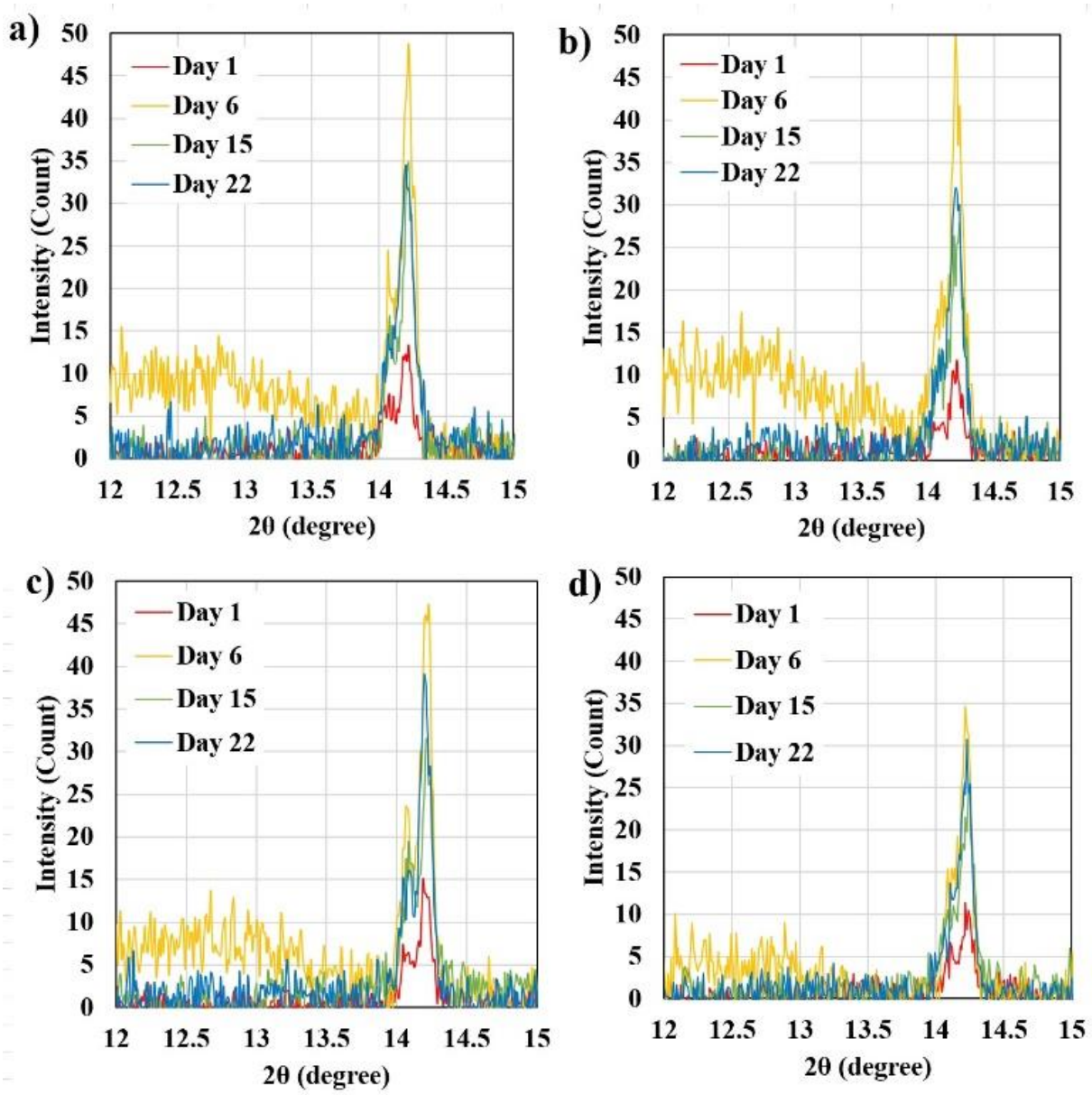

Figure 4.3 X-ray diffraction pattern of the arrays of $CH_3NH_3PbI_3$ microchannels formed on the PET substrate and coated with (a) CYTOP and kept in the desiccator, (b) CYTOP and kept under ambient condition, (c) FluoroPel and kept in the desiccator, and (d) FluoroPel and kept under ambient condition.

4.3 Result and Discussion

I-V characteristics of the sample were measured in dark and under light illumination of 80 mW/cm^2. In order to investigate the effectiveness of the two fluoropolymer coatings on the stability of the samples, the measurements were repeated over the 38 days.

The dark current of all samples (shown in Figure 4.4) dropped below 2 nA after the first week from the fabrication date. Afterward, no significant changes were observed in all the samples. On the other hand, the photocurrent (the current under illumination) varied over the time. The I-V plots of the sample under light exposure are presented in Figure 4.5. To clearly display the photocurrent variation for samples, the percentages of the change in the photocurrent is shown in Figure 6.

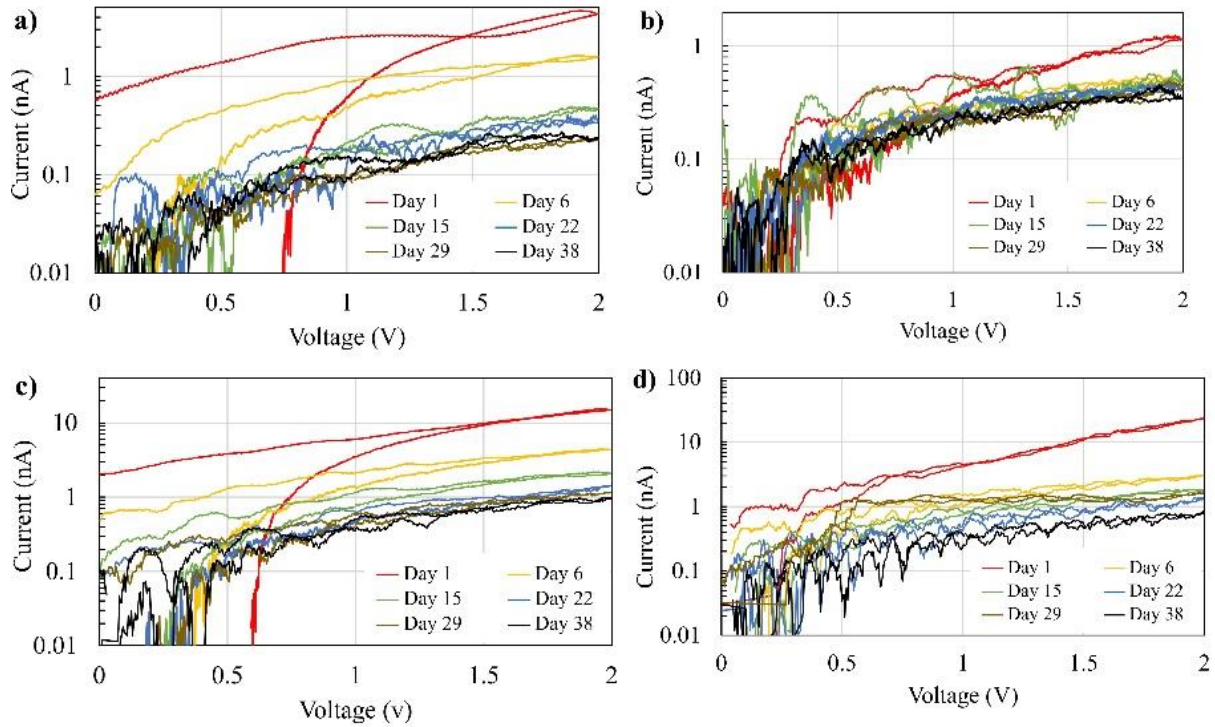

Figure 4.4 I-V characteristics of the ITO-$CH_3NH_3PbI_3$-ITO microchannels formed on the PET substrate and coated with (a) CYTOP and kept in the desiccator, (b) CYTOP and kept under ambient condition, (c) FluoroPel and kept in the desiccator, and (d) FluoroPel and kept under ambient condition, and in dark.

As can be seen in Figure 4.6 both the samples which were kept under ambient conditions (coated by CYTOP or FluoroPel) showed a significant increase in the photocurrent for 22 days after the fabrication. Also, regardless of the fluoropolymer coating material and the storage conditions, all the samples showed higher photocurrent frequently.

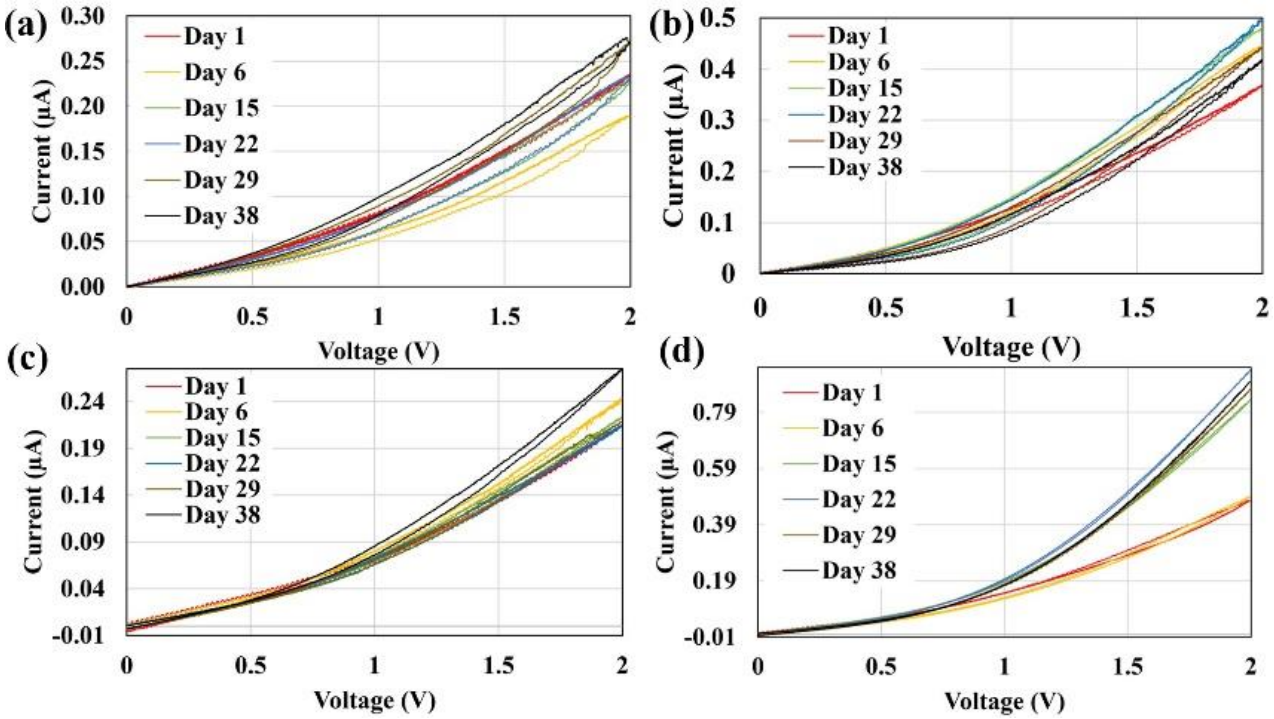

Figure 4.5 I-V characteristics of the ITO-$CH_3NH_3PbI_3$-ITO microchannels formed on the PET substrate and coated with (a) CYTOP and kept in the desiccator, (b) CYTOP and kept under ambient condition, (c) FluoroPel and kept in the desiccator, and (d) FluoroPel and kept under ambient condition, and under light illumination.

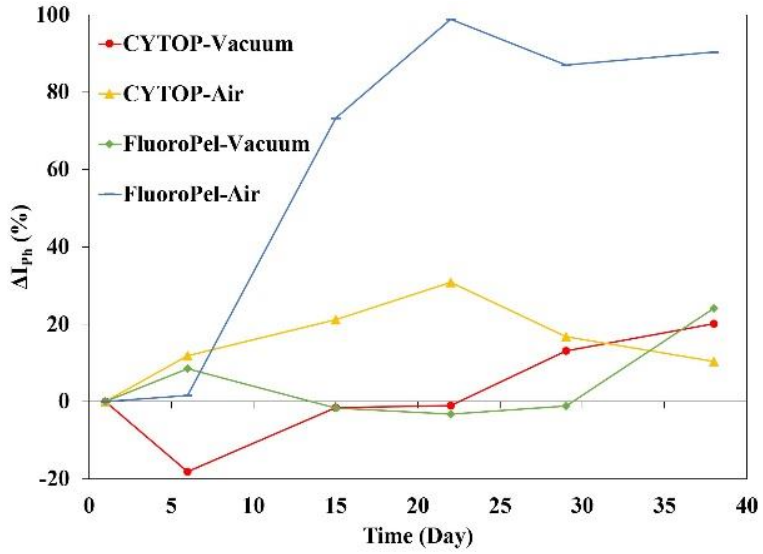

Figure 4.6 Comparison between the percentage of the change in the photocurrent of the samples at 2 V over the time.

Equation 1 was used to calculate the average measured changes in the photocurrent over 38 days for each sample. The Table 4.1 shows the calculated values. The two samples kept under

ambient condition were found to be more unstable and showed higher variation in the photocurrent. This may prove that the coating layers are not fully defect-free. The sample coated with FluoroPel and kept in vacuum was the most stable sample and showed the lowest average change in the photocurrent.

$$\Delta I_{ph}= \frac{\frac{I_{day1}-I_{day1}}{I_{day1}}+\frac{I_{day6}-I_{day1}}{I_{day1}}+\frac{I_{day15}-I_{day1}}{I_{day1}}+\frac{I_{day22}-I_{day1}}{I_{day1}}+\frac{I_{day29}-I_{day1}}{I_{day1}}+\frac{I_{day38}-I_{day1}}{I_{day1}}}{6}\times 100 \qquad (4\text{-}1)$$

Table 4.1 The average of the percentage of the change in the photocurrent.

	CYTOP Vacuum	**CYTOP Air**	**FluoroPel Vacuum**	**FluoroPel Air**
Avg. ΔI_{ph}(%)	10.79	18.21	7.71	70.26

The unusual behavior of the raise in the photocurrent over the time needs to be investigated along with the higher peak intensity in X-Ray diffraction data. The absence of the PbI_2 diffraction peak at 2Θ of 12.6 degrees confirms that the formation of PbI_2 due to the perovskite decomposition in this unique lateral structure is unlikely. Since the perovskite layer is encapsulated from the two walls of the microchannel and the PET substrate underneath. In addition, the perovskite upper part is coated by a fluoropolymer.

On the other hands, it has been reported that the high dipole moment of the strong polar C-F bond in fluoropolymers can favorably change the electrical characteristics of the device [144]. As it was discussed before, the grown perovskite is in the tetragonal phase which is ferroelectric [123]. Since the light was illuminated from the top-side of the samples, it passes through the polymer coating, and is mainly absorbed by the part of the perovskite which is in contact with the fluoropolymer. The enhance in the photocurrent over a long period of time can be due to the effect

of the high dipole moment of the strong polar C-F bond in fluoropolymers on aligning of the domains in the ferroelectric perovskite layer.

Sharpening of the perovskite (002) and (110) planes diffraction peaks after 6 days from the fabrication time indicates more ordered crystalline domains by passing the time which can be as the result of nearly fully encapsulating the perovskite inside a microchannel and coating it by a fluoropolymer. More study is needed to investigate the effect of perovskite confinement during the growth and encapsulation.

4.4 Conclusion

In summary, we employed two fluoropolymers as the encapsulation layer to protect the perovskite microchannel from degrading due to exposure to oxygen and moisture. Four photodetectors were fabricated using laser micromachining. Two photodetectors were coated by CYTOP and the other two photodetectors were coated by FluoroPel. To investigate the effect of the ambient environment, one photodetector from each coating was kept in the vacuum inside a desiccator and one photodetector was kept under ambient environment.

Unexpectedly, the average photocurrent of all four samples increased over 38 days from the fabrication time. The sample which was coated by FluoroPel and kept in the vacuum was the most stable sample. This study suggests the use of FluoroPel in perovskite solar cell applications.

Chapter 5: Ion Migration and Piezo-Photocurrent Modulation

Recently, $MAPbI_3$ has been found to have piezoelectricity. Alignment of polarized domains via the polling process can generate a permanent polarization in the material, but in such a form, both dark and photocurrents are expected to be increased by reducing barriers under an external force (leading to an insignificant improvement in the device sensitivity) [145].

Many efforts have been made to boost the functionality of fabricated lead halide perovskite photodetectors [146]. Recent investigations have revealed that the piezoelectric property of $MAPbI_3$ [88-92] causes a piezo-phototronic effect. This effect can be employed to reduce the structural barrier under illumination to enhance the photoresponse of a $MAPbI_3$ single crystal photodetector [91]. It has been shown that the piezoelectric coefficient increases by several-fold under illumination [90].

Ion migration has been suggested as a mechanism for photo-induced self-polling effect. This enhances the photocurrent in $MAPbI_3$ based photovoltaic devices under illumination by accumulating ions at the interfaces and making a p-i-n homojunction in the perovskite layer [147-149].

In this chapter, the effect of external forces in different directions on the photocurrent of the photodetector structure which was introduced in the previous chapters has been investigated. The device was also characterized by SEM, XRD, AFM, and profilometer.[§]

[§] Sections 5.1-5.4 are as presented in the published work in the journal of Advanced Electronic Materials 2019.

5.1 Experimental

The perovskite precursor solution contained a mixture of equimolar 0.5 M lead iodide (98.5%, Alfa Aesar) and methylammonium iodine (Lumtec) in gamma-butyrolactone (99%, Aldrich). The solution was stirred over night at 1200 rpm and at 50 °C.

1.5 cm×2 cm piece of ITO coated polyethylene terephthalate, PET, (60 Ωsqr, Sigma-Aldrich) was cut and placed into a microcutting tool that comprises an X-Acto knife blade protruding wedge into the ITO coated PET substrate to form a micro-channel with ~100 µm width. 2 µl of the perovskite precursor was placed at one end of the channel. The solution droplet was immediately pulled into the channel due to the capillary motion effect. Then the sample was placed on the hotplate and heated to 90 °C for 6 minutes. Afterward, a ~50 nm transparent layer of water repellent fluoropolymer CYTOP (AGC Chemicals) was deposited by spin coating to protect the perovskite [150]. Finally, the sample was heated to 100 °C for 90 seconds followed by another annealing process for 30 minutes at 90 °C and kept in the desiccator for 24 hours to remove any residual solvent. Figure 22.a illustrates the process of preparing the photodetector. SEM, XRD, AFM, and profilometer were employed to characterize the perovskite channel.

For the I-V characterization under the light, dark, compressed and released conditions, a VersaSTAT 4 potentiostat was connected to the device electrodes inside a dark box. A solar simulator (RST, Radiant Source Technology) was used as the light source. The light intensity at the sample location was measured to be ~80 mW/cm^2. In-house designed setups were used for bending the devices and applying normal forces while they were tested under the dark and light conditions. Figure 22.b shows the schematic of a home-made vice setup that was used for bending the device by turning the screw (Figure S1.a in the Supporting Information). For the normal tests (Figure 22.c), a pneumatic actuator was used to apply the pressure over the device while the light

was illuminated through the transparent window at the back of the device (Figure S1.b). Both setups were designed to be placed in the dark box connected to the light source.

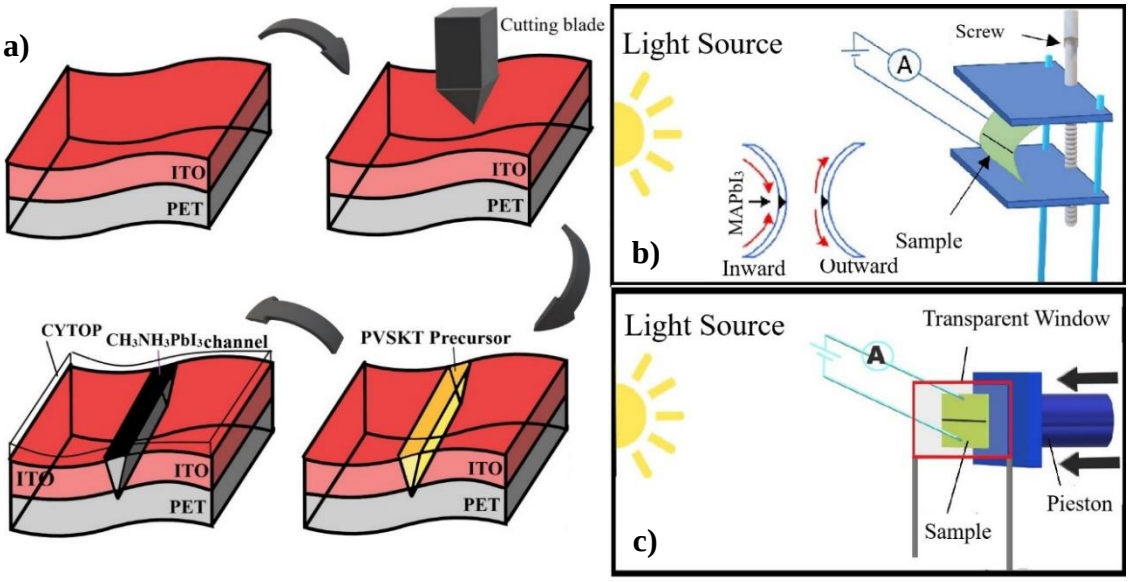

Figure 5.1 Schematic of (a) the fabrication process steps, (b) the setup used for bending the device and (c) the setup used for applying normal forces.

5.2 Device Characterization

The top view SEM image of the sample (Figure 5.2.a, b and c) showed that the channel is filled with a packed layer of perovskite. As it can be seen in Figure 5.2.b the grains sizes of the perovskite layer vary across the channel. Larger grains were observed at the edges of the channel which could be the result of the coffee ring effect [151]. For further investigation, the thickness profile of the channel was measured at different spots along the channel (Figure S2). The profile image showed a groove shape with two standing walls before the channel was filled with perovskite. After filling, at the beginning of the channel where the capillary motion started, perovskite fully filled the channel and crystalized over the walls. As it reached toward the end, the thickness of the perovskite decreased (Figure S.3).

Using AFM in the contact mode, the morphology of the perovskite in the channel was studied on a sample without the CYTOP coating. The surface height morphology is shown in

Figure 5.2.d demonstrating a relatively rough surface. The XRD pattern (Figure 5.2.e) was measured on a sample with an array of parallel channels with 300 µm distance between them while all the channels were filled with perovskite using the capillary motion. The pattern displayed five sharp peaks at 2θ of 14, 28.3, 31.8, 40.5 and 43 degree indicating the channels were filled with tetragonal-phase $MAPbI_3$ [152]. The absence of a diffraction peak at 12.65 degrees suggests that the level of the PbI_2 impurity phase is negligible [21]. The wide broad peak at 25 degrees is due to the PET substrate.

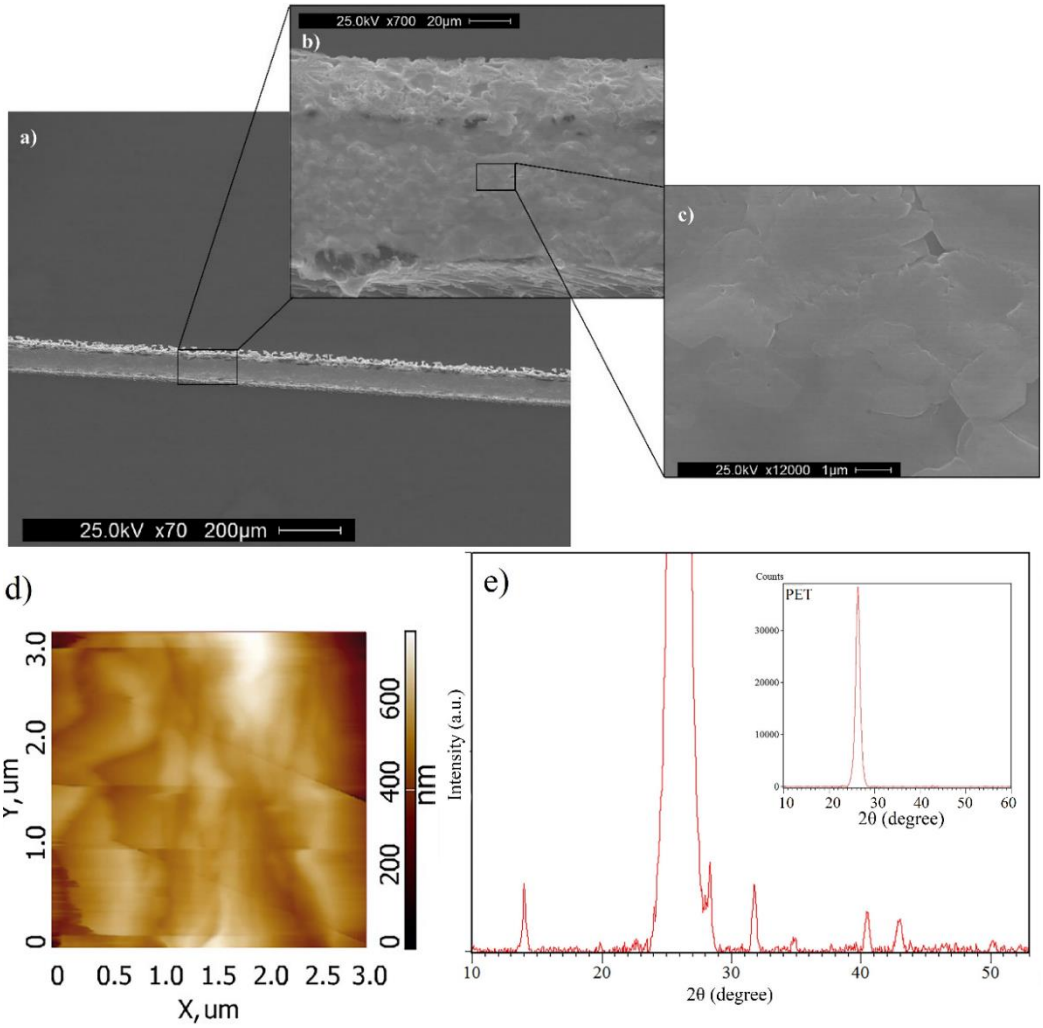

Figure 5.2 (a, b and c) Top view SEM image of the fabricated perovskite microchannel at different zooming levels. (d) AFM height image of $MAPbI_3$. (e) X-ray diffraction pattern of the arrays of $MAPbI_3$ microchannels formed on the PET substrate. The inset picture shows the XRD pattern of the PET substrate.

5.3 Results and Discussion

To study the effect of stress perpendicular to the applied electric field across the perovskite, the device was placed in the compressing setup shown in Figure 5.1.c (Figure S1.a) that was equipped with a pressure regulator to adjust the applied stress to the sample. Then the I-V measurement was carried out with the voltage ranged between -2.0 V and +2.0 V under illumination while the device was compressed or released at different normal pressures. Also, the device was tested in the dark in the relaxed mode (no pressure) as the reference. As shown in Figure 5.3.a, a non-linear I-V characteristic was observed which is likely due to the formation of Schottky junctions between the ITO electrodes and $MAPbI_3$ [141, 153]. The response under different pressures clearly shows that the current under illumination (photocurrent) increased with the pressure. Also, the low dark-current verifies the behavior of the device as a photodetector. At +2.0 V biasing, the photocurrent magnitude reached from 3.5 μA at the no pressure condition to 6.9 μA at the highest normal force of 340 kPa which is 97% higher than the released state.

To investigate the effect of compressive and tensile forces across the channel, the setup shown in Figure 22.b (Figure S1.b) was used to bend the device inward (concave shape) and outward (convex shape), respectively. The I-V characteristics of the device were measured again in the voltage range of -2.0 V and +2.0 V and as an example under one curvature for each bending direction (inward or outward). The inverse of the curvature radius is reported as the curvature, κ, in Figure 5.3.b. The results showed a higher photocurrent when the device was under a compressive force (inward bending). At +2.0 V biasing, the photocurrent magnitude was 4.5 μA at the inward curvature of 0.3 cm^{-1}, which was ~30% larger than that at the flat position. In contrast, the measured photocurrent at the outward curvature of -0.3 cm^{-1} had the lowest magnitude of 2.8 μA which is ~20% lower than the photocurrent at the flat position.

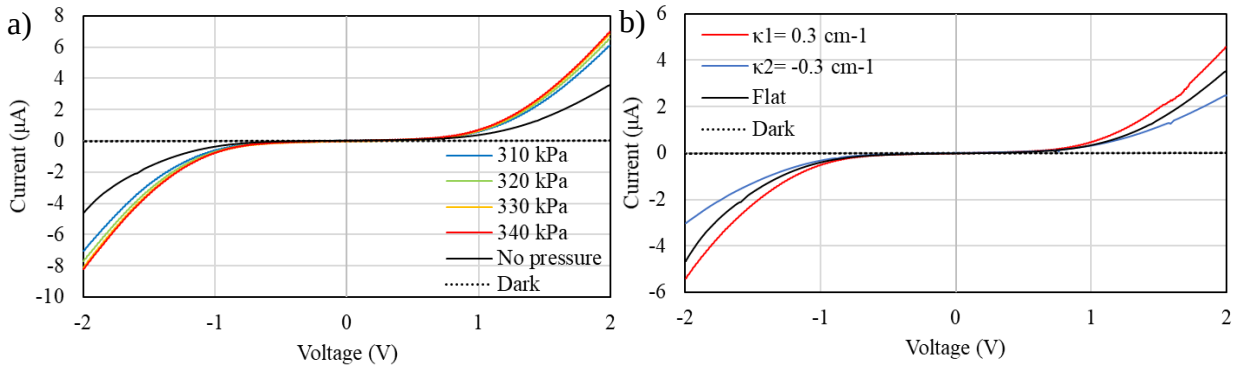

Figure 5.3 I-V characteristics of the fabricated device in the dark (no pressure and flat condition) and under ~80 mW/cm^2 light exposure while the device was tested (a) under different normal pressures and (b) at different bending curvatures (inward and outward bending curvatures are shown with positive and negative numbers, respectively).

To study the transient response of the current, the sample was biased at 2.0 V and a constant normal pressure was applied when the light was switched on and off every 20 sec (Figure S4). The results from different experiments under different normal forces are presented in Figure 5.4.a. In the first few cycles of light exposure under no external pressure, the photocurrent showed a constant increase with time until it reached a stable value after a few cycles. The following cycles were tested when the sample was under a constant pressure. The current pulses show a higher photocurrent at higher pressures, after four steps of compression from 310 kPa to 340 kPa, the device was released, and the photocurrent was measured to be less than all photocurrents under pressure. However, its value was higher than the primary state before applying any pressure. To ensure that the change in the photocurrent is the effect of the normal force, the dynamic respond of the photocurrent to the normal forces was measured by compressing and releasing the device under light illumination (Figure 5.5.a). Fast and reversible response to the normal force was observed.

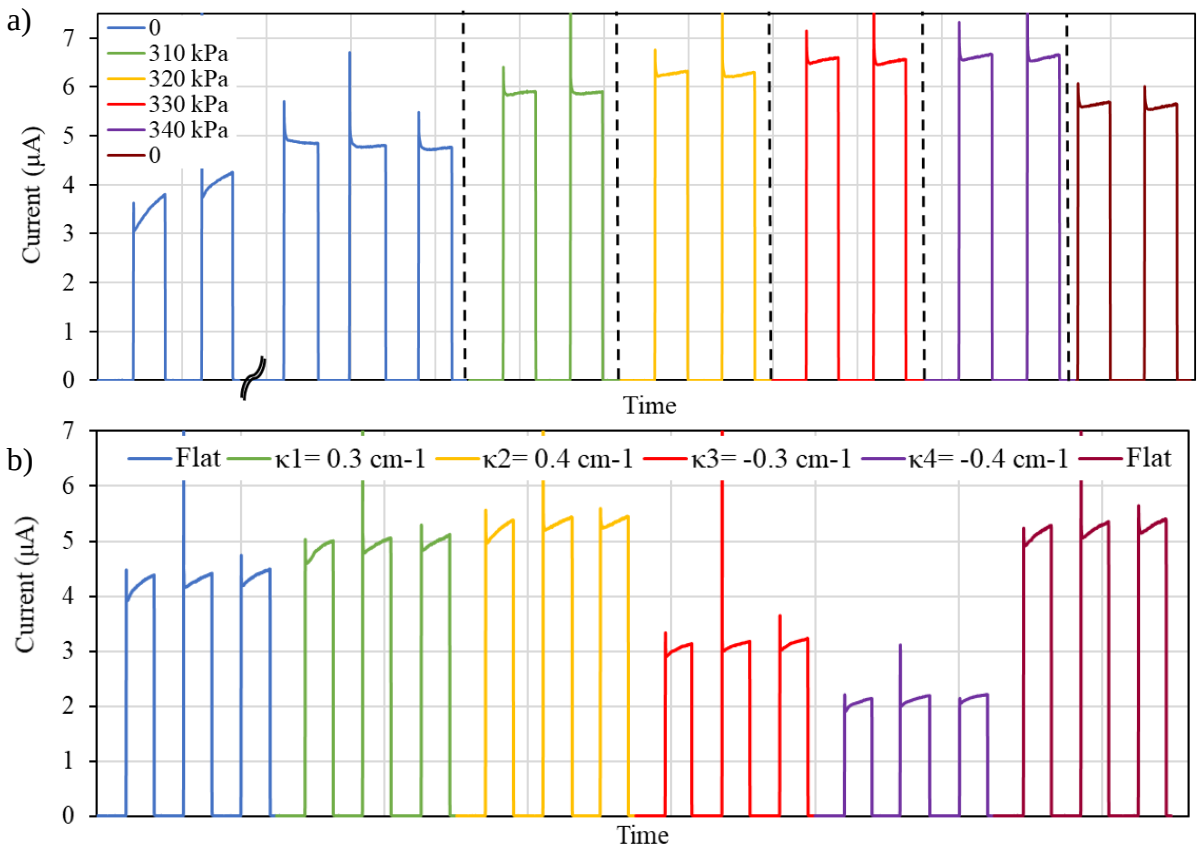

Figure 5.4 Current response of the photodetector to light pulses at 2.0 V bias under different compressive/tensile pressures. (a) under different normal pressures. (b) under different bending curvatures (inward bending is showed with the positive number and outward bending with a negative sign).

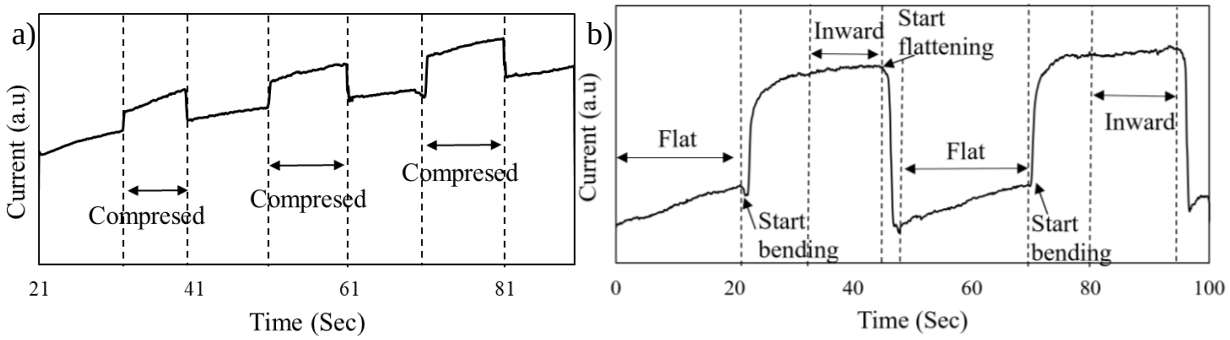

Figure 5.5 Dynamic photocurrent response of the fabricated sample at 2.0 V bias under continuous illumination to (a) a normal force and releasing for 3 cycles, (b) manually bending into inward position and flattening for 2 cycles.

Static and dynamic responses to the compressive and tensile forces aligned with the applied electric field were measured using the fabricated setup in Figure 22.b for bending the sample

inward and outward at different curvatures. Figure 5.4.b shows the effect of the static force under different curvatures. The higher inward curvatures resulted in the higher photocurrent. Changing the bending curvature from inward to outward resulted in a lower photocurrent. However, returning to the flat position, the photocurrent increased to a higher level than the primary flat state photocurrent. This can be due to the illumination history and electric field history as reported before [154]. To ensure that the change in the photocurrent is the effect of bending the device, dynamic response of the photocurrent was measured by bending the device under illumination (Figure 5.5.b).

For the better understanding of this apparent piezoelectric effect in the perovskite photodetector, the device was tested in the dark under various pressures and bending conditions. The dark-currents versus time are shown in Figure 27 at +2.0 V bias voltage. Although some changes were observed in the dark-current when a mechanical stress was applied, the changes were not coherent with the magnitude and direction of the forces. More importantly, the variation in the dark-current was less than 12% under different normal forces (Figure 27.a) while a coherent change of photocurrent up to 30% was observed for the same range of the forces. Similarly, the dark-current under the bending conditions did not show any specific relation to the curvature. Even as shown in Figure 6.b, the dark-current was exactly the same for the flat position and the max inward bending at the curvature of κ=0.4 cm^{-1}. The coherent response of the photocurrent to the external forces and the lack of any relationship between the dark-currents and the forces clearly indicate that the change in the photocurrent is not due to the mechanical contacts between the perovskite and ITO. Furthermore, much larger boosts in the photocurrent and smaller changes in the dark-current suggest that the mechanism of governing the charge transport through the device is not a simple piezoresistive effect [155].

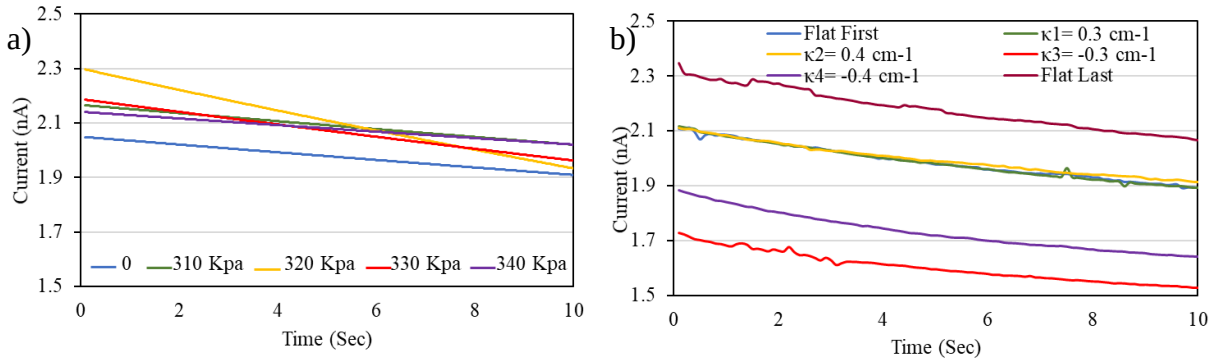

Figure 5.6 I-t responses of the device in dark, (a) under different normal pressures and (b) at different bending curvatures.

To ensure the stability of the device during the measurement, the dark current-voltage characteristic of the device was measured by the scan rate of 50 mV/sec, once before starting the measurements and compared with the dark current-voltage characteristic of the device after more than 100 cycles of all tests that were performed including I-V measurements and I-t transient characteristics under light and at different pressures or bending positions. The results are shown in Figure S6. The I-V of the final test was in a good match with the first I-V measurements which proves that no significant cracking happened.

The performance of the photodetector can be evaluated by sensitivity (*S*) and responsivity (*R*) [156], which are defined by the equations (5-1) and (5-2) respectively:

$$S = \frac{I_{light} - I_{dark}}{I_{dark}} \times 100 = \frac{I_{ph}}{I_{dark}} \times 100 \qquad (5\text{-}1)$$

$$R = \frac{I_{ph}}{P}\ (A/W) \qquad (5\text{-}2)$$

where, I_{light} is the measured current under illumination, I_{dark} is the dark-current, I_{ph} is the difference between measured current under illumination and the dark-current (=I_{light} - I_{dark}) which in our device is almost equal to I_{light}, P is the optical power received by the active area of the photodetector. The sensitivity and responsivity of the device were measured and calculated at +2.0 V bias voltage while the device was exposed to nearly 80 mW/cm^2 power density. As shown in

Figure 5.7, the device sensitivity and responsivity increased by bending into inward positions and applying normal forces while the sensitivity and responsivity of the device decreased when it was bended into outward positions. The sensitivity of 2.08×10^5 A/A and responsivity of 9.1 mA/W at +2.0 V flat position and no applied stress were calculated. As we increased the applied normal pressure the amount of sensitivity and responsivity raised to the highest point of 3.25×10^5 and 14.56 mA/W while the device was under 340 kPa normal force. This level of sensitivity is two orders of magnitude higher than a previously reported device under a normal compressive pressures [91].

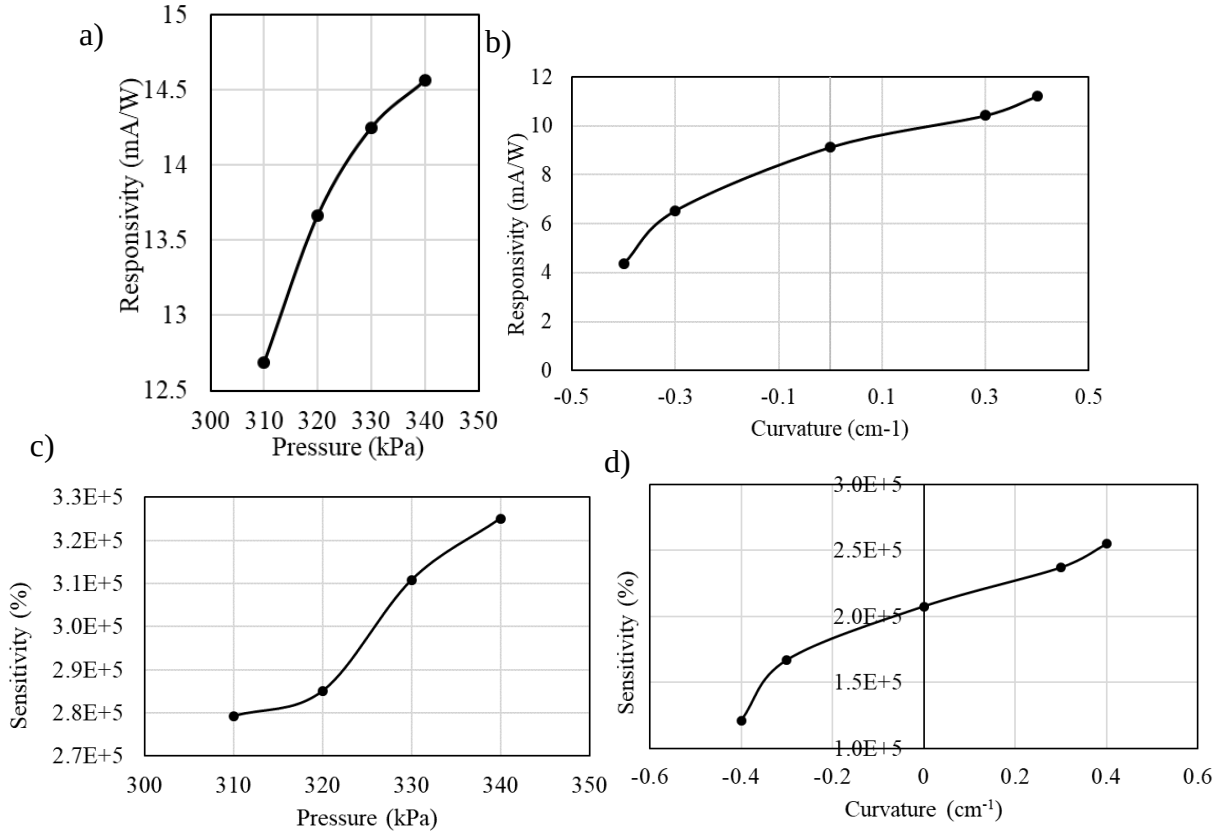

Figure 5.7 The responsivity of the device (a) under different normal pressures, (b) under different curvatures. The sensitivity of the device (c) under different normal pressures and (d) under different curvatures. All plots are measures at +2 V forward bias and ~80 mW/cm^2 illumination power density.

The effect of pressure on the optical and electrical properties of $MAPbI_3$ has been investigated by several groups [52, 157-161]. It has been shown that increasing the pressure to few

GPa may affect carrier life time, bandgap, tilting of $[PbI_6]^{4-}$ octahedra and yielding new phases [52, 162]. However, the applied pressure in our experiments was four orders of magnitude lower than the pressure level required for a crystalline change in the material.

To explain the photocurrent modulation by the applied stress/pressure, the band-bending at the ITO-$MAPbI_3$ was considered as a Schottky contact [141]. In the absence of any electric field (no DC biasing) and in the dark, the device is in equilibrium with a symmetrical band bending at the both ITO-$MAPbI_3$ junctions (Figure 5.8.a). However, in the presence of light when an external electric field is applied across the perovskite channel (biasing at 2.0 V across 100 μm), migration of interstitial iodine accelerates and ions/vacancies drift toward the ITO electrodes [163, 164]. This break the symmetry of the band structure. As explained by Yuan et al. [148], the drift of ions/vacancies accumulates the positive ions at the proximity of the anode resulting in an n-type doping of the $MAPbI_3$ layer. Similarly, the accumulation of negative ions/vacancies close the cathode is expected to induce a p-type doping region and consequently forms a p-i-n homojunction in the perovskite material that modifies the band bending at the ITO-$MAPbI_3$ interfaces (Figure 5.8.b). This process is known as light-induced self-poling (LISP) effect [147-149].

Illumination generates a large number of electrons and holes. Through the aforementioned mechanism, holes can more easily hop or tunnel through the narrowed barrier at n-$MAPbI_3$/ITO side and electrons can pass though p-$MAPbI_3$/ITO side. The time-scale of the ion-migration-induced barrier modification is reported to be in the order of several minutes [130]. This can be the reason for the observed non-steady state increasing photocurrent in the first pulses in Figure 5.4 and Figure 5.5. Also, the history effect observed after extended illumination time under a constant electric field can be due to the same ion migration effect. The fact that the tested sample

recovered its original characteristic in the dark (Figure S6) supports the theory of LISP being responsible for the suggested band diagram in Figure 5.8.b [164].

However, the LISP effect alone does not explain the apparent piezo-photocurrent modulation. In general, electric polarization can have three primary contributions: electronic, ionic, and dipole reorientation-related [145]. The tetragonal phase of $MAPbI_3$ has a natural polarized structure with the previously reported ferroelectric and piezoelectric properties [87, 89]. In the polycrystalline form, domains are randomly distributed. The low external electric field of 0.02 V/μm which is also weakened by the internal electric field due to ion migration may not be large enough for the poling process. However, the accumulation of positive and negative ions near the ITO-$MAPbI_3$ interfaces can establish a large electric field near the interfaces. This high electric field can align domains and make polarized structures at the perovskite sides close to the ITO-$MAPbI_3$ interfaces such as the polarization mechanism induced by the poling process in piezoelectric materials. With this light-induced self-poling at the interfaces, it is likely that the polarized regions near the interfaces have been formed that were responding to the external mechanical forces. Therefore, although we have not performed poling process purposely, the response of this polarized structure to the mechanical stresses can be called an apparent piezoelectric effect.

Bending inward or compressing the perovskite induces an electric field in the same direction as the external field, resulting in further band bending in favor of lowering the barrier for a larger current to pass through the device. In contrast, the outward bending may generate an electric field opposite of the external field direction that reduces the current in the device. More studies are required for a better understanding of the possible mechanisms, and also measuring the piezo coefficients at different directions.

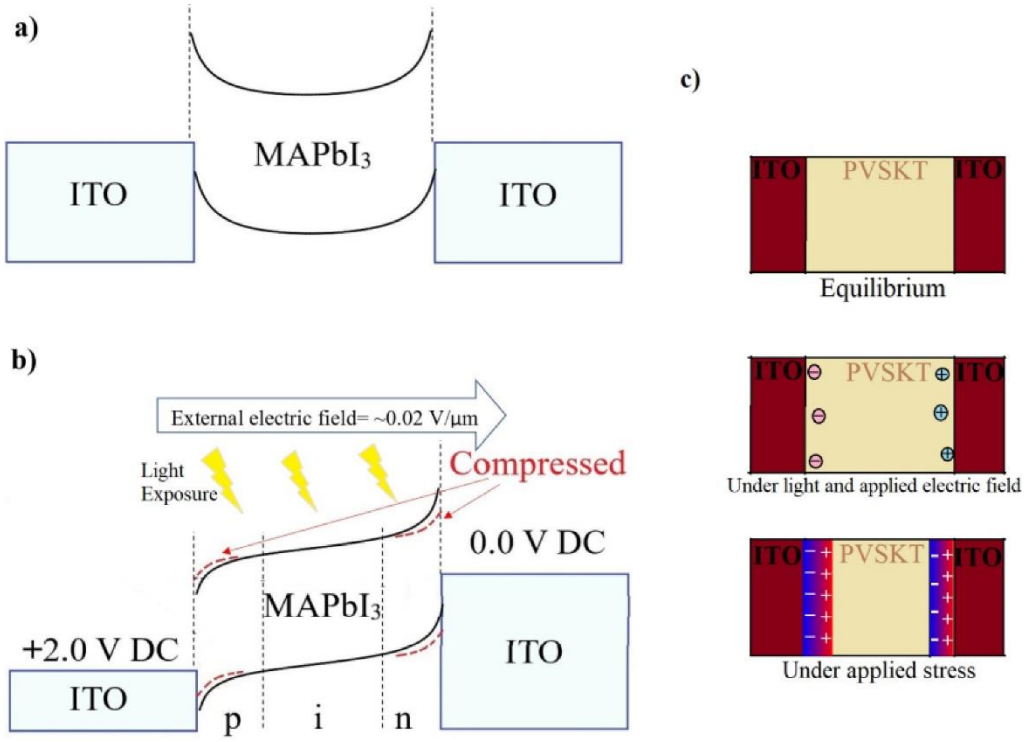

Figure 5.8 Energy diagrams of the device (a) in equilibrium and (b) under the DC biasing. Both light and mechanical stress can affect the band bending. (c) schematic of the device structure at three states of equilibrium, under light and applied electric field (ion/vacancies accumulate at the interfaces) and under applied stress.

5.4 Conclusion

In summary, here we fabricated an ITO–$MAPbI_3$–ITO lateral structure. This unique structure demonstrated an apparent piezo effect for two different directions of stress. Also, the induced piezo electric field was found to be more effective under illumination perhaps due to the LISP effect. The photocurrent and consequently responsivity and sensitivity of the device were enhanced while the sample was under normal pressure and at inward bending positions. At the highest state, the responsivity enhanced from 9.1 mA W^{-1} to 14.56 mA W^{-1} and I_{ph}/I_{dark} from 2.08 × 10^3 to 3.25 × 10^3. While more study is needed for better understanding of the mechanisms of charge transport and the effect of stress and light on the electrical behavior of the device, the observed apparent piezo-phototronic effect can be employed to design photosensors with a higher level of sensitivity.

Chapter 6: Methylammonium Lead Iodide Transistor

As it was discussed in the previous chapters, motivation for using perovskite is their low-cost. Additionally, the solution processability of lead halide perovskites is an advantage for making low-cost devices with simple fabrication methods. Yet, using their extraordinary electro-optical properties for making highly sensitive phototransistors.

Several groups have reported on the different $MAPbI_3$–based field-effect transistor (FET) structures [21, 22, 28, 30, 33, 44]. A challenge in fabrication of $MAPbI_3$ FETs is the incompatibility of the standard patterning techniques such as photolithography and E-beam lithography to be applied for perovskites, due to the sensitivity of $MAPbI_3$ to polar solvents [27] and their low activation energy for degradation [165]. The other challenges are instability of transistors under ambient conditions, biased at high electric fields [166] and a limited current modulation at room temperature [29].

In this chapter, we introduced two different designs to make perovskite photodetectors. The first phototransistor is made on a flexible PET by laser engraving and the second designed phototransistor was made using a pneumatic nozzle printer. The electrical and electro-optical properties of the fabricated phototransistors are studied.

6.1 Fabrication of Perovskite Transistors Using Laser Ablation

Portable and wearable applications of transistors require the use of lightweight flexible substrates. Different technologies and materials have been employed to develop flexible phototransistors by low-temperature fabrication methods [167]. Among the materials that are compatible with low-temperature processes, organic semiconductors suffer from low mobility

[168] and metal oxide semiconductors have complicated and costly deposition techniques in order to reach a high-quality film [169].

Thus, the combination of suitable perovskite transistor architectures with fast and reproducible patterning methodologies on flexible substrates can accelerate the progress towards industry-relevant applications [66]. Here we have demonstrated a $MAPbI_3$ transistor with a lateral structure made using an extremely simple and low-cost fabrication process. As of our knowledge, the device is the first $MAPbI_3$ channel transistor produced on a flexible plastic sheet.

6.1.1 Experimental

Perovskite precursor was prepared by mixing 0.5 M PbI_2 (98.5%, Alfa Aesar) and 0.5 M MAI (Lumtec) in GBL (99%, Aldrich) and keeping it on the hotplate at 60°C overnight. The sample was fabricated using 1 cm×1 cm pieces of ITO coated PET sheet (60 Ωsqr, Sigma-Aldrich). A 200 µl of PMMA in chlorobenzene (0.369 g in 3 ml chlorobenzene) was spun coated at 1000 rpm for 40 seconds. This layer was used as an isolating layer between ITO (drain and source contact material) and the gate contact.

After chlorobenzene was evaporated, the sample was laser engraved (Epilog Fusion M2, 60 watt) at the power of 0.6 watts, speed of 38.1 $mm.s^{-1}$ and pulse per inch (PPI) of 5000. Then the laser engraved channel was filled with a 2 µl of the perovskite precursor solution using the capillary force when a droplet of the solution was placed at the one end of the channel. The sample was placed on the hotplate at 85°C for 6 minutes.

After that, for making the gate dielectric, a 50 µl of CYTOP CTL-809M (AGC Chemicals, Tokyo, Japan) was spun coated at 2000 rpm for 40 seconds and formed a ~1 µm thick CYTOP layer. Afterward, the sample was kept inside the desiccator overnight in order to remove any

residual solvent. Then a very narrow piece of Cu tape was placed on the channel to serve as the gate contact. For better adhesion, a layer of Acrylic (MG Chemicals) was poured on the Cu tape.

The sample was characterized by SEM (Hitachi SU70), XRD (Bruker D8 Advance) and a two channels source measure unit (SMU) (Keithley 2602A). All the measurements under light were performed when the sample was illuminated by a solar simulator (RST 300S) at 80 mW/cm^2 optical power. A schematic of the device structure is illustrated in Figure 6.1.

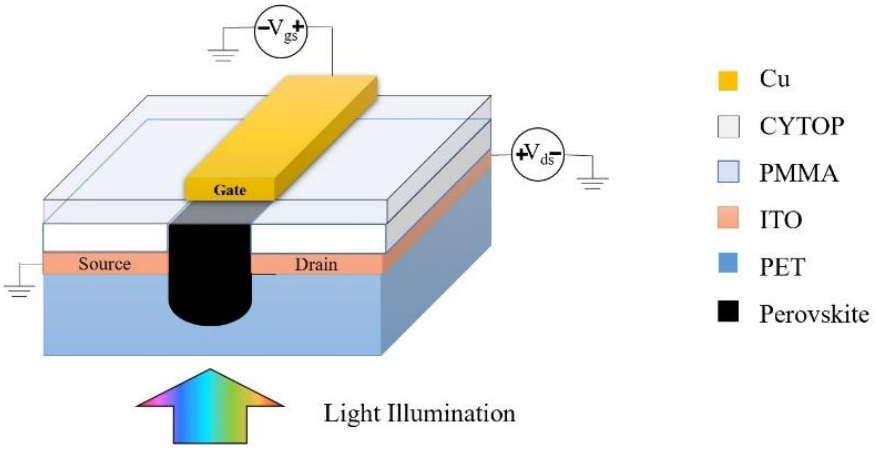

Figure 6.1 The schematic of the fabricated perovskite transistor by laser engraving.

6.1.2 Result and Discussion

The SEM image of the laser engraved channel is shown in Figure 6.2.a. The channel width was measured to be ~60 µm. As it was expected from our previous devices [102, 104, 123], the crystallized precursor inside the microchannel formed tetragonal phase $MAPbI_3$.

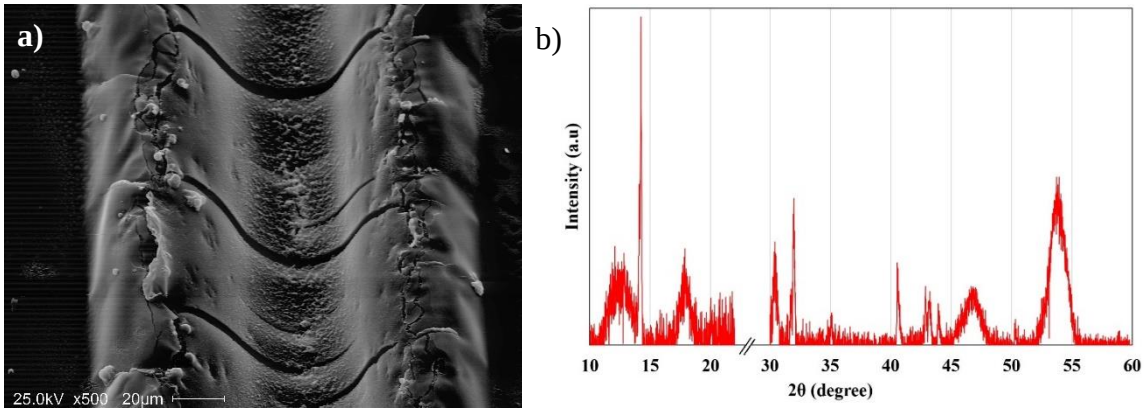

Figure 6.2 (a) The SEM image of the laser engraved microchannel (the image is taken at 44 degrees tilt angle), (b) the XRD spectra of the perovskite channel.

The transistor characteristics were measured in dark and under white light illumination (power density of 80 mW.cm^{-2}) which are represented in Figure 6.3. Since CYTOP surface hydrophobicity worsen at high electric field [170] and may cause degradation of the perovskite layer, the output characteristics (drain current (I_D) versus drain voltage (V_{DS})) were measured from 0 V to 20.0 V while varying gate voltage (V_{GS}) from 10.0 V to 30.0 V by 10.0 V steps. The transfer characteristic (I_D versus V_{GS}) of the fabricated device was measured at V_{DS} of 20 V.

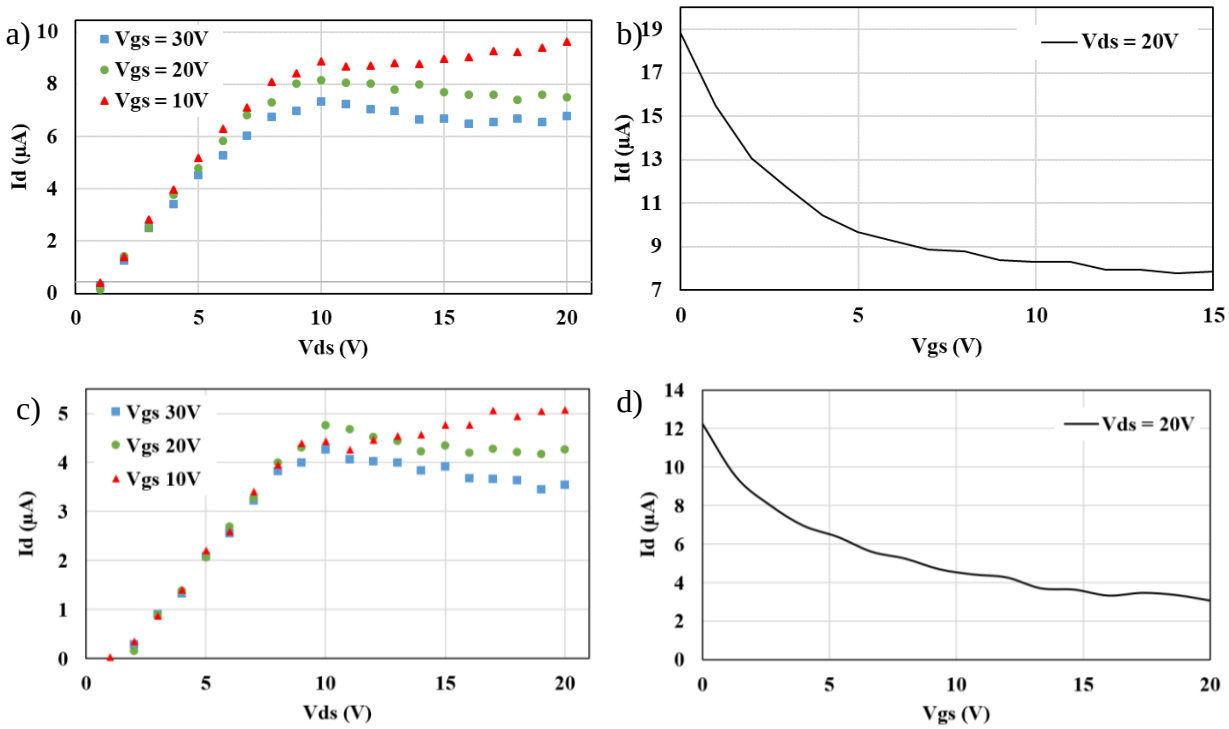

Figure 6.3 Transfer and output characteristics of the fabricated flexible transistor (a and b) under light illumination, (c and d) in dark.

As the channel was well encapsulated by CYTOP, all measurements were performed in ambient condition. To minimize ion-migration and bias stress effect the overall time duration of each scan was set to ~8 seconds and the time interval of few minutes was set between every two measurements while the sample was kept in the dark condition. In order to ensure that the decrease in current is not as the result of time, the output characteristics measurements were repeated in the

reverse order as well (starting at V_{GS} of 30 V and decreasing the V_{GS}) and the same trend was observed.

As can be seen from Figure 6.3, under light illumination condition, the current in both output and transfer characteristics is larger than the dark current at the equal bias voltages. From the output characteristics, the transistor reaches the saturation region when the drain-source voltage is above 10.0 V. As the gate voltage increased, the saturated drain current decreased. The same trend was observed from the transfer characteristics both in dark and light conditions. The drain current dropped when the gate voltage increased at a drain voltage of 20.0 V.

In this design, as the channel is very thick (~40 µm), light is not able to penetrate the whole channel. Therefore, the top gate does not modulate the gate effectively. Positive gate voltage makes a temporary inverted area near the gate contact. This area has a higher conductivity and the overall drain current is dominated by this area.

The crystallization of grains at low temperatures by solution-based fabrication process generates a large number of defects. These defects and trap states provide low activation energy and make a channel for intrinsic migration of I^-, MA^+, Pb^{2+}, and in some cases H^+ ions. These ions accumulate at the interfaces, screen the applied gate electric field, and they can reduce the mobile electrons concentration in the accumulation layer of FET [39]. Therefore ion migration plays an important role in carrier transport in lead halide perovskite [132]. The concentration of carriers changes mobility [171, 172]. As the saturation current is in direct relation with the mobility, decreasing the mobility lower the saturation current. The mobility of the fabricated device was calculated from the linear region of the transfer characteristic on using Equation 6-1 to be 1.7 $cm^2V^{-1}S^{-1}$.

$$\mu = \frac{I_{ds}}{C.V_{ds}} \frac{l}{w} (V_{th} - V_{gs}) \qquad (6.1)$$

where, C is the capacitor of CYTOP layer, l is the channel length, w is the channel width and V_{th} is the threshold voltage.

This novel fabrication method provides a simple solution to make $MAPbI_3$ transistor on flexible substrates with comparably high mobility. Under application of a positive gate voltage, the negative charged point defects drift toward the CYTOP/perovskite interface, screen the applied gate electric field. The transistor showed a p-type transport characteristic.

In the next section, a hybrid structure of zinc oxide (ZnO)/perovskite is studied. The perovskite thin film was deposited on the ZnO electron transport layer using a pneumatic nozzle printing method.

6.2 Fabrication of Perovskite Transistor Using Pneumatic Nozzle Printer

Printing techniques are among fast, simple and low-cost methods for the fabrication of flexible electronic devices and sensors [173]. Contact and non-contact approaches are usually used to develop a printing system. Contact printing methods such as dry transfer printing [174], offset printing [175] and nano-imprinting [176] place pre-patterned parts of a module in contact with the flexible (or non-flexible) substrates and transfer the ink onto them.

Non-contact printing techniques like inkjet printing [177], screen printing [178] and pneumatic nozzle printing [179] dispense the ink via openings or nozzles and define structures by moving the stage and/or nozzle.

Ink formula, substrate physical and chemical properties, printing speed, nozzle size and distance, solvent evaporation during the deposition and annealing conditions are among the factors that influence the printing quality [177, 180, 181]. Here, we employed a pneumatic nozzle printer to make a thin layer of $MAPbI_3$ and use this layer as the channel of a thin film transistor.

6.2.1 Ink Development

Ink properties such as viscosity, surface tension, and wetting behavior influence the crystallization and the quality of the perovskite film [181]. Thus, developing a proper ink is of utmost concern. Unlike some materials that solvents are mainly solubilizing agents and evaporation of the solvent after printing results in the desired layer, perovskite crystallite morphology relies heavily on the solvent [181].

Solvents may become incorporated into crystalline intermediate Phases. High coordinating solvents such as DMSO are beneficial to form homogeneous and pinhole-free thin films [181]. Also, while high boiling point solvents are favorable to stop early crystallization and clogging of the ink in the nozzle, a mixture of low and high boiling solvents can result in a homogeneous film formation [182]. Furthermore, the inhomogeneous mixture of solvents may adversely affect the reproducibility of the printed film with the same crystallization quality. For example, as ethanol ratio in the perovskite precursor can cause the formation of $MAPbI_3$ microcrystals [183], using the inhomogeneous ink containing 0.75 M equimolar PbI_2 and MAI, Acetic Acid, and ethanol, with the same printing parameters, resulted in the formation of perovskite microcrystals (Figure 6.4.a) and perovskite film with nano-size grains (Figure 6.4.b) due to different ethanol concentration.

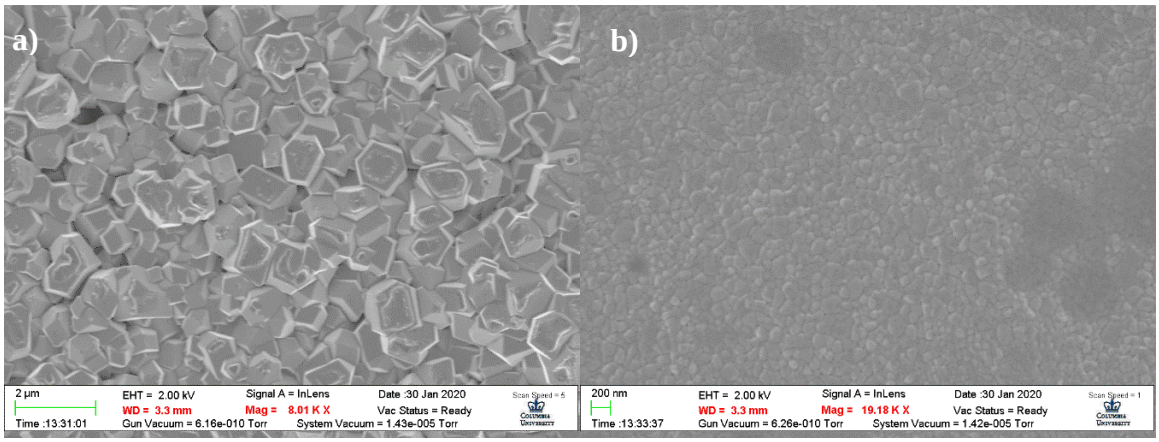

Figure 6.4 The top-view SEM image of $MAPbI_3$ printed on polyethylene naphthalate (PEN) showing inhomogeneous ink resulted in crystal size difference due to variation in ethanol concentration.

Molarity and hydrophobicity of the ink and substrate affect the film quality. Since PbI_2 is known as a highly polar salt and raise in its concentration results in higher hydrophobicity.

6.2.2 Device Fabrication

To make the transistor, a heavily doped 4-inch p-type <100> silicon wafer (0.005 Ω.cm) with 285 nm dry chlorinated thermally grown silicon dioxide layer was used as the substrate. Prior to fabrication, the substrate was placed under ultraviolet–ozone treatment for 10 min. Thereafter, an 80 nm ZnO layer was deposited on SiO_2 using RF-magnetron sputtering system.

To make the drain and source contacts, the wafer was covered with a shadow mask and a 5 nm layer chromium (adhesion layer) was thermally evaporated followed by 80 nm gold thermal evaporation. The gold and chromium evaporation rates were kept at 0.5 °$A.s^{-1}$ and 0.4 °$A.s^{-1}$ respectively during the process.

The perovskite precursor was prepared by mixing 1 M PbI_2 and 2 M MAI in a solution containing GBL and DMSO with a 1:3 ratio and it was kept at 60°C overnight. The precursor was then loaded into the syringe with a 25 gauge needle. During the printing, the substrate temperature was set to 85°C. The printing speed was kept at 0.1 $mm.s^{-1}$ and 0.7 and 0.7 psi of vacuum and forward pressure was applied, respectively. The width of the printed strip was ~470 µm. The transfer and output characteristics of the fabricated transistor were measured under ambient light. The schematic of the device is shown in Figure 6.5.

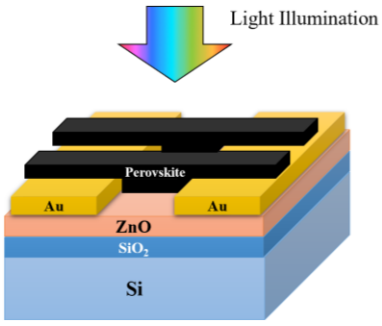

Figure 6.5 The schematic of the fabricated perovskite transistor by the pneumatic nozzle printing method.

6.2.3 Results and Discussion

Prior to the perovskite deposition, current-voltage characteristics of the gold contacts on the ZnO layer were measured and no current was observed by varying the gate voltage. Therefore, the ZnO layer is not performing as a transistor channel. As it can be seen in Figure 6.6, at the drain-source voltage of 10.0 V and the gate-source voltage of 0 V, nearly 0.46 µA current passed through the semiconductor, showing that the device was a normally ON transistor.

As the gate-source voltage was increased, the I_{ds} increased as well. However, the I_{ds}/V_{gs} slope reduces at higher voltages and the current remains constant at the gate-source voltages above 24.0 V suggesting that there is another mechanism hindering the transistor normal functionality.

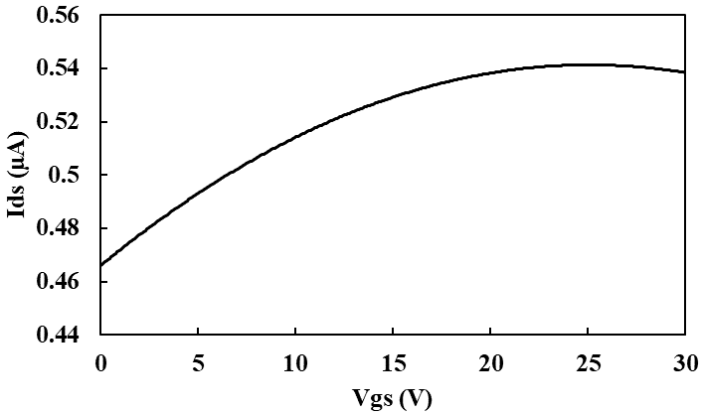

Figure 6.6 The transfer characteristic of the fabricated transistor at V_{ds} 10 V and under ambient light.

Figure 6.7 shows the output characteristics of the device. The drain-source current was measured at different constant gate-source voltages while increasing V_{ds}. To limit the electric field induced degradation of the perovskite layer, we discontinued the measurement for the drain-source voltages higher than 20.0 V. However, the last test was performed to show that the transistor reaches the saturation mode at higher voltages. The drain-source current was measured at the drain-source voltage of 40.0 V (Figure 6.7.b).

Although the transfer characteristics showed higher I_{ds} as V_{gs} gets higher, no meaningful relation between V_{gs} and I_{ds} was observed in the output characteristics which may imply an inevitable perovskite degradation while measurement was carried on under ambient condition when the device was not encapsulated.

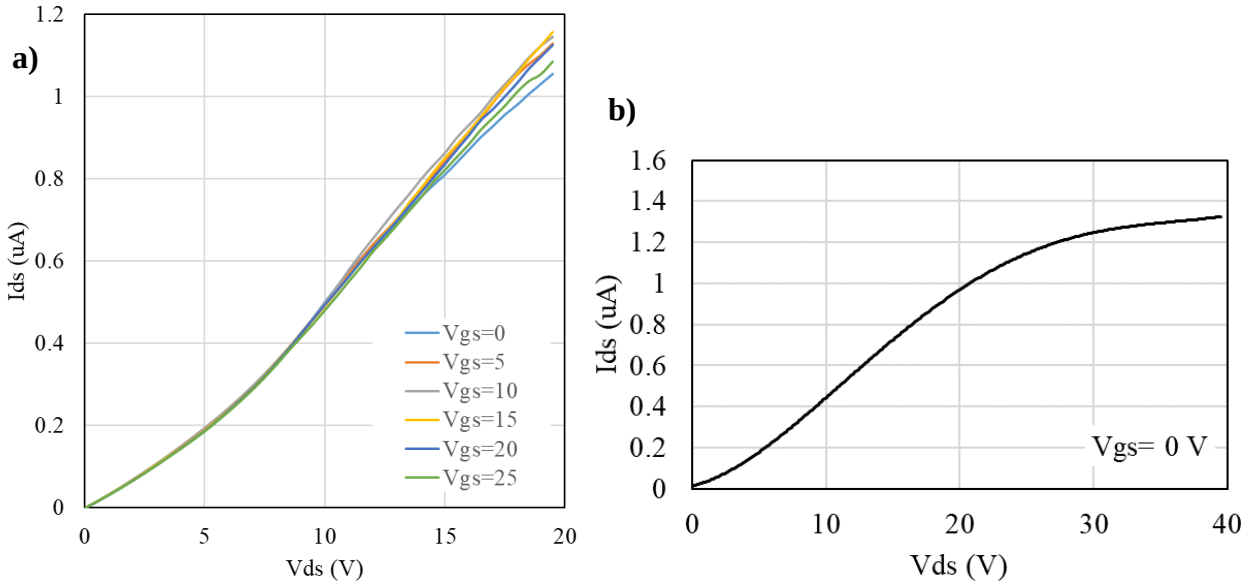

Figure 6.7 The output characteristics of the fabricated transistor.

Since ZnO layer was not conductive before the perovskite deposition, change in the carrier transport type observed in Figure 6.6 in compare with the Figure 6.3.b and d can be due to the significant role of defect at the surface of ZnO which is in contact with the perovskite layer. As time passed, degradation became the dominant mechanism and the current reduced (Figure 6.7). More studies are needed to better understand the mechanism.

6.3 Conclusion

In conclusion, in this chapter, we studied the feasibility of fabricating perovskite transistors by non-spin coating and non-lithography techniques. In the first design, by laser engraving, $MAPbI_3$ channel transistors were made.

In the second design, ZnO was placed between the gate oxide and the perovskite layer while having direct contact with the Au electrodes. This layer was aimed to drive excess carriers from the perovskite layer, to lower the concentration, and raise the mobility. Although the drain current increased by increasing V_{ds} and V_{gs}, as time passed the decomposition became the dominant process.

Both transistors operated in the ON state at zero gate-source voltage. Although cut off mode was not observed, at higher drain-source voltages, both transistors entered saturation mode. In addition, it was observed that encapsulation helps to suppress the perovskite decomposition rate by protecting it from moisture. However, degradation is an intrinsic process and can be electric field induced. Therefore, the perovskite transistor operation voltage has to be chosen at very low voltages. This study can facilitate a better understanding of charge carrier transport in $MAPbI_3$.

Chapter 7: Conclusion and Future Works

7.1 Conclusion

Since the first reported perovskite solar cell, this material has expanded its application in different photovoltaic devices. Owing to the extraordinary optical properties and the direct bandgap in the visible region, one of the interesting applications of $MAPbI_3$ can be an ambient light detector in a phototransistor configuration. Solution-based fabrication methods provide the capability to make perovskite devices and integrate them with capillary circuits for the label-free biosensing applications.

In this work, first, to ensure the feasibility of the idea, different methods were employed to make two-terminal photodetectors. The capillary channels were made by mechanical micromachining and laser engraving. Photolithography was found to be incapable of producing a cost-effective device since it requires many fabrication steps to make cast and mold and making high-quality contact with perovskite is complicated and difficult.

Mechanical micromachining was employed by using a custom-designed blade set up to engrave a wedge-shape capillary microchannel on an ITO coated PET substrate. An extremely small portion of the perovskite precursor filled the microchannel and made high-quality contact with ITO on both sides. The optical and electrical properties of the fabricated photodetector were characterized and compared with a photodetector with the same structure which was fabricated by lithography.

In a different approach, to enhance the reproducibility of the device, an industrial laser cutter was employed to engrave micro-channels on ITO coated PET substrates. This approach proved as a high-speed manufacturing method with the ability to produce devices in large scales.

Stability, ion-migration, and toxicity are the main challenges in $MAPbI_3$ based devices. The lead halide perovskite precursor can be prepared by mixing lead iodide and methylammonium iodide in a solution. All the proposed methods dramatically reduce the required amount of PbI_2 in comparison to the conventional spin coating technique. Also, the precursor waste percentage is zero in these methods. Therefore, only a very small amount of lead was used.

In another study, the stability of the fabricated photodetectors was examined by encapsulation technique using two different fluoropolymers (FluoroPel and CYTOP) and it was found that the photodetector's photocurrent encapsulated with either of the polymers, does not drop in a time period of 38 days and the encapsulation is highly effective. However, due to higher sustainability, CYTOP was chosen as the encapsulation material for the rest of the study. We also showed stress-induced ion migration can greatly enhance the photocurrent of the fabricated photodetectors.

Finally, perovskite phototransistor was made by using the top contact gate configuration and laser engraving method which was used to make the two-terminal photodetector. The perovskite layer was fully covered, and the gate contact did not require any photolithography steps and glove box condition. This design is extremely low-cost, reproducible, and simple.

7.2 Future Works

There are mainly 4 challenges we face in lead halide perovskite phototransistors which are: lead toxicity, instability, defects and current modulation. The proposed method effectively reduces

the amount of lead in a way that makes it far below the dangerous level defined by the U.S. standard and regulations for lead toxicity level, therefore the device can be counted as non-toxic [184].

Regarding stability, defects and current modulation more studies are needed to address many still open questions, such as (1) what is the effect of encapsulation of perovskite on the crystalline structure, phase and grains? (2) how does capillary motion affect element distribution in a microchannel? And does the stoichiometry vary across the channel? (3) does surface tension affect the crystal orientation during solidification of the precursor inside microchannels?

For future works, it is suggested more characterization techniques to be performed such as piezo-force microscopy (PFM) to determine the piezoelectric coefficients. A higher resolution laser cutter can be employed to narrow the channel length of the transistor and increase the width-to-length ratio. The crystal growth of the perovskite in curved or zig-zag shaped microfluidic channels is also feasible and encouraged to be studied. In addition, to fully understand ion migration impact to perovskite phototransistor performance, I-V characteristics can be measured at low to moderate temperatures to suppress the migration of ions or accelerate them and observe the related effect. Since a high electric field induces material to degrade, the upper limit voltage which indicates as a typical operation voltage of the device needs to be found.

It was shown that perovskite transistor fabrication by pneumatic nozzle printer is possible. This method is simple, fast and cost-effective with the feasibility of large-scale fabrication and capability to make nonplanar structures. It has the potential to be one of the highest demanded industrial products.

One of the main advantages of printing techniques is having the degree of freedom to manipulate many parameters and optimize crystallization. Developing the proper ink would help

to print a defect-free homogeneous film and optimize the ink printing behavior to make it independent of the substrate physical properties.

References

[1] Pires, N., et al., Integrated optical microfluidic biosensor using a polycarbazole photodetector for point-of-care detection of hormonal compounds. Journal of biomedical optics, 2013. 18(9): p. 097001.

[2] Sodnik, Z., B. Furch, and H. Lutz, Optical intersatellite communication. IEEE journal of selected topics in quantum electronics, 2010. 16(5): p. 1051-1057.

[3] Ahmadi, M., T. Wu, and B. Hu, A review on organic–inorganic halide perovskite photodetectors: device engineering and fundamental physics. Advanced Materials, 2017. 29(41): p. 1605242.

[4] Yotter, R.A. and D.M. Wilson, A review of photodetectors for sensing light-emitting reporters in biological systems. IEEE Sensors Journal, 2003. 3(3): p. 288-303.

[5] Fossum, E.R. and D.B. Hondongwa, A review of the pinned photodiode for CCD and CMOS image sensors. IEEE Journal of the electron devices society, 2014.

[6] Brennan, D., et al., Emerging optofluidic technologies for point-of-care genetic analysis systems: a review. Analytical and bioanalytical chemistry, 2009. 395(3): p. 621-636.

[7] Fan, X. and I.M. White, Optofluidic microsystems for chemical and biological analysis. Nature photonics, 2011. 5(10): p. 591.

[8] Zhu, J., et al., Optofluidic marine phosphate detection with enhanced absorption using a Fabry–Pérot resonator. Lab on a Chip, 2017. 17(23): p. 4025-4030.

[9] Yang, Y., et al., Optofluidic waveguide as a transformation optics device for lightwave bending and manipulation. Nature communications, 2012. 3(1): p. 1-7.

[10] Li, Z., et al., Single mode optofluidic distributed feedback dye laser. Optics Express, 2006. 14(2): p. 696-701.

[11] Han, D., et al., Pulse Oximetry Using Organic Optoelectronics under Ambient Light. Advanced Materials Technologies, 2020: p. 1901122.

[12] Park, Y.M., et al., Ambient light-based optical biosensing platform with smartphone-embedded illumination sensor. Biosensors and Bioelectronics, 2017. 93: p. 205-211.

[13] Stranks, S.D. and H.J. Snaith, Metal-halide perovskites for photovoltaic and light-emitting devices. Nature nanotechnology, 2015. 10(5): p. 391.

[14] Moon, S., et al., Integrating microfluidics and lensless imaging for point-of-care testing. Biosensors and Bioelectronics, 2009. 24(11): p. 3208-3214.

[15] Chiriaco, M.S., et al., EIS microfluidic chips for flow immunoassay and ultrasensitive cholera toxin detection. Lab on a Chip, 2011. 11(4): p. 658-663.

[16] Kim, J.-H., et al., Immunosensor towards low-cost, rapid diagnosis of tuberculosis. Lab on a Chip, 2012. 12(8): p. 1437-1440.

[17] de Arquer, F.P.G., et al., Solution-processed semiconductors for next-generation photodetectors. Nature Reviews Materials, 2017. 2(3): p. 1-17.

[18] Raghu Das, X.H.a.K.G., Printed, Organic and Flexible Electronics 2020-2030: Forecasts, Technologies, Markets. IDTechEx Research

[19] Xie, C., et al., Perovskite-Based Phototransistors and Hybrid Photodetectors. Advanced Functional Materials, 2019: p. 1903907.

[20] Ward, J.W., et al., Solution-processed organic and halide perovskite transistors on hydrophobic surfaces. ACS applied materials & interfaces, 2017. 9(21): p. 18120-18126.

[21] Li, F., et al., Ambipolar solution-processed hybrid perovskite phototransistors. Nature communications, 2015. 6: p. 8238.

[22] Chin, X.Y., et al., Lead iodide perovskite light-emitting field-effect transistor. Nature communications, 2015. 6: p. 7383.

[23] Liu, J., et al., Two-dimensional CH3NH3PbI3 perovskite: Synthesis and optoelectronic application. ACS nano, 2016. 10(3): p. 3536-3542.

[24] Wu, Y., et al., Organic–inorganic hybrid CH 3 NH 3 PbI 3 perovskite materials as channels in thin-film field-effect transistors. RSC advances, 2016. 6(20): p. 16243-16249.

[25] Kim, Y. and B. Park, Interfacial charge transport in MAPbI3 perovskite on ZnO. Results in Physics, 2019. 13: p. 102207.

[26] Cho, N., et al., Pure crystal orientation and anisotropic charge transport in large-area hybrid perovskite films. Nature communications, 2016. 7(1): p. 1-11.

[27] Li, D., et al., The effect of thermal annealing on charge transport in organolead halide perovskite microplate field-effect transistors. Advanced Materials, 2017. 29(4): p. 1601959.

[28] Mei, Y., et al., Electrostatic gating of hybrid halide perovskite field-effect transistors: balanced ambipolar transport at room-temperature. MRS Communications, 2015. 5(2): p. 297-301.

[29] Yu, H., et al., Vertical Organic–Inorganic Hybrid Perovskite Schottky Junction Transistors. Advanced Electronic Materials, 2018. 4(5): p. 1800039.

[30] Canicoba, N.D., et al., Halide Perovskite High-k Field Effect Transistors with Dynamically Reconfigurable Ambipolarity. ACS Materials Letters, 2019. 1(6): p. 633-640.

[31] Lü, Q.-R., et al., CH3NH3PbI3 Single Crystal-Based Ambipolar Field-Effect Transistor with Ta2O5 as the Top Gate Dielectric. Acta Physico-Chimica Sinica, 2017. 33(1): p. 249-254.

[32] Ji, J., et al., Ambipolar Transport in Methylammonium Lead Iodide Thin Film Transistors. Crystals, 2019. 9(10): p. 539.

[33] Wang, Y., et al., Hybrid graphene–perovskite phototransistors with ultrahigh responsivity and gain. Advanced Optical Materials, 2015. 3(10): p. 1389-1396.

[34] Wang, G., et al., Wafer-scale growth of large arrays of perovskite microplate crystals for functional electronics and optoelectronics. Science advances, 2015. 1(9): p. e1500613.

[35] Wang, J., et al., Novel organic-perovskite hybrid structure forward photo field effect transistor. Organic Electronics, 2016. 38: p. 158-163.

[36] Tong, S., et al., Large-area and high-performance CH3NH3PbI3 perovskite photodetectors fabricated via doctor blading in ambient condition. Organic Electronics, 2017. 49: p. 347-354.

[37] Li, F., et al., Ultrahigh Carrier Mobility Achieved in Photoresponsive Hybrid Perovskite Films via Coupling with Single-Walled Carbon Nanotubes. Advanced Materials, 2017. 29(16): p. 1602432.

[38] He, B., et al., Ultrasensitive all-solution-processed field-effect transistor based perovskite photodetectors with sol-gel SiO2 as the dielectric layer. Journal of Alloys and Compounds, 2017. 717: p. 150-155.

[39] Senanayak, S.P., et al., Understanding charge transport in lead iodide perovskite thin-film field-effect transistors. Science advances, 2017. 3(1): p. e1601935.

[40] Lv, Q., et al., Anisotropic Carrier Transport in CH 3 NH 3 PbI 3 Single Crystal Field-Effect Transistor. IEEE Electron Device Letters, 2018. 39(9): p. 1389-1392.

[41] Cao, M., et al., Enhanced perovskite phototransistor by multi-step slow annealing strategy. Optical Materials, 2018. 84: p. 498-503.

[42] Hong, Z., et al., Controllable switching properties in an individual CH 3 NH 3 PbI 3 micro/nanowire-based transistor for gate voltage and illumination dual-driving non-volatile memory. Journal of Materials Chemistry C, 2019. 7(14): p. 4259-4266.

[43] Hoang, N.T.T., et al., Fast-switching mixed a-cation organic-inorganic hybrid perovskite TFTs. IEEE Electron Device Letters, 2019. 40(6): p. 917-920.

[44] Zhou, Z., et al., The Effect of Annealing Pressure on Perovskite Films and Its Thin-Film Field-Effect Transistors' Performance. physica status solidi (a), 2019. 216(22): p. 1900434.

[45] Chen, P.-A., et al., Microfluidic Solution-Processed Organic and Perovskite Nanowires Fabricated for Field-Effect Transistors and Photodetectors. Journal of Materials Chemistry C, 2020.

[46] Tilley, R.J., Perovskites: structure-property relationships. 2016: John Wiley & Sons.

[47] Bowman, H., On the structure of perovskite from the Burgumer alp, Pfitschthal, tyrol. Mineralogical Magazine and Journal of the Mineralogical Society, 1908. 15(69): p. 156-176.

[48] Glazer, A., The classification of tilted octahedra in perovskites. Acta Crystallographica Section B: Structural Crystallography and Crystal Chemistry, 1972. 28(11): p. 3384-3392.

[49] Frost, J.M., et al., Atomistic origins of high-performance in hybrid halide perovskite solar cells. Nano letters, 2014. 14(5): p. 2584-2590.

[50] Sommer, R., N. Yushin, and J. Van der Klink, Polar metastability and an electric-field-induced phase transition in the disordered perovskite Pb (Mg 1/3 Nb 2/3) O 3. Physical Review B, 1993. 48(18): p. 13230.

[51] Ullah, A., et al., Electric-field-induced phase transition and large strain in lead-free Nb-doped BNKT-BST ceramics. Journal of the European Ceramic Society, 2014. 34(1): p. 29-35.

[52] Wang, K., et al., Pressure-induced reversible phase transition and amorphization of CH3NH3PbI3. arXiv preprint arXiv:1509.03717, 2015.

[53] Lee, Y., et al., Pressure-induced phase transitions and templating effect in three-dimensional organic-inorganic hybrid perovskites. Physical Review B, 2003. 68(2): p. 020103.

[54] Fu, W., et al., Temperature-induced phase transitions in BaTbO3. Journal of Solid State Chemistry, 2004. 177(4-5): p. 1667-1671.

[55] Jacobsson, T.J., et al., Determination of thermal expansion coefficients and locating the temperature-induced phase transition in methylammonium lead perovskites using x-ray diffraction. Inorganic chemistry, 2015. 54(22): p. 10678-10685.

[56] Azpiroz, J.M., et al., Defect migration in methylammonium lead iodide and its role in perovskite solar cell operation. Energy & Environmental Science, 2015. 8(7): p. 2118-2127.

[57] Lee, J.-W., et al., 2D perovskite stabilized phase-pure formamidinium perovskite solar cells. Nature communications, 2018. 9(1): p. 1-10.

[58] Camargo, F.V., et al., Dark sub-gap states in metal-halide perovskites revealed by coherent multidimensional spectroscopy. Journal of the American Chemical Society, 2019.

[59] De Marco, N., et al., Guanidinium: a route to enhanced carrier lifetime and open-circuit voltage in hybrid perovskite solar cells. Nano letters, 2016. 16(2): p. 1009-1016.

[60] Saliba, M., et al., Cesium-containing triple cation perovskite solar cells: improved stability, reproducibility and high efficiency. Energy & environmental science, 2016. 9(6): p. 1989-1997.

[61] Koh, T.M., et al., Formamidinium tin-based perovskite with low E g for photovoltaic applications. Journal of Materials Chemistry A, 2015. 3(29): p. 14996-15000.

[62] Amat, A., et al., Cation-induced band-gap tuning in organohalide perovskites: interplay of spin–orbit coupling and octahedra tilting. Nano letters, 2014. 14(6): p. 3608-3616.

[63] Li, S., et al., Metal halide perovskite single crystals: from growth process to application. Crystals, 2018. 8(5): p. 220.

[64] Hoefler, S.F., G. Trimmel, and T. Rath, Progress on lead-free metal halide perovskites for photovoltaic applications: a review. Monatshefte für Chemie-Chemical Monthly, 2017. 148(5): p. 795-826.

[65] Kim, Y.-H., H. Cho, and T.-W. Lee, Metal halide perovskite light emitters. Proceedings of the National Academy of Sciences, 2016. 113(42): p. 11694-11702.

[66] Lin, Y.H., P. Pattanasattayavong, and T.D. Anthopoulos, Metal-Halide Perovskite Transistors for Printed Electronics: Challenges and Opportunities. Advanced Materials, 2017. 29(46): p. 1702838.

[67] Dong, Y., et al., Recent progress of metal halide perovskite photodetectors. Journal of Materials Chemistry C, 2017. 5(44): p. 11369-11394.

[68] He, X., et al., Patterning multicolored microdisk laser arrays of cesium lead halide perovskite. Advanced Materials, 2017. 29(12): p. 1604510.

[69] Fu, Q., et al., Recent Progress on the Long-Term Stability of Perovskite Solar Cells. Advanced Science, 2018. 5(5): p. 1700387.

[70] Li, Y., et al., Over 20% Efficiency in Methylammonium Lead Iodide Perovskite Solar Cells with Enhanced Stability via “in Situ Solidification” of the TiO2 Compact Layer. ACS Applied Materials & Interfaces, 2020. 12(6): p. 7135-7143.

[71] Alsalloum, A.Y., et al., Low-Temperature Crystallization Enables 21.9% Efficient Single-Crystal MAPbI3 Inverted Perovskite Solar Cells. ACS Energy Letters, 2020. 5(2): p. 657-662.

[72] Stoumpos, C.C., C.D. Malliakas, and M.G. Kanatzidis, Semiconducting tin and lead iodide perovskites with organic cations: phase transitions, high mobilities, and near-infrared photoluminescent properties. Inorganic chemistry, 2013. 52(15): p. 9019-9038.

[73] Papavassiliou, G.C., G.A. Mousdis, and I. Koutselas, Some new organic–inorganic hybrid semiconductors based on metal halide units: structural, optical and related properties. Advanced Materials for Optics and Electronics, 1999. 9(6): p. 265-271.

[74] Kojima, A., et al., Organometal halide perovskites as visible-light sensitizers for photovoltaic cells. Journal of the American Chemical Society, 2009. 131(17): p. 6050-6051.

[75] Foley, B.J., et al., Temperature dependent energy levels of methylammonium lead iodide perovskite. Applied Physics Letters, 2015. 106(24): p. 243904.

[76] Hoque, M.N.F., et al., Ionic and optical properties of methylammonium lead iodide perovskite across the tetragonal–cubic structural phase transition. ChemSusChem, 2016. 9(18): p. 2692-2698.

[77] Diroll, B.T., P. Guo, and R.D. Schaller, Unique optical properties of methylammonium lead iodide nanocrystals below the bulk tetragonal-orthorhombic phase transition. Nano letters, 2018. 18(2): p. 846-852.

[78] Quarti, C., et al., Structural and optical properties of methylammonium lead iodide across the tetragonal to cubic phase transition: implications for perovskite solar cells. Energy & Environmental Science, 2016. 9(1): p. 155-163.

[79] Xing, G., et al., Long-range balanced electron-and hole-transport lengths in organic-inorganic CH3NH3PbI3. Science, 2013. 342(6156): p. 344-347.

[80] Dong, Q., et al., Electron-hole diffusion lengths> 175 μm in solution-grown CH3NH3PbI3 single crystals. Science, 2015. 347(6225): p. 967-970.

[81] Wang, Q., et al., Qualifying composition dependent p and n self-doping in CH3NH3PbI3. Applied Physics Letters, 2014. 105(16): p. 163508.

[82] Zhang, C.C., et al., Polarized Ferroelectric Polymers for High-Performance Perovskite Solar Cells. Advanced Materials, 2019. 31(30): p. 1902222.

[83] Frolova, L.A., N.N. Dremova, and P.A. Troshin, The chemical origin of the p-type and n-type doping effects in the hybrid methylammonium–lead iodide (MAPbI 3) perovskite solar cells. Chemical Communications, 2015. 51(80): p. 14917-14920.

[84] Levine, I., et al., Mobility–Lifetime Products in MAPbI3 Films. The journal of physical chemistry letters, 2016. 7(24): p. 5219-5226.

[85] Chen, Y., et al., Extended carrier lifetimes and diffusion in hybrid perovskites revealed by Hall effect and photoconductivity measurements. Nature communications, 2016. 7(1): p. 1-9.

[86] Boix, P.P., et al., Perovskite solar cells: beyond methylammonium lead iodide. The journal of physical chemistry letters, 2015. 6(5): p. 898-907.

[87] Rakita, Y., et al., Tetragonal CH3NH3PbI3 is ferroelectric. Proceedings of the National Academy of Sciences, 2017. 114(28): p. E5504-E5512.

[88] Sun, Y. and X. Yan, Recent advances in dual-functional devices integrating solar cells and supercapacitors. Solar RRL, 2017. 1(3-4): p. 1700002.

[89] Kim, Y.-J., et al., Piezoelectric properties of CH 3 NH 3 PbI 3 perovskite thin films and their applications in piezoelectric generators. Journal of Materials Chemistry A, 2016. 4(3): p. 756-763.

[90] Coll, M., et al., Polarization switching and light-enhanced piezoelectricity in lead halide perovskites. The journal of physical chemistry letters, 2015. 6(8): p. 1408-1413.

[91] Lai, Q., et al., Piezo-Phototronic Effect Enhanced Photodetector Based on CH3NH3PbI3 Single Crystal. ACS Nano, 2018.

[92] Dong, Q., et al., Lateral-Structure Single-Crystal Hybrid Perovskite Solar Cells via Piezoelectric Poling. Advanced Materials, 2016. 28(14): p. 2816-2821.

[93] Cai, B., W.-H. Zhang, and J. Qiu, Solvent engineering of spin-coating solutions for planar-structured high-efficiency perovskite solar cells. Chinese Journal of Catalysis, 2015. 36(8): p. 1183-1190.

[94] Zhang, Z., et al., High reproducibility of perovskite solar cells via a complete spin-coating sequential solution deposition process. Solar Energy, 2015. 122: p. 97-103.

[95] Park, Y. and B. Park, Interfacial energy band bending and carrier trapping at the vacuum-deposited MAPbI3 perovskite/gate dielectric interface. Results in Physics, 2018. 11: p. 302-305.

[96] Li, M.H., et al., Highly Efficient 2D/3D Hybrid Perovskite Solar Cells via Low-Pressure Vapor-Assisted Solution Process. Advanced Materials, 2018. 30(30): p. 1801401.

[97] Bonomi, S., et al., Novel physical vapor deposition approach to hybrid perovskites: Growth of MAPbI 3 thin films by RF-magnetron sputtering. Scientific reports, 2018. 8(1): p. 1-8.

[98] Peng, Y., et al., Fully doctor-bladed planar heterojunction perovskite solar cells under ambient condition. Organic Electronics, 2018. 58: p. 153-158.

[99] Rocks, C., et al., Understanding surface chemistry during MAPbI 3 spray deposition and its effect on photovoltaic performance. Journal of Materials Chemistry C, 2017. 5(4): p. 902-916.

[100] Liang, C., et al., One-step inkjet printed perovskite in air for efficient light harvesting. Solar RRL, 2018. 2(2): p. 1700217.

[101] Li, Z., et al., Scalable fabrication of perovskite solar cells. Nature Reviews Materials, 2018. 3(4): p. 18017.

[102] Khorramshahi, F. and A. Takshi. Novel fabrication of flexible perovskite photosensor using capillary motion. in Organic and Hybrid Sensors and Bioelectronics XI. 2018. International Society for Optics and Photonics.

[103] Gu, L., et al., 3D Arrays of 1024-Pixel Image Sensors based on Lead Halide Perovskite Nanowires. Advanced Materials, 2016. 28(44): p. 9713-9721.

[104] Khorramshahi, F., et al. Laser assisted rapid fabrication of perovskite photodetector. in Organic and Hybrid Sensors and Bioelectronics XII. 2019. International Society for Optics and Photonics.

[105] Olanrewaju, A., et al., Capillary microfluidics in microchannels: from microfluidic networks to capillaric circuits. Lab on a Chip, 2018. 18(16): p. 2323-2347.

[106] Terry, S.C., J.H. Jerman, and J.B. Angell, A gas chromatographic air analyzer fabricated on a silicon wafer. IEEE transactions on electron devices, 1979. 26(12): p. 1880-1886.

[107] Qi, H., et al., Fabrication and characterization of a polymethyl methacrylate continuous-flow PCR microfluidic chip using CO 2 laser ablation. Microsystem technologies, 2009. 15(7): p. 1027-1030.

[108] Lim, D., et al., Fabrication of microfluidic mixers and artificial vasculatures using a high-brightness diode-pumped Nd: YAG laser direct write method. Lab on a Chip, 2003. 3(4): p. 318-323.

[109] McGinty, S., G.M. O'Connor, and T.J. Glynn. A comparative study of channel formation in polymer materials using VUV and UV nano-second laser sources for use in micro-fluidic applications. in Opto-Ireland 2005: Optoelectronics, Photonic Devices, and Optical Networks. 2005. International Society for Optics and Photonics.

[110] Bhattacharjya, D., et al., Fast and controllable reduction of graphene oxide by low-cost CO2 laser for supercapacitor application. Applied Surface Science, 2018. 462: p. 353-361.

[111] Chen, T.-C. and R.B. Darling, Laser micromachining of the materials using in microfluidics by high precision pulsed near and mid-ultraviolet Nd: YAG lasers. Journal of materials processing technology, 2008. 198(1-3): p. 248-253.

[112] Shaegh, S.A.M., et al., Rapid prototyping of whole-thermoplastic microfluidics with built-in microvalves using laser ablation and thermal fusion bonding. Sensors and Actuators B: Chemical, 2018. 255: p. 100-109.

[113] Ghandoori, T., et al., Fabrication of polycarbonate microfluidic devices using a focusing and defocusing methods of CO2 laser system. Advanced science, engineering and medicine, 2014. 6(1): p. 50-55.

[114] Yan, S., et al., A rapid, maskless 3D prototyping for fabrication of capillary circuits: Toward urinary protein detection. Electrophoresis, 2018. 39(7): p. 957-964.

[115] Green, M.A., et al., Solar cell efficiency tables (Version 55). Progress in Photovoltaics: Research and Applications, 2020. 28(1): p. 3-15.

[116] Mahapatra, A., et al., A review of aspects of additive engineering in perovskite solar cells. Journal of Materials Chemistry A, 2020. 8(1): p. 27-54.

[117] Niu, G., et al., Study on the stability of CH 3 NH 3 PbI 3 films and the effect of post-modification by aluminum oxide in all-solid-state hybrid solar cells. Journal of Materials Chemistry A, 2014. 2(3): p. 705-710.

[118] Wong-Stringer, M., et al., High-Performance Multilayer Encapsulation for Perovskite Photovoltaics. Advanced Energy Materials, 2018. 8(24): p. 1801234.

[119] Bella, F., et al., Improving efficiency and stability of perovskite solar cells with photocurable fluoropolymers. Science, 2016. 354(6309): p. 203-206.

[120] Zong, Y., et al., Continuous grain-boundary functionalization for high-efficiency perovskite solar cells with exceptional stability. Chem, 2018. 4(6): p. 1404-1415.

[121] Kim, G.-H., et al., Fluorine functionalized graphene nano platelets for highly stable inverted perovskite solar cells. Nano letters, 2017. 17(10): p. 6385-6390.

[122] Guo, Y., et al., Air-stable and solution-processable perovskite photodetectors for solar-blind UV and visible light. The journal of physical chemistry letters, 2015. 6(3): p. 535-539.

[123] Khorramshahi, F., et al., Apparent Piezo-Photocurrent Modulation in Methylammonium Lead Iodide Perovskite Photodetectors. Advanced Electronic Materials, 2019. 5(12): p. 1900518.

[124] Lee, E.R., Microdrop generation. 2018: CRC press.

[125] Koo, B. and C.-J. Kim, Evaluation of repeated electrowetting on three different fluoropolymer top coatings. Journal of Micromechanics and Microengineering, 2013. 23(6): p. 067002.

[126] Yuan, Y., et al., Electric-field-driven reversible conversion between Methylammonium lead triiodide perovskites and lead iodide at elevated temperatures. Advanced Energy Materials, 2016. 6(2): p. 1501803.

[127] Kim, H.-S. and N.-G. Park, Parameters affecting I–V hysteresis of CH3NH3PbI3 perovskite solar cells: effects of perovskite crystal size and mesoporous TiO2 layer. The journal of physical chemistry letters, 2014. 5(17): p. 2927-2934.

[128] Kim, H.-S., et al., Control of I–V hysteresis in CH3NH3PbI3 perovskite solar cell. The journal of physical chemistry letters, 2015. 6(22): p. 4633-4639.

[129] Sanchez, R.S., et al., Slow dynamic processes in lead halide perovskite solar cells. Characteristic times and hysteresis. The journal of physical chemistry letters, 2014. 5(13): p. 2357-2363.

[130] Chen, B., et al., Impact of capacitive effect and ion migration on the hysteretic behavior of perovskite solar cells. The journal of physical chemistry letters, 2015. 6(23): p. 4693-4700.

[131] Futscher, M.H., et al., Quantification of Ion Migration in CH3NH3PbI3 Perovskite Solar Cells by Transient Capacitance Measurements. arXiv preprint arXiv:1801.08519, 2018.

[132] Yuan, Y. and J. Huang, Ion migration in organometal trihalide perovskite and its impact on photovoltaic efficiency and stability. Accounts of chemical research, 2016. 49(2): p. 286-293.

[133] Levine, I., et al., Interface-dependent ion migration/accumulation controls hysteresis in MAPbI3 solar cells. The Journal of Physical Chemistry C, 2016. 120(30): p. 16399-16411.

[134] Sutherland, B.R., et al., Sensitive, fast, and stable perovskite photodetectors exploiting interface engineering. Acs Photonics, 2015. 2(8): p. 1117-1123.

[135] Lian, Z., et al., High-performance planar-type photodetector on (100) facet of MAPbI 3 single crystal. Scientific reports, 2015. 5: p. 16563.

[136] Chen, S., et al., A Flexible UV–Vis–NIR Photodetector based on a Perovskite/Conjugated-Polymer Composite. Advanced Materials, 2016. 28(28): p. 5969-5974.

[137] Li, P., et al., High performance photodetector based on 2D CH3NH3PbI3 perovskite nanosheets. Journal of Physics D: Applied Physics, 2017. 50(9): p. 094002.

[138] Lin, Q., et al., Near infrared photodetectors based on sub-gap absorption in organohalide perovskite single crystals. Laser & Photonics Reviews, 2016. 10(6): p. 1047-1053.

[139] Liang, S., et al., ZnO Schottky ultraviolet photodetectors. Journal of crystal Growth, 2001. 225(2-4): p. 110-113.

[140] Konstantatos, G., et al., Ultrasensitive solution-cast quantum dot photodetectors. Nature, 2006. 442(7099): p. 180.

[141] Xin Hu, X.Z., Lin Liang, Jian Bao, Shuang Li, Wenlong Yang, Yi Xie, High-Performance Flexible Broadband Photodetector Based on Organolead Halide Perovskite. Advanced materials, 2014. 24(46): p. 8.

[142] Khorramshahi, F., O.E. Okeke, and A. Takshi, Electrochemical photocurrent enhancement in a ZnO-perovskite heterojunction using piezoelectric effect. Electrochimica Acta, 2018. 266: p. 110-117.

[143] Song, Z., et al., Impact of processing temperature and composition on the formation of methylammonium lead iodide perovskites. Chemistry of Materials, 2015. 27(13): p. 4612-4619.

[144] Ha, T.-J., et al., Transformation of the electrical characteristics of graphene field-effect transistors with fluoropolymer. ACS applied materials & interfaces, 2012. 5(1): p. 16-20.

[145] Uchino, K., Ferroelectric devices. 2018: CRC press.

[146] Miao, J. and F. Zhang, Recent progress on highly sensitive perovskite photodetectors. Journal of Materials Chemistry C, 2019. 7(7): p. 1741-1791.

[147] Deng, Y., Z. Xiao, and J. Huang, Light-induced self-poling effect on organometal trihalide perovskite solar cells for increased device efficiency and stability. Advanced Energy Materials, 2015. 5(20): p. 1500721.

[148] Yuan, Y., et al., Photovoltaic switching mechanism in lateral structure hybrid perovskite solar cells. Advanced Energy Materials, 2015. 5(15): p. 1500615.

[149] Gottesman, R., et al., Dynamic phenomena at perovskite/electron-selective contact interface as interpreted from photovoltage decays. Chem, 2016. 1(5): p. 776-789.

[150] Zheng, Y., et al., A cytop insulating tunneling layer for efficient perovskite solar cells. Small Methods, 2017. 1(10): p. 1700244.

[151] Deegan, R.D., et al., Capillary flow as the cause of ring stains from dried liquid drops. Nature, 1997. 389(6653): p. 827.

[152] Oku, T., Crystal structures of CH3NH3PbI3 and related perovskite compounds used for solar cells, in Solar Cells-New Approaches and Reviews. 2015, InTech.

[153] Saidaminov, M.I., et al., Planar-integrated single-crystalline perovskite photodetectors. Nature communications, 2015. 6: p. 8724.

[154] Kwon, K.C., et al., Inhibition of Ion Migration for Reliable Operation of Organolead Halide Perovskite-Based Metal/Semiconductor/Metal Broadband Photodetectors. Advanced Functional Materials, 2016. 26(23): p. 4213-4222.

[155] Stassi, S., et al., Flexible tactile sensing based on piezoresistive composites: A review. Sensors, 2014. 14(3): p. 5296-5332.

[156] Tong, S., et al., High-Performance Broadband Perovskite Photodetectors Based on CH3NH3PbI3/C8BTBT Heterojunction. Advanced Electronic Materials, 2017. 3(7): p. 1700058.

[157] Flores-Livas, J.A., et al., Emergence of hidden phases of methylammonium lead iodide (CH 3 NH 3 PbI 3) upon compression. Physical Review Materials, 2018. 2(8): p. 085201.

[158] Bonomi, S., et al., Ambient condition retention of band-gap tuning in MAPbI 3 induced by high pressure quenching. Chemical Communications, 2018. 54(94): p. 13212-13215.

[159] Francisco-López, A.n., et al., Pressure-Induced Locking of Methylammonium Cations versus Amorphization in Hybrid Lead Iodide Perovskites. The Journal of Physical Chemistry C, 2018. 122(38): p. 22073-22082.

[160] Ou, T., et al., Visible light response, electrical transport, and amorphization in compressed organolead iodine perovskites. Nanoscale, 2016. 8(22): p. 11426-11431.

[161] Jaffe, A., et al., High-pressure single-crystal structures of 3D lead-halide hybrid perovskites and pressure effects on their electronic and optical properties. ACS central science, 2016. 2(4): p. 201-209.

[162] Postorino, P. and L. Malavasi, Pressure-induced effects in organic–inorganic hybrid perovskites. The journal of physical chemistry letters, 2017. 8(12): p. 2613-2622.

[163] Shi, J., et al., Interfaces in perovskite solar cells. Small, 2015. 11(21): p. 2472-2486.

[164] Mosconi, E., et al., Light-induced annihilation of Frenkel defects in organo-lead halide perovskites. Energy & Environmental Science, 2016. 9(10): p. 3180-3187.

[165] Smecca, E., et al., Stability of solution-processed MAPbI 3 and FAPbI 3 layers. Physical Chemistry Chemical Physics, 2016. 18(19): p. 13413-13422.

[166] Bae, S., et al., Electric-field-induced degradation of methylammonium lead iodide perovskite solar cells. The journal of physical chemistry letters, 2016. 7(16): p. 3091-3096.

[167] Zhu, H., et al., Printable semiconductors for backplane TFTs of flexible OLED displays. Advanced Functional Materials, 2019.

[168] Sundholm, E.S., Amorphous oxide semiconductor thin-film transistor ring oscillators and material assessment. 2010.

[169] Petti, L., et al., Metal oxide semiconductor thin-film transistors for flexible electronics. Applied Physics Reviews, 2016. 3(2): p. 021303.

[170] Chae, J.B., et al., Optimum thickness of hydrophobic layer for operating voltage reduction in EWOD systems. Sensors and Actuators A: Physical, 2014. 215: p. 8-16.

[171] Zhang, M., et al., Charge transport in hybrid halide perovskites. Physical Review B, 2017. 96(19): p. 195203.

[172] Bi, C., et al., Understanding the formation and evolution of interdiffusion grown organolead halide perovskite thin films by thermal annealing. Journal of Materials Chemistry A, 2014. 2(43): p. 18508-18514.

[173] Khan, S., L. Lorenzelli, and R.S. Dahiya, Technologies for printing sensors and electronics over large flexible substrates: a review. IEEE Sensors Journal, 2014. 15(6): p. 3164-3185.

[174] Cha, S., et al., Low-temperature, dry transfer-printing of a patterned graphene monolayer. Scientific reports, 2015. 5: p. 17877.

[175] Pudas, M., J. Hagberg, and S. Leppävuori, Printing parameters and ink components affecting ultra-fine-line gravure-offset printing for electronics applications. Journal of the European Ceramic Society, 2004. 24(10-11): p. 2943-2950.

[176] Ko, S.H., et al., Direct nanoimprinting of metal nanoparticles for nanoscale electronics fabrication. Nano letters, 2007. 7(7): p. 1869-1877.

[177] Singh, M., et al., Inkjet printing—process and its applications. Advanced materials, 2010. 22(6): p. 673-685.

[178] Shaheen, S.E., et al., Fabrication of bulk heterojunction plastic solar cells by screen printing. Applied Physics Letters, 2001. 79(18): p. 2996-2998.

[179] Yang, S., et al., Employing Pneumatic Nozzle Printing for Controlling the Crystal Growth of Small Molecule Organic Semiconductor for Field-Effect Transistors. Advanced Electronic Materials, 2018. 4(6): p. 1700534.

[180] Howard, I.A., et al., Coated and printed perovskites for photovoltaic applications. Advanced Materials, 2019. 31(26): p. 1806702.

[181] Mathies, F., E.J. List-Kratochvil, and E.L. Unger, Advances in Inkjet-Printed Metal Halide Perovskite Photovoltaic and Optoelectronic Devices. Energy Technology, 2019: p. 1900991.

[182] Gardner, K.L., et al., Nonhazardous solvent systems for processing perovskite photovoltaics. Advanced Energy Materials, 2016. 6(14): p. 1600386.

[183] Kim, J., et al., Solvent and intermediate phase as boosters for the perovskite transformation and solar cell performance. Scientific reports, 2016. 6: p. 25648.

[184] Control, C.f.D. and Prevention, Lead (Pb) toxicity: What are the US standards for lead levels? Atsdr. cdc. gov. 2016. 2018.

Appendix A: Supplementary Information for Chapter 5

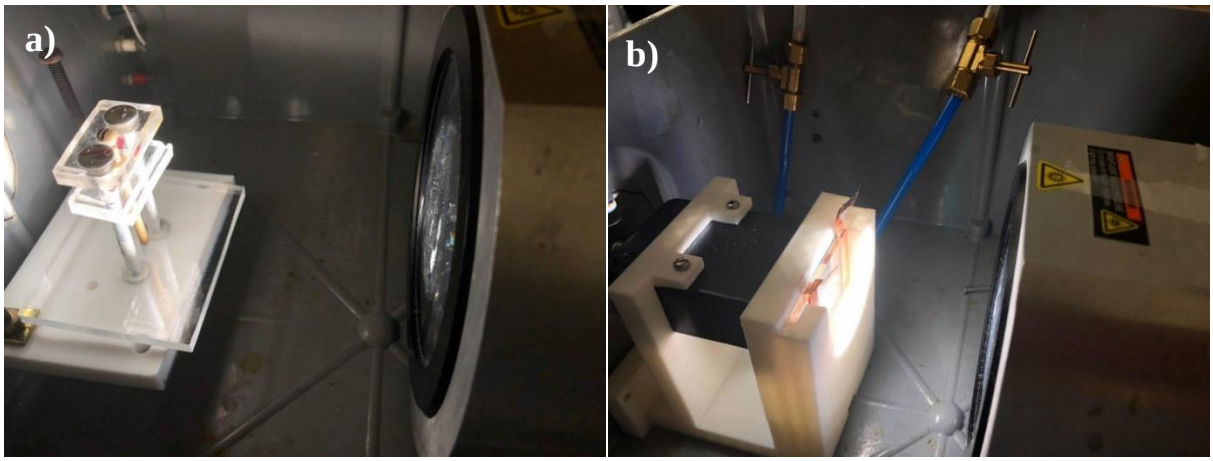

Figure S 1 The setups used for the I-V measurements under light illumination. (a) for different bending curvatures which were performed by turning the screw and changing the distance between the two plates, and (b) for applying the normal forces (two valves were using to push or release the piston connected to a pressure gauge).

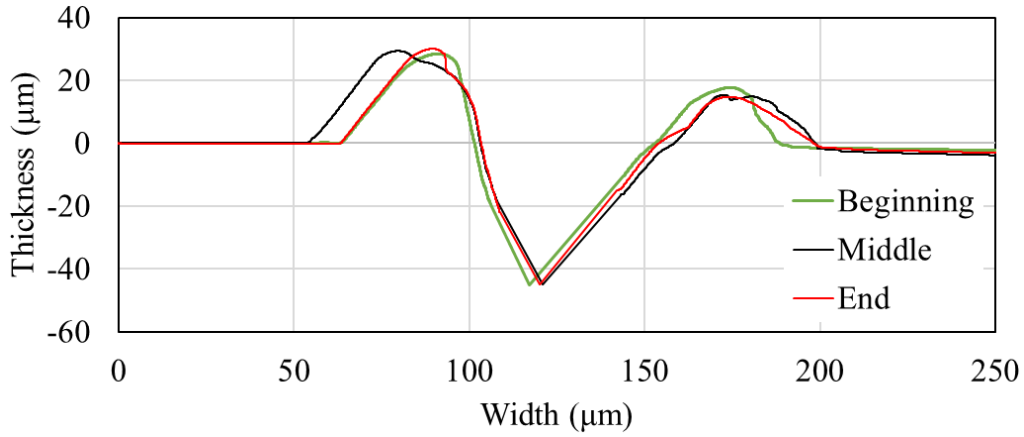

Figure S 2 Thickness profile of the cut layer (microchannel) across the channel and at the different spots along the channel.

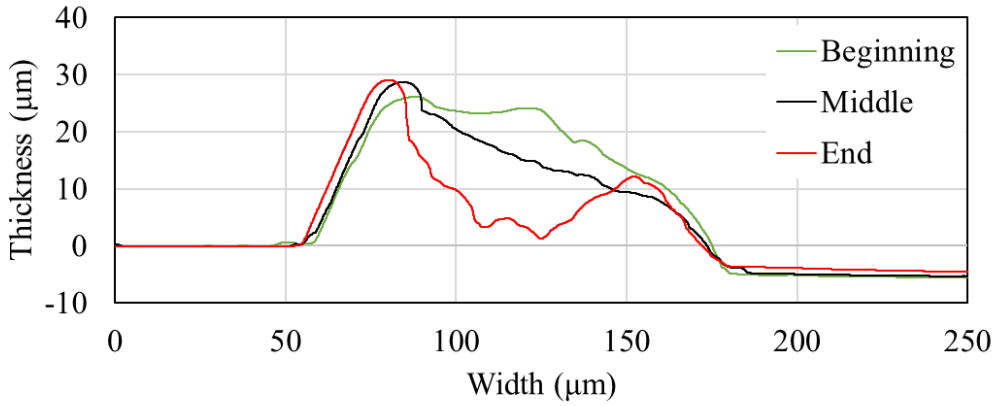

Figure S 3 Thickness profile of the perovskite layer across the channel and at the different spots along the channel.

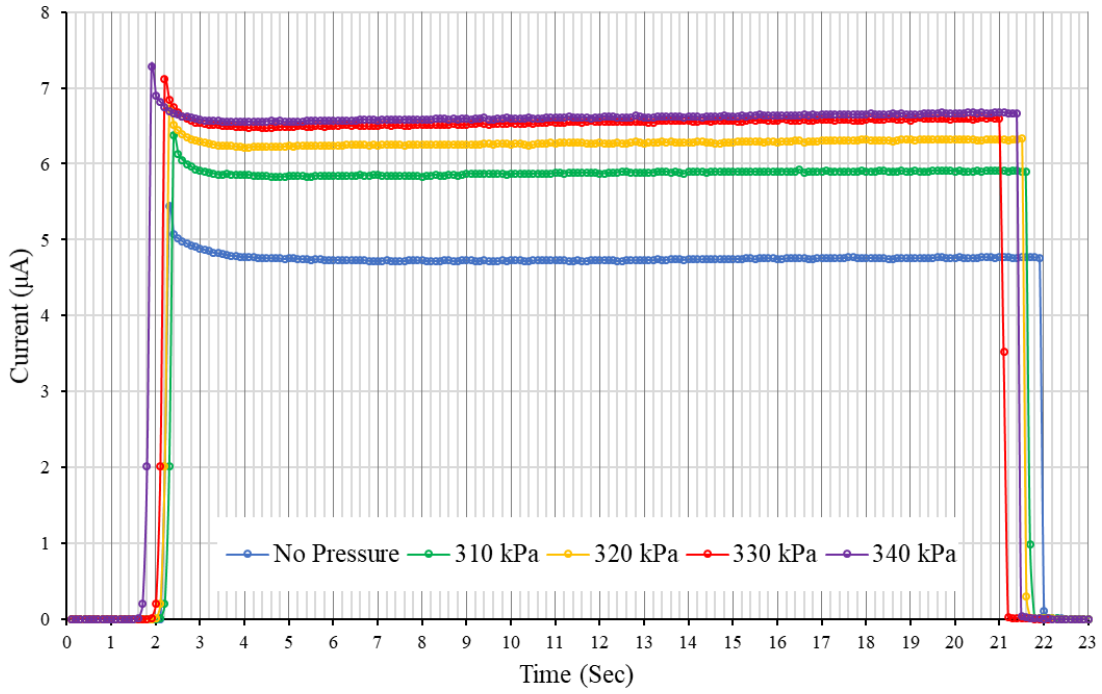

Figure S 4 Single photocurrent response cycle of the device at 2.0 V bias with light irradiation on and off, at different normal pressures (illumination for ~20 s, manually started at ~2nd second, 80 mW/cm^2).

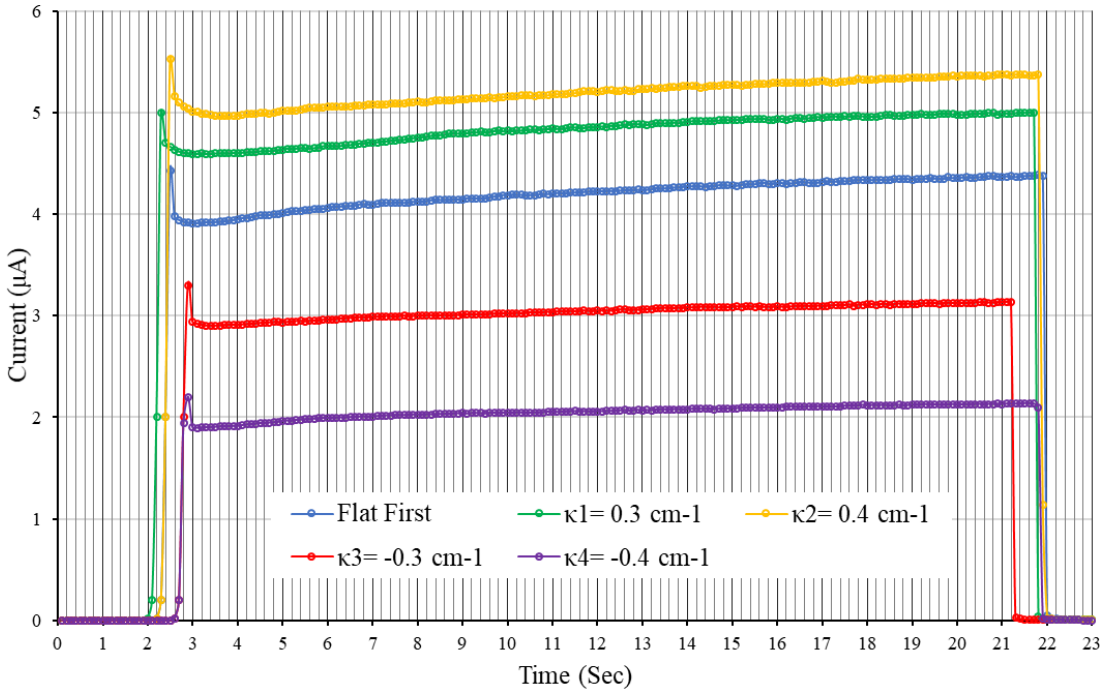

Figure S 5 Single photocurrent response cycle of the device at 2.0 V bias with light irradiation on and off, at different bending curvatures (illumination for ~20 s, manually started at ~2nd second, 80 mW/cm^2).

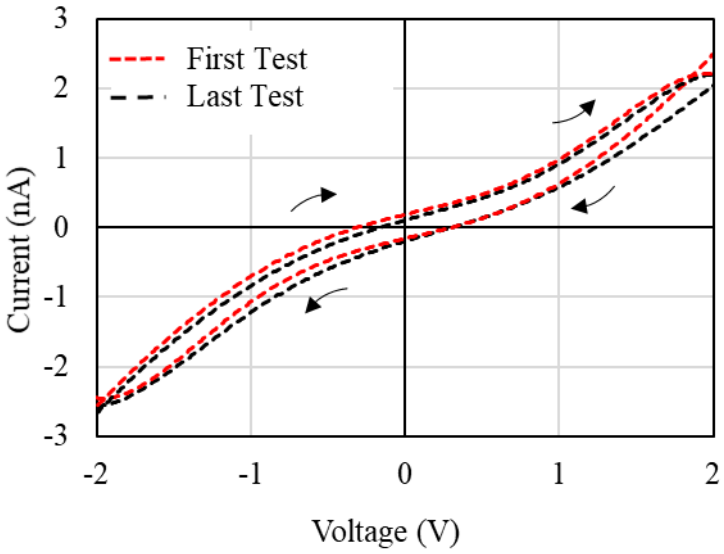

Figure S 6 I-V characteristics of the device in dark before applying compressive/tensile stress on the device as the first test and after all measurements (compressive normal force and concave/convex bending) as the last test, 50 mV/sec scan rate.

Appendix B: Copyright Permissions

Below is permission for the use of Figure 1.1.

Order license ID	1038766-1
Order detail status	Completed
ISSN	1473-0189
Type of use	Republish in a thesis/dissertation
Publisher	ROYAL SOCIETY OF CHEMISTRY
Portion	Image/photo/illustration

0.00 USD
Republication Permission

LICENSED CONTENT

Publication Title	Lab on a chip	**Country**	United Kingdom of Great Britain and Northern Ireland
Author/Editor	Royal Society of Chemistry (Great Britain)	**Rightsholder**	Royal Society of Chemistry
Date	01/01/2001	**Publication Type**	e-Journal
Language	English	**URL**	http://www.rsc.org/loc

REQUEST DETAILS

Portion Type	Image/photo/illustration	**Distribution**	Worldwide
Number of images / photos / illustrations	1	**Translation**	Original language of publication
Format (select all that apply)	Print,Electronic	**Copies for the disabled?**	No
Who will republish the content?	Academic institution	**Minor editing privileges?**	No
Duration of Use	Life of current edition	**Incidental promotional use?**	No
Lifetime Unit Quantity	Up to 499	**Currency**	USD
Rights Requested	Main product		

NEW WORK DETAILS

Title	Theory, Fabrication, and Characterization of Perovskite Phototransistor	**Institution name**	University of South Florida
Instructor name	Fatemeh Khorramshahi	**Expected presentation date**	2020-06-04

ADDITIONAL DETAILS

The requesting person / organization to appear on the license	Fatemeh Khorramshahi

REUSE CONTENT DETAILS

Title, description or numeric reference of the portion(s)	Theory, Fabrication, and Characterization of Perovskite Phototransistor	**Title of the article/chapter the portion is from**	INTRODUCTION
Editor of portion(s)	N/A	**Author of portion(s)**	Royal Society of Chemistry (Great Britain)
Volume of serial or monograph	N/A	**Publication date of portion**	2001-01-01
Page or page range of portion	2		

Total Items: 1

Subtotal: 0.00 USD
Order Total: 0.00 USD

Below is permission for the use of Figure 2.2.

AIP PUBLISHING LICENSE
TERMS AND CONDITIONS

Jun 01, 2020

This Agreement between Fatemeh Khorramshahi ("You") and AIP Publishing ("AIP Publishing") consists of your license details and the terms and conditions provided by AIP Publishing and Copyright Clearance Center.

License Number	4840300418947
License date	Jun 01, 2020
Licensed Content Publisher	AIP Publishing
Licensed Content Publication	Applied Physics Letters
Licensed Content Title	Qualifying composition dependent p and n self-doping in CH3NH3PbI3
Licensed Content Author	Qi Wang, Yuchuan Shao, Haipeng Xie, et al
Licensed Content Date	Oct 20, 2014
Licensed Content Volume	105
Licensed Content Issue	16
Type of Use	Thesis/Dissertation
Requestor type	Student
Format	Print and electronic

Portion	Photograph/Image
Number of Photographs/Images	1
Title	Theory, Fabrication, and Characterization of Perovskite Phototransistor
Institution name	University of South Florida
Expected presentation date	Jun 2020
Portions	Figure 3
Requestor Location	TAMPA, FL 33613 United States Attn: Fatemeh Khorramshahi
Total	0.00 USD

Below is permission for the use of material in Chapter 3.

RE: Reprint and Re-Use Permission Request

Shannon Engelbrecht <shannone@spie.org>

Thu 5/28/2020 7:30 PM

To: Khorramshahi, Fatemeh <khorramshahi@usf.edu>

Dear Fatemeh Khorramshahi,

Thank you for seeking permission from SPIE to reprint material from our publications. SPIE shares the copyright with you, so as author you retain the right to reproduce your papers in part or in whole.

Publisher's permission is hereby granted under the following conditions:
(1) the material to be used has appeared in our publication without credit or acknowledgment to another source; and
(2) you credit the original SPIE publication. Include the authors' names, title of paper, volume title, SPIE volume number, and year of publication in your credit statement.

Please let me know if I may be of any further assistance.

Sincerely,

Shannon Engelbrecht
Conference Programs & Proceedings Assistant
shannone@spie.org
SPIE is the international society for optics and photonics
http://SPIE.org
SPIE.

From: Khorramshahi, Fatemeh <khorramshahi@usf.edu>
Sent: Wednesday, May 27, 2020 6:52 PM
To: reprint_permission <reprint_permission@spie.org>
Subject: Reprint and Re-Use Permission Request

Dear Madam/Sir,

I am writing to you to request the Re-use of two papers in the SPIE proceeding that I am the first author. Here is the information:

1. Novel fabrication of flexible perovskite photosensor using capillary motion, Khorramshahi, Fatemeh, and Arash Takshi. *Organic and Hybrid Sensors and Bioelectronics XI*. Vol. 10738. International Society for Optics and Photonics, 2018.
2. Laser assisted rapid fabrication of perovskite photodetector. Khorramshahi, Fatemeh, Belqasem Aljafari, Ioannis Kymissis, and Arash Takshi. *Organic and Hybrid Sensors and Bioelectronics XII*. Vol. 11096. International Society for Optics and Photonics, 2019.

I would like to reuse them in my Ph.D. dissertation which will be published by the University of South Florida.

Thank you for your time.
I am looking forward to hearing from you.

Best regards,
Fatemeh Khorramshahi

Below is permission for the use of material in Chapter 4.

CAMBRIDGE UNIVERSITY PRESS LICENSE
TERMS AND CONDITIONS

May 27, 2020

This Agreement between Fatemeh Khorramshahi ("You") and Cambridge University Press ("Cambridge University Press") consists of your license details and the terms and conditions provided by Cambridge University Press and Copyright Clearance Center.

License Number	4837150414745
License date	May 27, 2020
Licensed Content Publisher	Cambridge University Press
Licensed Content Publication	MRS Advances
Licensed Content Title	Study of the stability of lead halide perovskite under two different fluoropolymer top coatings
Licensed Content Author	Fatemeh Khorramshahi, Arash Takshi
Licensed Content Date	Feb 10, 2020
Licensed Content Volume	5
Licensed Content Issue	8-9
Start page	377
End page	383
Type of Use	Dissertation/Thesis
Requestor type	Author

Portion	Full article
Author of this Cambridge University Press article	Yes
Author / editor of the new work	Yes
Title	Theory, Fabrication, and Characterization of Perovskite Phototransistor
Institution name	University of South Florida
Expected presentation date	Jun 2020
Territory for reuse	World
Requestor Location	TAMPA, FL 33613 United States Attn: Fatemeh Khorramshahi
Publisher Tax ID	GB823847609
Total	0.00 USD

Below is permission for the use of material in Chapter 5 and Appendix A.

JOHN WILEY AND SONS LICENSE
TERMS AND CONDITIONS

May 27, 2020

This Agreement between Fatemeh Khorramshahi ("You") and John Wiley and Sons ("John Wiley and Sons") consists of your license details and the terms and conditions provided by John Wiley and Sons and Copyright Clearance Center.

License Number	4837371431355
License date	May 27, 2020
Licensed Content Publisher	John Wiley and Sons
Licensed Content Publication	Advanced Electronic Materials
Licensed Content Title	Apparent Piezo-Photocurrent Modulation in Methylammonium Lead Iodide Perovskite Photodetectors
Licensed Content Author	Fatemeh Khorramshahi, Adam G. Woughter, Manoj K. Ram, et al
Licensed Content Date	Aug 22, 2019
Licensed Content Volume	5
Licensed Content Issue	12
Licensed Content Pages	9

Type of use	Dissertation/Thesis
Requestor type	Author of this Wiley article
Format	Print and electronic
Portion	Full article
Will you be translating?	No
Title	Theory, Fabrication, and Characterization of Perovskite Phototransistor
Institution name	University of South Florida
Expected presentation date	Jun 2020
Requestor Location	TAMPA, FL 33613 United States Attn: Fatemeh Khorramshahi
Publisher Tax ID	EU826007151
Total	0.00 USD

About the Author

Fatemeh Khorramshahi received her B.Sc. in Electrical Engineering in 2010 and her M.Sc. in Photonics Engineering in 2013. During her master's studies, she served as a Teaching Assistant and later as an instructor at Amirkabir University of Technology (Tehran Polytechnic) in the Department of Electrical Engineering and the Department of Computer Engineering and Information Technology.

She earned her Ph.D. in Electrical Engineering at the University of South Florida (USF) in 2020 where she served as a Research Assistant in Bio-Organic Electronics lab. Her research was mainly focused on advanced techniques for fabrication of perovskite photovoltaic devices, ion-migration and piezoelectricity in lead halide perovskites, and ion-sensitive FETs for studying the self-assembly of photosynthetic proteins.

Fatemeh also served as a Teaching Assistant in USF for several courses at the Department of Electrical Engineering and as a researcher at Columbia University. In her Ph.D. studies, she received Matching Grant Research Award from Florida High Tech Corridor Council and scholarship from the Persian American Society of Tampa Bay.